Photoactive Iron N-Heterocyclic Carbene Complexes

From Design to Photoredox Catalysis

Schwarz, Jesper

2024

Document Version:
Publisher's PDF, also known as Version of record




Photoactive Iron *N*-Heterocyclic Carbene Complexes

From Design to Photoredox Catalysis

JESPER SCHWARZ
CENTRE FOR ANALYSIS AND SYNTHESIS | LUND UNIVERSITY






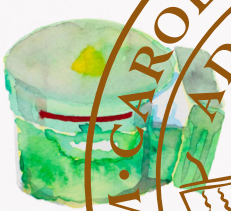


Photoactive Iron *N*-Heterocyclic Carbene Complexes

Photoactive Iron *N*-Heterocyclic Carbene Complexes

From Design to Photoredox Catalysis

Jesper Schwarz

LUND
UNIVERSITY

DOCTORAL DISSERTATION

Doctoral dissertation for the degree of Doctor of Philosophy (PhD) at the Faculty of Science at Lund University to be publicly defended on Friday, November 22 at 09.00 in lecture hall KC:A, Department of Chemistry, Naturvetarvägen 22, Lund.

Faculty opponent
Prof. David E. Herbert, University of Manitoba

Organization: LUND UNIVERSITY

Document name: Doctoral dissertation **Date of issue:** 2024-11-22

Author: Jesper Schwarz

Title and subtitle: Photoactive Iron *N*-Heterocyclic Carbene Complexes: From Design to Photoredox Catalysis

Abstract:

Recent years have seen a surge to develop first-row transition metal complexes with photophysics and photochemistry similar to those of noble metals, such as ruthenium and iridium. The reason for this is obvious, looking at their relative abundance. Iron stands out as the most abundant transition metal on earth, and is positioned right above ruthenium in the periodic table.

The aim of this thesis has been to design and synthesise new photoactive iron complexes, and to apply these in artificial photosynthesis and photoredox catalysis. The strategy for both the new complexes and existing complexes has been to use *N*-heterocyclic carbenes (NHC) as strongly σ-donating ligands, to increase the ligand field splitting. This raises the metal-centred (MC) excited states in energy compared to the charge transfer excited states, which introduces a barrier for the deexcitation through the MC states.

In the first manuscript, a π-extended NHC ligand was used to both raise the MC state energy and lower the charge transfer state energy. The aim was to increase the barrier for deexcitation through the MC states even more. However, the ligand-to-metal charge transfer (LMCT) state of the Fe^{III} complex was found to have a lifetime of only 14 ps, possibly because of fast direct deactivation to the ground state. The same complex was also isolated in its Fe^{II} state, which was found to have an excited state lifetime of 120 ns. The nature and potential applications of this excited state are currently investigated.

In the second chapter, the investigation of two different oxidation states of a cyclometallated iron complex, previously published in the Fe^{III} state, revealed insights into the photophysics. While the Fe^{III} complex had been claimed to feature dual luminescence, it was discovered that the blue emission originated from a small but highly emissive impurity.

The two final papers included in this thesis showcase the use of iron *N*-heterocyclic carbene complexes as photosensitisers in artificial photosynthesis and photoredox catalysis. For the first time, a high yielding hydrogen evolution reaction driven by an iron photosensitiser was demonstrated. In the photoredox catalysis reaction, an unusual biphotonic consecutive photoinduced electron transfer mechanism was found to be operating.

These findings underscore the potential of iron *N*-heterocyclic carbene complexes as viable and cost-effective alternatives to noble metals in photochemical applications. The research advances our understanding of iron complex photophysics and lays the groundwork for their future use in artificial photosynthesis and photoredox catalysis.

Key words: Iron, *N*-heterocyclic carbenes, photocatalysis, photoredox catalysis, artificial photosynthesis, photosensitisers, Earth-abundant

Language: English

ISBN (print): 978-91-8096-068-7

ISBN (electronic): 978-91-8096-069-4 **Number of pages**: 215

Photoactive Iron *N*-Heterocyclic Carbene Complexes

From Design to Photoredox Catalysis

Jesper Schwarz

LUND
UNIVERSITY

Front cover: Illustration by Jesper Schwarz.

Back cover: Arches National Park, Utah, USA. The green and red colours of the rock result from iron in two different oxidation states, much like the iron complexes in this thesis, which display different colours based on their oxidation state. Photo by Jesper Schwarz.

Faculty of Science

Department of Chemistry

Centre for Analysis and Synthesis

ISBN (print): 978-91-8096-068-7

ISBN (electronic): 978-91-8096-069-4

Printed in Sweden by Media-Tryck, Lund University

Lund 2024

To Curiosity

Table of Contents

Populärvetenskaplig sammanfattning

Inom kemi i allmänhet, och organisk kemi i synnerhet, har komplex av ädelmetaller såsom rutenium och iridium blivit väldigt populära och använda under de senaste 16 åren. Dessa metallkomplex är molekyler som består av en metalljon omgiven av organiska ligander. Ligander är organiska molekyler som binder till metallen, och som vi kan modifiera för att ge metallkomplexen olika egenskaper. Intresset för dessa metallkomplex har exploderat de senaste åren eftersom de kan absorbera ljusenergi och omvandla ljusenergin till kemisk energi. Detta används redan idag för att tillverka organiska föreningar på nya sätt, och kan i framtiden användas i solceller eller för att producera vätgas från vatten.

När dessa metallkomplex absorberar ljus, så exciteras en elektron till en högre energinivå. Den högre energin hos elektronen är den som sedan kan användas för att driva kemiska reaktioner, eller för att driva en solcell. För att driva kemiska reaktioner, måste elektronen vara kvar i det exciterade tillståndet tillräckligt länge för att möta en annan molekyl att reagera med. Om livslängden på det exciterade tillståndet är för kort trillar elektronen ner till grundtillståndet igen, innan energin hinner överföras. Fördelen med komplex av ädelmetallerna rutenium och iridium är att de har livstider på det exciterade tillståndet på flera hundra nanosekunder, upp till mikrosekunder, vilket gör att det finns gott om tid att reagera med andra molekyler. Nackdelen med rutenium och iridium är att de är extremt sällsynta och dyra (180 000 respektive 1,7 miljoner kr/kg), vilket gör att det inte kommer att gå att skala upp användningen av deras metallkomplex till stor skala. Mängden som behövs för storskalig produktion av exempelvis vätgas finns inte på jorden.

I min forskning har jag i stället undersökt om vi kan använda en annan metall, järn, och ge dess komplex samma egenskaper som komplexen av rutenium och iridium. Målet med forskningen har varit att förlänga det exciterade tillståndet hos järnkomplex, samt att visa på praktiska tillämpningar av dessa järnkomplex. Järn befinner precis ovanför rutenium i det periodiska systemet, och liknar därför i vissa aspekter rutenium kemiskt. Järn är också jordskorpans näst vanligaste metall, och därför betydligt billigare (<10 kr / kg). Dock är det inte helt lätt att modifiera järn så att det mer liknar rutenium, vilket till stor del beror på den mindre storleken av järns elektronmoln jämfört med elektronmolnen hos tyngre metaller såsom rutenium och iridium.

I den första delen av avhandlingen beskriver jag hur jag har tillverkat järnkomplex med målet att ge dessa en så lång livstid på det exciterade tillståndet som möjligt. I artikel ett var designstrategin att göra liganden, dvs den organiska molekylen runt järnet, mer mottaglig för elektroner. Detta skulle höja barriären för att den exciterade elektronen ska trilla ner till grundtillståndet, vilket skulle göra det exciterade tillståndet mer långlivat. Tyvärr visade det sig att elektronen kunde ta en annan väg tillbaka till

grundtillståndet, vilket gjorde att det exciterade tillståndet fick en livstid på endast 14 pikosekunder, för kort för att kunna driva kemiska reaktioner. En reducerad form av järnkomplexet visade sig dock ha ett betydligt längre exciterat tillstånd med en livstid på 120 nanosekunder, och vi undersöker nu hur vi kan använda detta.

I artikel två undersökte vi ett järnkomplex som hade rapporterats vara fluorescerande i två olika färger (rött och blått), något som är väldigt ovanligt. Genom att tillverka komplexet i väldigt ren form kunde vi visa att den blå fluorescensen kom från en orenhet, och att den sanna livstiden på det exciterade tillståndet var 240 pikosekunder, men att den röda fluorescensen stämde.

Den tredje artikeln beskriver utvecklingen av en metod för att mäta sammansättningen av olika gaser som bildas i en reaktion, vilket vi behövde för att kunna mäta mängden bildad vätgas i nästa projekt. Med en stark grön laser kan vi mäta mängden av olika gaser samtidigt i realtid, vilket gör att vi kan följa reaktioner väldigt exakt. Tidigare metoder för att mäta gassammansättningar bygger på att en liten mängd gas tas ut med en gastät spruta, vilket punkterar reaktionskärlet och medför en risk för läckage och därmed felaktiga mätningar. Genom att istället använda en laser som går genom glaset till gasen förenklar vi och kortar vi ner tiden för gasmätandet, eftersom reaktionsbehållaren inte behöver punkteras.

Den fjärde artikeln beskriver hur vi för första gången använt ett järnkomplex för att absorbera ljus och katalytiskt producera vätgas i större mängder. I studien visar vi att järnkomplexet kan absorbera grönt ljus, exciteras, och överföra den absorberade energin i form av en elektron till två olika katalysatorer, som i sin tur reducerar protoner till vätgas. Även om järnkomplexet vi använde producerade vätgas långsammare än ruteniumkomplexet vi jämförde det med, var det betydligt mer stabilt, vilket gjorde att det till skillnad från ruteniumkomplexet överlevde ett dygns kraftig belysning.

Slutligen beskriver jag i den sista artikeln hur vi använt ett ljusabsorberande järnkomplex för att driva en kemisk reaktion. Genom att använda grönt ljus och ett järnkomplex bryter vi en kol–jod-bindning, som sedan adderar till en annan dubbelbinding och bildar två nya kol–kol- och kol–jod-bindningar. I studien fann vi också att en foton absorberas vid två olika tillfällen i reaktionen, en typ av reaktion som ännu är väldigt ovanlig.

Sammanfattningsvis har den här avhandlingen bidragit till ökad förståelse av vilka faktorer som påverkar det exciterade tillståndet hos järnkomplex, och visat att järnkomplex kan vara ett lovande och hållbart alternativ till ädelmetallkomplex för att driva kemiska reaktioner med ljus. Trots vissa begränsningar i reaktivitet och livslängd på det exciterade tillståndet, kan järnkomplexen användas för både vätgasproduktion och syntes av nya organiska molekyler. Resultaten öppnar för vidare utveckling av miljövänliga, ljusdrivna kemiska processer.

Popular science summary

In chemistry in general, and organic chemistry in particular, complexes of noble metals such as ruthenium and iridium have become very popular and widely used over the past 16 years. These metal complexes are molecules consisting of a metal ion surrounded by organic ligands. Ligands are organic molecules that bind to the metal, and we can modify them to give the metal complexes different properties. Interest in these metal complexes has exploded in recent years because they can absorb light energy and convert it into chemical energy. This is already being used today to produce organic compounds in new ways, and in the future, it may be used in solar cells or to produce hydrogen from water.

When these metal complexes absorb light, an electron is excited to a higher energy level. The higher energy of the electron can then be used to drive chemical reactions or power a solar cell. To drive chemical reactions, the electron must remain in the excited state long enough to encounter another molecule to react with. If the excited state's lifetime is too short, the electron will fall back to the ground state before the energy can be transferred. The advantage of noble metal complexes like ruthenium and iridium is that they have excited state lifetimes of several hundred nanoseconds, up to microseconds, giving plenty of time to react with other molecules. The downside of ruthenium and iridium is that they are extremely rare and expensive (16 000 and 150 000 €/kg, respectively), which makes scaling up the use of their metal complexes on a large scale impossible. The amount needed for large-scale hydrogen production, for example, does not exist on Earth.

In my research, I have instead investigated whether we can use another metal, iron, and give its complexes the same properties as those of ruthenium and iridium. The aim of the research has been to extend the excited state lifetime of iron complexes and to demonstrate practical applications of these complexes. Iron is located just above ruthenium in the periodic table, and therefore chemically resembles ruthenium in some aspects. Iron is also the second most common metal in the Earth's crust and therefore significantly cheaper (<1 €/kg). However, it is not easy to modify iron to resemble ruthenium more closely, largely due to the smaller size of iron's electron cloud compared to the electron clouds of heavier metals such as ruthenium and iridium.

In the first part of the thesis, I describe how I have synthesised iron complexes with the aim of giving them as long an excited state lifetime as possible. In the first paper, the design strategy was to make the ligand, i.e., the organic molecule around the iron, more electron accepting. This would raise the barrier for the excited electron to fall back to the ground state, making the excited state more long-lived. Unfortunately, it turned out that the electron could take another path back to the ground state, resulting in an excited state lifetime of only 14 picoseconds, too short to drive chemical reactions.

However, a reduced form of the iron complex exhibited a significantly longer excited state lifetime of 120 nanoseconds, and we are now investigating how we can exploit this.

In the second paper, we examined an iron complex that had been reported to fluoresce in two different colours (red and blue), something that is very rare. By synthesising the complex in a very pure form, we were able to show that the blue fluorescence came from an impurity, and that the true excited state lifetime was 240 picoseconds, but that the red fluorescence was present.

The third paper describes the development of a method for measuring the composition of different gases produced in a reaction, which we needed to measure the amount of hydrogen produced in the next project. Using a powerful green laser, we can measure the amounts of different gases simultaneously in real time, allowing us to monitor reactions very accurately. Previous methods for measuring gas compositions relied on taking a small gas sample with a gas-tight syringe, which punctured the reaction vessel and risked leakage, leading to inaccurate measurements. By instead using a laser that passes through the glass to the gas, we simplify and shorten the time required for gas measurements, as the reaction vessel does not need to be punctured.

The fourth paper describes how we have, for the first time, used an iron complex to absorb light and catalytically produce substantial amounts of hydrogen. In the study, we show that the iron complex can absorb green light, become excited, and transfer the absorbed energy in the form of an electron to two different catalysts, which in turn reduce protons to hydrogen gas. Although the iron complex we used produced hydrogen more slowly than the ruthenium complex we compared it to, it was significantly more stable, which meant that, unlike the ruthenium complex, it survived a full day of intense illumination.

Finally, in the last paper, I describe how we used a light-absorbing iron complex to drive a chemical reaction. By using green light and an iron complex, we break a carbon–iodine bond, which then adds to another double bond, forming two new carbon–carbon and carbon–iodine bonds. In the study, we also found that a photon is absorbed at two different points in the reaction, a type of reaction that is still very rare.

In summary, this thesis has contributed to a greater understanding of the factors that affect the excited state in iron complexes and has shown that iron complexes can be a promising and sustainable alternative to noble metal complexes for driving light-driven chemical reactions. Despite some limitations in reactivity and lifetime of the excited state, the iron complexes can be used for both hydrogen production and the synthesis of new organic molecules. The results open the door for further development of environmentally friendly, light-driven chemical processes.

List of papers

This thesis is based on the following papers, referred to by their Roman numerals.

‡These authors contributed equally.

I Extending the π-system of a Luminescent Iron *N*-Heterocyclic Carbene Complex to Increase the Barrier for Internal Conversion

J. Schwarz, M. Zhang, M. Al Rammal, A. Mishra, T. Ericsson, L. Häggström, F. Lindgren, P. Huang, S. Kaufhold, J. Bendix, E. Jakubikova, R. Lomoth and K. Wärnmark

Manuscript

II Ferrous and Ferric Complexes with Cyclometalating *N*-Heterocyclic Carbene Ligands: A Case of Dual Emission Revisited

C. E. Johnson, J. Schwarz, M. Deegbey, O. Prakash, K. Sharma, P. Huang, T. Ericsson, L. Häggström, J. Bendix, A. K. Gupta, E. Jakubikova, K. Wärnmark and R. Lomoth

Chem. Sci. **2023**, *14*, 10129–10139

III Simultaneous Non-Invasive Gas Analysis in Artificial Photosynthesis Reactions Using Rotational Raman Spectroscopy.

J. Schwarz‡, A. Ilic‡, S. Kaufhold, J. Ahokas, P. Myllyperkiö, M. Pettersson and K. Wärnmark

Sustain. Energy Fuels **2022**, *6*, 4388–4392

IV High Turnover Photocatalytic Hydrogen Formation with an Fe(III) *N*-Heterocyclic Carbene Photosensitiser

J. Schwarz‡, A. Ilic‡, C. Johnson‡, R. Lomoth and K. Wärnmark

Chem. Commun. **2022**, *58*, 5351–5354

V Photoredox Catalysis via Consecutive ^{2}LMCT- and ^{3}MLCT-Excitation of an Fe(III/II)–*N*-Heterocyclic Carbene Complex

A. Ilic‡, J. Schwarz‡, C. Johnson‡, L. H. M. de Groot, S. Kaufhold, R. Lomoth and K. Wärnmark

Chem. Sci. **2022**, *13*, 9165–9175

The following related publications are not included in this thesis.

VI Photophysical Integrity of the Iron(III) Scorpionate Framework in Iron(III)–NHC Complexes with Long-Lived ^{2}LMCT Excited States.

O. Prakash, L. Lindh, N. Kaul, N. W. Rosemann, I. B. Losada, C. Johnson, P. Chábera, A. Ilic, J. Schwarz, A. K. Gupta, J. Uhlig, T. Ericsson, L. Häggström, P. Huang, J. Bendix, D. Strand, A. Yartsev, R. Lomoth, P. Persson and K. Wärnmark

Inorg. Chem. **2022**, *61*, 17515–17526

VII Competing Dynamics of Intramolecular Deactivation and Bimolecular Charge Transfer Processes in Luminescent Fe(III) *N*-Heterocyclic Carbene Complexes

N. W. Rosemann, L. Lindh, I. Bolaño Losada, S. Kaufhold, O. Prakash, A. Ilic, J. Schwarz, K. Wärnmark, P. Chábera, A. Yartsev and P. Persson

Chem. Sci. **2023**, *14*, 3569–3579

VIII High-Efficiency Photoinduced Charge Separation in Fe(III)Carbene Thin Films

M. Zhang, C. E. Johnson, A. Ilic, J. Schwarz, M. B. Johansson and R. Lomoth

J. Am. Chem. Soc. **2023**, *145*, 19171–19176

IX Iron Photoredox Catalysis – Past, present, and future

L. H. M. de Groot‡, A. Ilic‡, J. Schwarz‡ and K. Wärnmark,

J. Am. Chem. Soc. **2023**, *145*, 9369–9388

Author's contribution to the papers

Paper I

I conceived the project, planned it, and performed all the synthesis. I characterised the compounds by ^{1}H- and ^{13}C-NMR, UV-vis absorption spectroscopy and magnetic susceptibility measurements. I coordinated the writing, wrote major parts of the manuscript, and reviewed it with input from the other authors.

Paper II

I synthesised the complexes, characterised them by ^{1}H- and ^{13}C-NMR, UV-vis absorption spectroscopy and magnetic susceptibility measurements. I did the photodegradation studies, analysed the data and contributed to the discussion and development of the hypothesis regarding the origin of the emissive impurity. I wrote parts of the manuscript and took part in reviewing and editing.

Paper III

I performed large parts of the experimental work, including calibration curves and hydrogen evolution reactions, and interpreted the data. I coordinated the troubleshooting of the instrument and software. I coordinated the writing, wrote major parts of the manuscript, and reviewed it with input from the other authors.

Paper IV

I planned the project and performed large parts of the initial testing and optimisation reactions, and control reactions. I also conducted and analysed the results of mechanistic investigations, such as the time trace experiments. I coordinated the writing, wrote major parts of the manuscript, and reviewed it with input from the other authors.

Paper V

I performed large parts of the experimental work, including initial testing, optimisations and substrate scope for the oxidative quenching route and planned and carried out mechanistic investigations such as radical trapping experiments. I substantially contributed to conceiving the proposed mechanisms. I contributed to the writing and reviewing of the manuscript.

Abbreviations

*	Denotes the excited state of a species
A	Absorbance
A	Acceptor
ATRA	Atom Transfer Radical Addition
bpy	2,2'-Bipyridine
btz	3,3'-Dimethyl-1,1'-bis(p-tolyl)-4,4'-bis(1,2,3-triazol-5-ylidene)
CCD	Charge Coupled Device
conPET	Consecutive Photo-induced Electron Transfer
CT	Charge-transfer
D	Donor
DCM	Dichloromethane
dF(CF_3)ppy	2-(2,4-Difluorophenyl)-5-(trifluoromethyl)pyridine
DFT	Density Functional Theory
DMA	Dimethylaniline
DMF	Dimethylformamide
dmgH	Dimethylglyoximato
DMSO	Dimethylsulfoxide
dtbbpy	4,4'-Di-*tert*-butyl-2,2'-bipyridine
η_{ce}	Cage Escape Yield
η_q	Quenching Yield
ε	Molar absorption coefficient
E	Potential
$E_{1/2}$	Half-wave Potential
E_{0-0}	Energy gap between the lowest vibrational levels of the GS and ES
EPR	Electron Paramagnetic Resonance
ES	Excited State
Et_3N	Triethylamine
Φ	Quantum Yield
Fc	Ferrocene
GC	Gas Chromatography
GS	Ground State

GSB	Ground State Bleach
HE	Hantzsch Ester
HOMO	Highest Occupied Molecular Orbital
I_0	Intensity of incident light
I_{em}	Emission intensity
I_{tr}	Intensity of transmitted light
IC	Internal Conversion
IR	Infrared
ISC	Intersystem Crossing
k_{rET}	rate constant for in-cage reverse electron transfer
k_{bd}	rate constant for backdonation
k_{ce}	rate constant for cage escape
k_{nr}	rate constant for nonradiative decay
k_q	rate constant for quenching
k_r	rate constant for radiative decay
k_s	rate constant for single electron transfer to a substrate
K_D	Dynamic quenching constant
K_{SV}	Stern–Volmer constant
K_S	Static quenching constant/association constant
λ_{abs}	Absorption Wavelength
λ_{em}	Emission Wavelength
LMCT	Ligand-to-Metal Charge-transfer
LUMO	Lowest Unoccupied Molecular Orbital
MC	Metal-Centred
MeCN	Acetonitrile
MLCT	Metal-to-Ligand Charge-transfer
NHC	*N*-heterocyclic Carbene
ns	Nanosecond
OTf	Trifluoromethylsulfonate
PC	Photoredox Catalyst
phtmeimb	Tris(3-methyimidazolin-2-ylidene)(phenyl)borate
ppy	2-Phenylpyridine
PRC	Proton Reduction Catalyst
PS	Photosensitiser
ps	Picosecond

py	Pyridine
Q	Quencher
qpy	2,2':6',2'':6'',2'''-quaterpyridine
r	radius
SCE	Standard Calomel Electrode
SET	Single Electron Transfer
τ	Excited State Lifetime
TEA	Triethylamine
TEOA	Triethanolamine
THF	Tetrahydrofuran
TOF	Turnover Frequency
TON	Turnover Number
UV	Ultraviolet
vis	Visible

1 Introduction

Light

The overall goal of the work in this thesis is the conversion of light energy into chemical energy. The iron complexes in this thesis can be excited by light, that is an electron can be moved to a higher energy state, and the absorbed light energy can be transferred to another species in the form of an electron and converted to chemical energy.[1] Light is also used to study the iron complexes, either by steady-state absorption spectroscopy, or by transient absorption spectroscopy.

1.1 Coordination chemistry of iron complexes

Matter

In this thesis, iron complexes are designed, synthesised, and applied as photosensitisers and photoredox catalysts. Typical photosensitisers and photoredox catalysts are second- and third-row transition metal complexes, such as ruthenium polypyridyl and cyclometallated iridium phenylpyridyl complexes. The main reason for this is their beneficial photophysical properties, such as strong light absorption in the near-UV to visible region, long-lived energetic excited states and advantageous reduction and oxidation potentials.

Over the last decade, there has been a surge to synthesise first-row transition metal complexes with the same photophysical and photochemical properties as their second- and third-row analogues.[2,3] This is motivated by two reasons, the first one being the current movement towards green chemistry. Since first-row metals are significantly more abundant than second and third-row metals, being able to use them would present a more sustainable path, both in terms of economic and ecological sustainability.[4]

The second reason for the shift towards first-row metals is a more fundamental interest in challenging the limitations set by the atomic orbitals of the metals. First-row metals have relatively small atom radii, which is the same as their d-orbitals not extending as far into space as in heavier transition metals. The origin of this is the so-called primogenic effect, which states that whenever a shell with angular quantum number *l*

is occupied for the first time, radial nodes are absent except at the centre of the atom (r = 0).[5,6] For the transition metals, this absence of nodes means that the 3d orbitals do not extend further away from the core than the 3s and 3p orbitals (Fig. 1A). Contrarily, the 4d and 5d orbitals have radial nodes, which makes their maximum electron density extend beyond that of the corresponding s- and p-orbitals (Fig. 1B). According to ligand field theory, the contraction of the 3d orbitals compared to the 4d orbitals leads to intrinsic differences in how well the d-orbitals of the metal can interact with ligand orbitals, which in turn leads to differences in orbital splitting in the resulting complexes.[7]

Although the complexes discussed in this thesis deviate from the ideal octahedral symmetry (in fact they have D_{3d}, D_3 and C_{2v} symmetry), the orbital discussions will be based on a (pseudo)-octahedral complex symmetry. This is valid since all complexes in this thesis have six more or less equal metal-ligand bonds. In principle, one could also use iron complexes of other geometries, such as tetrahedral complexes, for photochemistry. However, the largest ligand field splitting is typically achieved in (pseudo)-octahedral complexes, as these complexes have the highest number of ligands interacting with the metal d-orbitals. The ligand field splitting of a tetrahedral complex (Δ_t) is only a fraction of the octahedral field splitting, $\Delta_t = 4/9\ \Delta_o$.

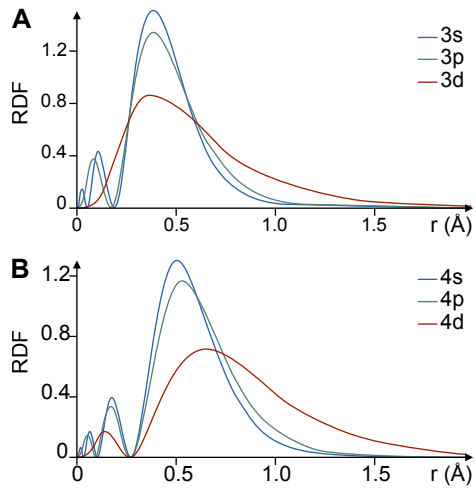

Figure 1. The primogenic effect. Radial distribution functions (RDFs) for the n = 3 shell of Fe^{II} (A) and the n = 4 shell of Ru^{II} (B). The plots illustrate the consequence of the primogenic effect, where the lack of a radial node for r ≠ 0 in the 3d orbital leads to it having a similar size compared to the 3p and 3d orbitals. In contrast, the 4d (and 5d) orbitals extend beyond their corresponding s- and p- orbitals. This leads to weaker metal-ligand interactions for the 3d orbital than are present in the case of 4d and 5d orbitals. Figure adapted from ref. 7. Reprinted with permission from AAAS.

1.2 Photophysics of iron complexes

Light meets matter

Because of the smaller 3d orbitals, the photophysics of iron complexes also deviate from those of $[Ru^{II}(bpy)_3]^{2+}$ (bpy = 2,2'-bipyridine), the archetype of a photoactive transition metal complex.[8,9] For the sake of argument, this discussion will start from a maybe naïve approach, comparing the two polypyridyl complexes $[Ru^{II}(bpy)_3]^{2+}$and $[Fe^{II}(bpy)_3]^{2+}$ (Fig. 2A). 2,2'-bipyridine is both a σ-donor and a π-acceptor, which leads to a splitting in orbital energy Δ_o between the t_{2g} and e_g levels of the resulting ruthenium complex (Fig. 2B). This splitting in orbital energy, typical of an octahedral complex, gives rise to photoactive excited states.

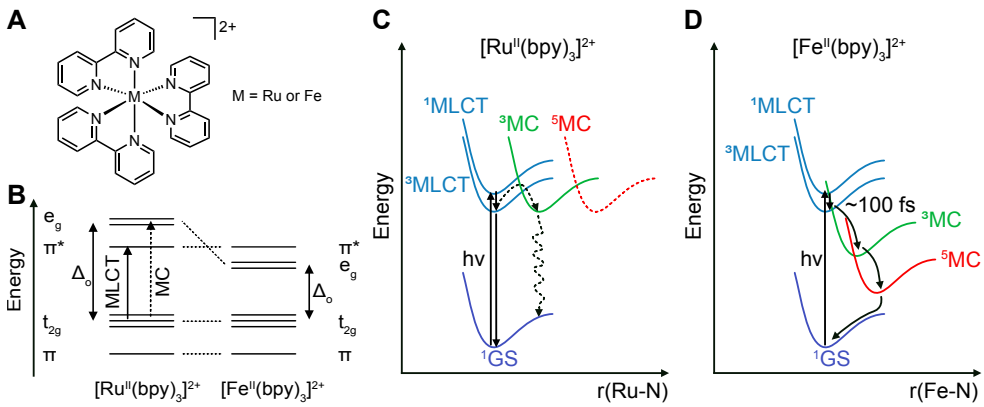

Figure 2. (A) Structure of $[M(bpy)_3]^{2+}$, M = Ru or Fe. (B) Schematic molecular orbital diagram for $[Ru^{II}(bpy)_3]^{2+}$ and $[Fe^{II}(bpy)_3]^{2+}$. (C) – (D) Schematic potential energy surfaces of $[Ru^{II}(bpy)_3]^{2+}$ and $[Fe^{II}(bpy)_3]^{2+}$. Dashed arrows denote non-favoured deactivation pathways. Adapted with permission from ref. 10. Copyright 2016 American Chemical Society.

In principle, one could imagine several possible excitations. However, the absorption of light follows certain rules. The first rule, spin selection, states that spin must be conserved in the excitation of an electron. The second rule, the Laporte rule, states that allowed transitions in complexes with inversion symmetry must involve a change in parity, either g → u or u → g. A consequence is that metal-centred (MC) d-d absorption bands are typically very weak in octahedral complexes ($\varepsilon < 1$ M^{-1} cm^{-1}). Charge transfer (CT) absorption bands, where an electron is excited from the metal to the ligand, or in the opposite direction, are therefore much stronger.

A photon with the right energy can therefore excite an electron from the t_{2g} orbitals of the metal to the ligand π^* orbitals. The resulting ^{1}MLCT (metal-to-ligand charge transfer) state of $[Ru^{II}(bpy)_3]^{2+}$ rapidly undergoes intersystem crossing (ISC, change of

spin) to the ^{3}MLCT state, which has a long lifetime (τ = 900 ns), during which it can interact with other molecules or relax back to the ground state through phosphorescence, releasing a photon. Deactivation through the MC states is slow, because of the activation barrier for internal conversion (IC, no spin change) from the ^{3}MLCT to the ^{3}MC (Fig. 2C).

Another important rule in photochemistry, that relates to how the excited states decay, is Kasha's rule. Derived from experimental observations, the original rule as stated by Kasha is: "*The emitting level of a given multiplicity is the lowest excited level of that multiplicity*"[11] The basis for this is that internal conversion is usually fast, much faster than luminescence. Generally, a molecule will therefore only emit light of one colour, matching the energy of the lowest excited state.[12] The rule can be extended to also encompass collisional quenching, meaning that the energy available for photocatalysis is generally also limited by the energy of the lowest excited state.[13,14] Notable exceptions exist, such as azulene, which emits from the second singlet excited state (S_2).[15]

Returning to the comparison between the photophysics of $[Fe^{II}(bpy)_3]^{2+}$ and $[Ru^{II}(bpy)_3]^{2+}$, several differences appear. Iron, having smaller d-orbitals, has a much poorer orbital overlap between the metal d-orbitals and the ligand orbitals. This now means that the e_g orbitals are lower in energy than the ligand π^*-orbitals (Fig. 2B), leading to the lowest excited states being MC states (Fig. 2D). Upon excitation of $[Fe^{II}(bpy)_3]^{2+}$ to the ^{1}MLCT state, it will undergo rapid ISC to the ^{3}MLCT state, from which deexcitation back to the ^{1}GS is spin forbidden (Fig. 2D). However, IC to the ^{3}MC state is barrierless, and from there it will relax nonradiatively back to the ground state. The lifetime of the ^{3}MLCT state is ca 120 femtoseconds (fs),[16] and this extremely short lifetime precludes any chemical reactivity of the ^{3}MLCT state.[17] Even if the MC states have a combined lifetime of about 1 ns, a significant amount of energy is lost compared to the ^{3}MLCT state.[16] In other words, a large part of the light energy of an absorbed photon is transformed into heat instead of being available for chemical reactivity.

Direct excitation to the MC states is also not a viable route for octahedral Fe-chromophores, as these d-d transitions are both Laporte- and spin-forbidden, which gives them a very weak absorption. There are recent examples where the MC states are used for photoredox catalysis, notably with Co complexes, however these still suffer from poor light absorption of their MC bands (ε <100 M^{-1} cm^{-1}).[18,19] An aim for the last decade has been to increase the lifetime of the ^{3}MLCT state of iron, so that it can be used in photoredox catalysis and artificial photosynthesis. From the considerations above, two possible strategies emerge to increase the activation barrier $\Delta G^{\ddagger}$ for the IC of the ^{3}MLCT state to the ^{3}MC state (Fig. 3):

1. Increasing Δ_o, to raise the ^{3}MC state to higher energies.
2. Lowering the energy of the ^{3}MLCT state compared to the ^{3}MC state.

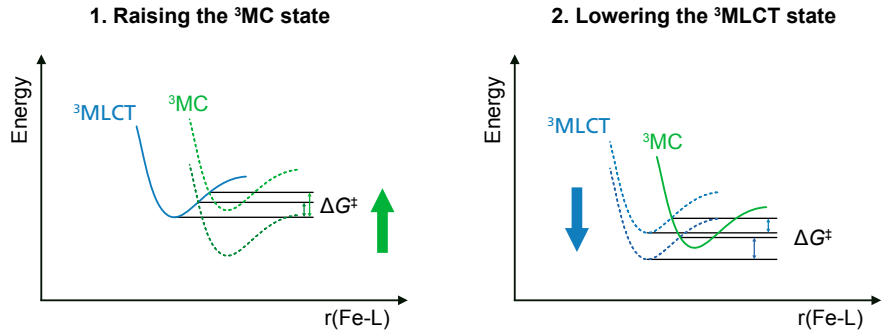

Figure 3. The two strategies for increasing the activation barrier $\Delta G^{\ddagger}$ for IC ^{3}MLCT → ^{3}MC.

The first strategy can be achieved by introducing strongly σ-donating and/or π-accepting ligands that interact with the e_g and t_{2g} orbitals respectively, and thereby increase the octahedral field splitting Δ_{oct}.[10,20] This increases the energy of the ^{3}MC state, and when the ^{3}MC state is moved up in energy relative to the ^{3}MLCT state, an energy barrier for IC between the two is introduced. The increase in energy of the MC states enables the excited electron to stay in the ^{3}MLCT state, instead of decaying back to the GS via the MC states. Further destabilisation of the ^{3}MC state prolongs the ^{3}MLCT lifetime. A π-accepting ligand will also lower the energy of the ^{3}MLCT state, impacting strategy two below.

The second strategy of lowering the ^{3}MLCT state relative to the ^{3}MC state has several effects on the photophysics. The ^{3}MLCT state can be lowered in energy by having a more electron accepting ligand, for instance by extending the π-system on the ligand, or by making the ligand more electron poor.[21–25] Lowering the energy of the ^{3}MLCT while maintaining the ^{3}MC state energy also introduces an energy barrier for passing from one to the other. Again, this increased barrier for deactivation through the MC state should extend the excited state lifetime.

However, another factor might give a contradicting effect. The energy gap law states that the rate for radiationless decay decreases exponentially with the energy gap between two states (eq. 1).[26–29]

$$k_{nr} \propto e^{-\alpha \Delta E} \qquad (1)$$

where k_{nr} is the rate of nonradiative decay, α is a constant that depends on the coupling strength and vibrational modes of the molecule and ΔE is the energy gap between the states. According to this, the rate of direct radiationless decay will increase when the energy gap between the CT states and the GS decreases. This factor becomes extra important for the spin-allowed deexcitation of ^{2}LMCT (ligand-to-metal charge transfer) states (see below).

Consequently, the design of iron complexes with long-lived excited states becomes more delicate, as these two effects have to be balanced. A further outcome of a lower energy ^{1}MLCT state is that the absorption is redshifted. This is beneficial both in artificial photosynthesis, where a good spectral overlap with the sunlight is needed, as well as in photoredox catalysis where destructive high energy light can be avoided. On the other hand, a lowered ^{3}MLCT state also decreases the energy available for chemical transformations from the excited state.

1.2.1 Introduction of *N*-heterocyclic carbene ligands changes the excited state landscape

The arguably most successful approach to increase the activation barrier for IC from the CT states to the MC states has been to introduce *N*-heterocyclic carbene (NHC) ligands.[10,30–33] These strongly σ-donating ligands will push the e_g orbitals to higher energies (Fig. 4), thus increasing the energy of the MC states. Pioneered in 2013, a tetra-NHC complex reached a ^{3}MLCT lifetime of 9 ps, an increase of almost two orders of magnitude compared to $[Fe(bpy)_3]^{2+}$.[20] Although the nature of the 9 ps excited state was later debated, it was a proof that this could be a viable strategy.[34,35] In 2018, an iron complex bearing six mesoionic carbene ligands, $[Fe^{II}(btz)_3]^{2+}$ (btz = 3,3'-dimethyl-1,1'-bis(p-tolyl)-4,4'-bis(1,2,3-triazol-5-ylidene)) reached a ^{3}MLCT lifetime of 528 ps, several orders of magnitude higher than what had previously been achieved (Fig. 5).[36] This strategy has successfully increased the ligand field splitting from Δ_o = 2.2–2.6 eV in $[Fe^{II}(bpy)_3]^{2+}$ to Δ_o = 3.2 eV in $[Fe^{II}(btz)_3]^{2+}$ and 3.8 eV in $[Fe^{III}(phtmeimb)_2]^+$ (phtmeimb = tris(3-methylimidazolin-2-ylidene)(phenyl)borate), Fig. 7).[19,37–39]

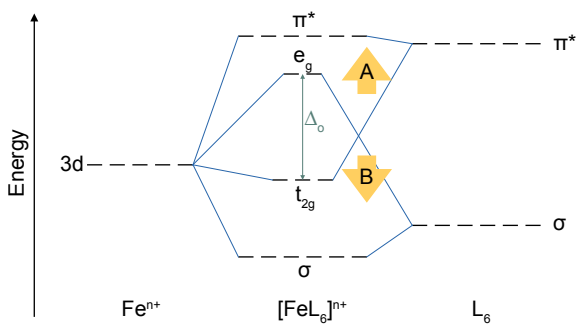

Figure 4. Approximate partial MO diagram for iron ligand bonding in an octahedral complex. (A) σ-donating ligands will raise the e_g orbital energy. (B) π-accepting ligands will lower the t_{2g} orbital energy.

Other strategies that have also led to long-lived ^{3}MLCT excited states are cyclometallation[40] and tetra-dentate macrocycles to give unusual nested excited state potentials[41] (Fig. 5). Calculations made by Dixon had predicted cyclometallation in combination with polypyridyl ligands as a route to photoactive Fe^{II} complexes with extended the ^{3}MLCT lifetimes[42–44], and such a design was realised by the group of Berkefeld in 2022 with the complex $[Fe^{II}(^{phen}N,N'\text{^}C)_2]$ ($(^{phen}N,N'\text{^}C)$ = 2-(4-(*tert*-butyl)phenyl)-1,10-phenanthroline).[40] The cyclometallated phenyl group is a strong σ-donor, while having better π-accepting properties than NHC ligands. In the case of $[Fe^{II}(HMTI)(CN)_2]$ (HMTI = 5,5,7,12,12,14-hexamethyl-1,4,8,11-tetraazacyclotetradeca-1,3,8,10-tetraene), it was argued by the authors that the ^{3}MLCT lifetime is extended by the rigidity of the tetradentate macrocycle, giving nested excited state potentials which slow down the nonradiative decay.

Another Fe^{II} complex with a long excited state lifetime (τ = 2.6 ns) was published by the group of Herbert in 2019.[45] Initially the long-lived excited state was thought to be of "π*-to-ligand charge transfer" character. This excited state was later reassigned using time-resolved X-ray emission spectroscopy to be a ^{5}MC state. [46]

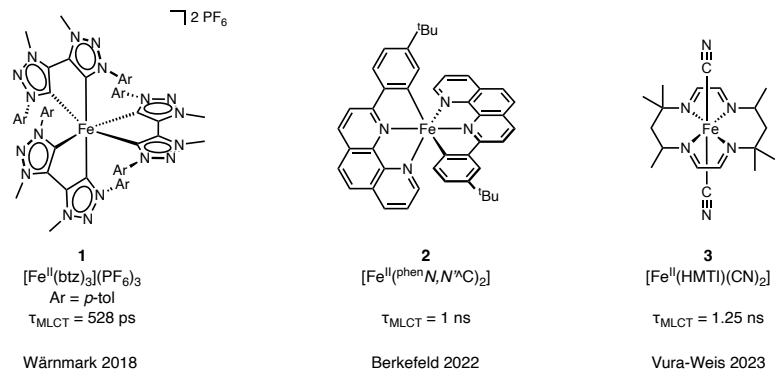

Figure 5. Fe^{II} complexes with long-lived ^{3}MLCT excited states.[36,40,41]

In the quest for long-lived ^{3}MLCT states, the number of strongly electron-donating NHC ligands was increased from four to six. A consequence of this was that the most stable oxidation state under ambient conditions changed from Fe^{II} to Fe^{III}. The Fe^{III} metal core was now easier to reduce than Fe^{II}, and the very electron rich ligands more easily oxidised compared to more electron poor ligands. This in turn meant that the lowest CT excited state was no longer a ^{3}MLCT, but rather a ^{2}LMCT state (Fig. 6). Formally, this corresponds to the excited state having an oxidised ligand and a reduced metal core. From the ^{2}LMCT state, the energy barrier for ISC to the ^{4}MC state is as high or even higher than the corresponding ^{3}MLCT → ^{3}MC barrier in Fe^{II} complexes, meaning that these ^{2}LMCT states can be even more long-lived.

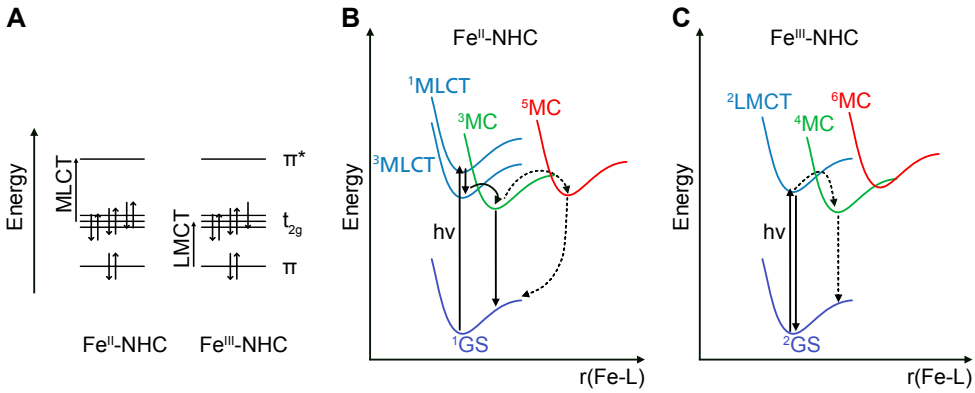

Figure 6. (A) Qualitative MO diagram for a d^6 Fe^{II} complex and a d^5 Fe^{III} complex. (B) and (C) Schematic potential energy surfaces for an Fe^{II}-NHC complex and an Fe^{III}-NHC complex respectively. Dashed arrows denote non-favourable deactivation pathways. Adapted with permission from ref. 10. Copyright 2016 American Chemical Society.

The longevity of the ^{2}LMCT state marked a shift in the design of photoactive iron complexes. From having solely focused on achieving long-lived ^{3}MLCT states, new Fe^{III} d^5 complexes were designed. With this, the first iron complex with visible photoluminescence at room temperature was discovered, $[Fe^{III}(phtmeimb)_2]PF_6$ (Fig. 7).[38] Furthermore, both oxidative and reductive quenching of a CT excited state in an iron complex could be demonstrated for the first time.[38,47] This complex has since then found use in hydrogen evolution reactions[48], organic light emitting diodes (OLEDs)[49], and photoredox catalysis[50,51]. Another complex that has shown an extended ^{2}LMCT lifetime of 240 ps is $[Fe^{III}(ImP)_2]^+$ (ImP = bis(2,6-bis(3-methylimidazol-2-ylidene-1-yl)phenylene)), which combines cyclometallation and NHC ligands.[52,53] This complex will be discussed extensively in chapter 4.

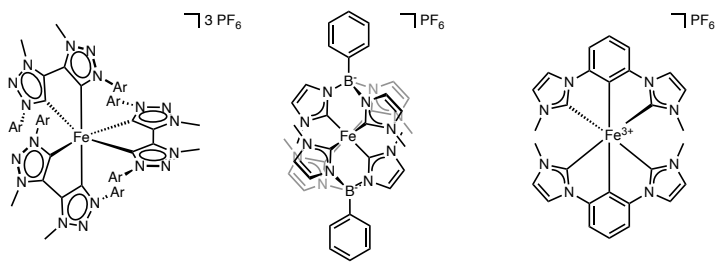

4
$[Fe^{III}(btz)_3](PF_6)_3$
Ar = *p*-tol
τ_{LMCT} = 100 ps
Wärnmark 2017

5
$[Fe^{III}(phtmeimb)_2]PF_6$
τ_{LMCT} = 2 ns
Wärnmark 2019

6
$[Fe^{III}(ImP)_2]PF_6$
τ_{LMCT} = 240 ps
Bauer, Wärnmark 2023

Figure 7. Fe^{III} complexes with long-lived ^{2}LMCT excited states.[38,52–54]

One of the fundamental laws in photochemistry is the Grotthus–Draper law: Only light that is absorbed can cause a chemical reaction.[55,56] Now that there are iron complexes with long-lived excited states, with proven electron transfer to/from the ^{2}LMCT state, a natural continuation is to apply them in photocatalysis reactions. The excited state properties of $[Fe(phtmeimb)_2]PF_6$ and $[Fe^{III/II}(btz)_3](PF_6)_{3/2}$ can be summarised in two Latimer diagrams (Fig. 8 and 9). These electrochemical data are important as a background for the photoredox catalysis, as they allow us to determine if electron transfer to/from a substrate is thermodynamically possible. We can for instance see that $*[Fe(phtmeimb)_2]^+$ is strongly reducing and fairly oxidising, even more so than the excited state of $[Ru(bpy)_3]^+$ ($E^o(Ru^{III/*}Ru^{II})$ = –0.81 V vs SCE, $E^o(*Ru^{II/}Ru^{II}(bpy)_2(bpy)^{\bullet-})$ = 0.77 V vs SCE)[57,58].

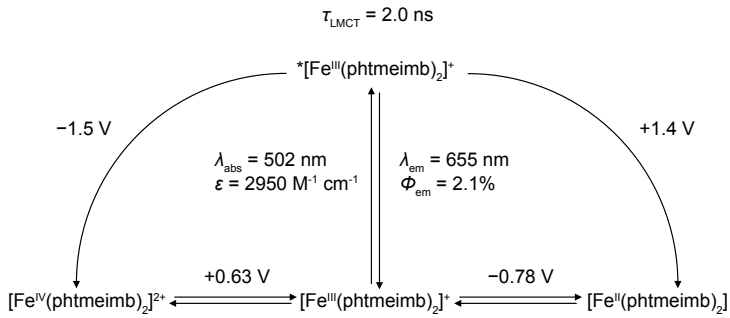

Figure 8. Latimer diagram displaying key electrochemical and photophysical properties of $[Fe(phtmeimb)_2]^+$. All potentials are given vs SCE. They were originally measured vs $Fc^{+/0}$ in acetonitrile[38] and converted using a conversion constant of +0.38 V.[58]

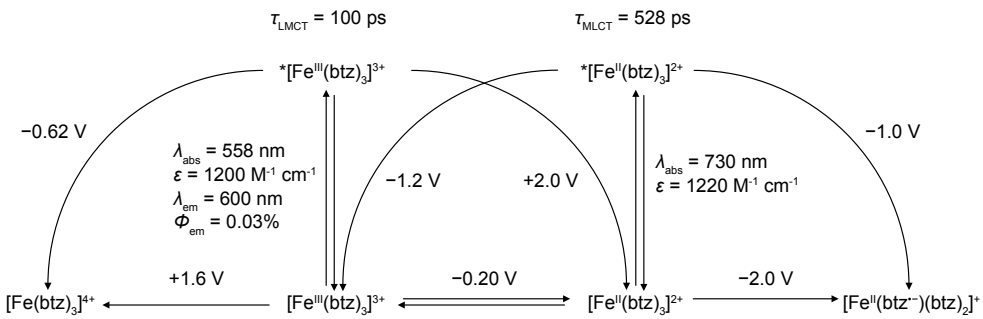

Figure 9. Latimer diagram displaying key electrochemical and photophysical properties of $[Fe(btz)_3]^{3+/2+}$. All potentials are given vs SCE. They were originally measured vs $Fc^{+/0}$ in acetonitrile[36,54] and converted using a conversion constant of +0.38 V.[58] The reduction to $[Fe^{II}(btz^{\bullet-})(btz)_3]^{2+}$, as well as the oxidation to $[Fe(btz)_3]^{4+}$, are ireversible under cyclic voltammetry conditions.

The lifetimes of 100 ps to 2.0 ns are at the diffusion limit of photoredox catalysis, meaning that the electron transfer mechanisms likely would be a combination of static and dynamic quenching. One should note that electrochemical oxidation of $[Fe^{III}(btz)_3]^{3+}$ to $[Fe(btz)_3]^{4+}$ is irreversible, and the corresponding species has never been isolated. It therefore remains unclear if this species is oxidised on the metal or on the ligand.[36,54] Similarly, the reduced species beyond $[Fe^{II}(btz)_3]^{2+}$, which most probably is reduced on the ligand, has never been isolated, and the reduction is irreversible on the timescale of cyclic voltammetry.

1.3 Synthesis of iron *N*-heterocyclic carbene complexes

The very first example of an iron NHC complex was reported in 1969, by Öfele. By reacting $K[FeH(CO)_4]$ and 1,3-dimethylimidazolium iodide, the tetracarbonyl Fe-NHC complex was obtained (Fig. 10, Path A).[59] The iron-hydride functioned as a base, deprotonating the imidazolium before coordination. The next development in the synthesis of iron NHC complexes was achieved by Lappert and co-workers in 1973, when they replaced one carbonyl ligand in $[Fe(CO)_5]$ with a carbene by heating the complex with the NHC dimer in benzene for 1 h (Path B).[60] However, both of these methods have the drawback that only one NHC ligand can be installed per complex.

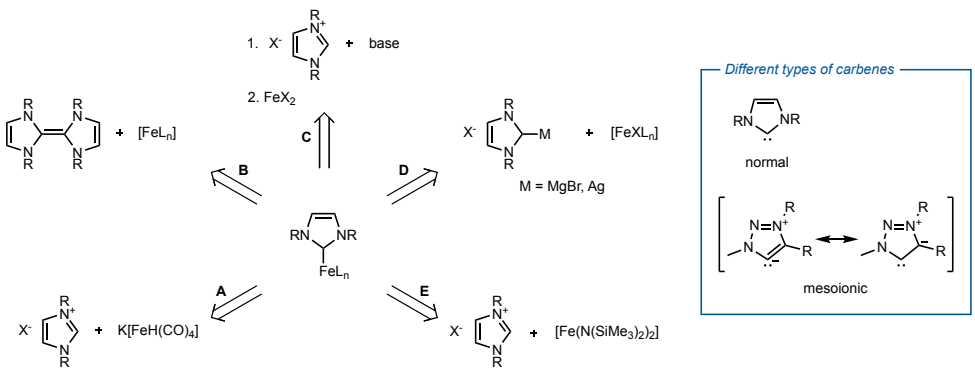

Figure 10. Left: Common synthetic paths toward iron NHC complexes. Adapted with permission from ref. 61. Copyright 2014 American Chemical Society. Right: *N*-heterocyclic carbenes can be divided into two types: normal and mesoionic carbenes. R can be the same or different in the same carbene.

A major breakthrough in the synthesis of iron NHC complexes came in 1996. The group of Fehlhammer discovered that by using a strong base, the corresponding imidazolium salt could be deprotonated and reacted with an iron halide (Path C).[62] This now meant that any number of NHC ligands could be combined with an iron

precursor, and iron complexes with more than one NHC ligand became attainable. This synthetic protocol has since been developed and a range of bases such as *n*-butyllithium, sodium hydride, lithium diisopropylamide (LDA) and most importantly, potassium *tert*-butoxide are nowadays used.[61] Curiously, it was a derivative of this first hexacarbene iron complex synthesised by Fehlhammer that 23 years later was the first iron complex, $[Fe(phtmeimb)_2]PF_6$, that was discovered to have a nanosecond lifetime of the ^{2}LMCT state.[38]

Smith and co-workers reported a variation of this method in 2005, when they reported the transmetallation from an isolated magnesium carbene to $FeBr_2$ (Path D).[63] They formed the magnesium carbene from the corresponding imidazolium salt using a Grignard reagent as a strong base. The border between path C and path D is diffuse, as it is not always clear if the carbene is actually coordinating to the metal, or if the metal is acting more as a counterion. Apart from magnesium carbenes, also silver carbenes, formed using Ag_2O as the silver source, have been used for transmetallation to iron.[64]

The latest development in the synthesis of iron NHC complexes is the use of $[Fe(N(SiMe_3)_2)_2]$, first described by Danopoulos (Path E).[65] Much like the first reagent for the synthesis of iron NHC complexes, $K[FeH(CO)_4]$, this reagent has the strong base already integrated in the iron precursor. This means that every equivalent of $[Fe(N(SiMe_3)_2)_2]$ can only deprotonate two NHC precursors. Unfortunately, the moisture sensitivity of $[Fe(N(SiMe_3)_2)_2]$ makes both the preparation and use of this reagent cumbersome.

Finally, one can note that the syntheses of iron NHC complexes, in particular those bearing several NHC ligands, give very erratic yields. In the literature, there are several examples where synthetic methods are successful in one research group, but not in another.[38,50,63,66] The reasons for these discrepancies are unclear, but apart from the moisture- and air-sensitive nature of these syntheses, the temperature and timing of the addition of the reagents seem to play an important role.

NHCs can be classified into two different classes, normal and mesoionic carbenes, the later one is sometimes also referred to as "abnormal" carbenes (Fig. 10, right). While the first type can be drawn so that all atoms are charge neutral, it is impossible to draw a resonance form of the mesoionic carbene without any formal charges. The latter one is usually thought to have slightly better π-accepting properties than the former, as well as stronger σ-donation.

1.4 Photocatalysis

Before exploring iron based photocatalysis, it is beneficial to take a look at photocatalysis in general, and in particular at the requirements for successful photocatalysis. Photocatalysis differs from conventional catalysis in that it can drive thermodynamically uphill reactions, using the absorbed light energy. Upon light absorption, the photocatalyst gets excited into a high-energy state. The energy now stored in the photocatalyst can be transferred either as energy — putting a substrate molecule into the excited state — or used to transfer an electron or a hole, effectively reducing or oxidising the substrate molecule (Fig. 11). There are two possibilities for energy transfer, the first one being Dexter energy transfer, which essentially is an exchange of an excited electron in the photosensitiser for a ground state electron from the substrate.[67] Another possibility is Förster resonance energy transfer, where the energy is transferred through dipole-dipole coupling.[68] Although energy transfer photocatalysis is not as widespread as photoredox catalysis through single electron transfer (SET), truly fascinating applications exist, such as enantioselective photocatalysis[69] and photochemical deracemization reactions[70]. In this thesis the term "photocatalyst" (PC) is used in the context of organic synthesis, while "photosensitiser" (PS) is employed in the context of artificial photosynthesis. That said, the same compound can function both as a photocatalyst and as a photosensitiser.

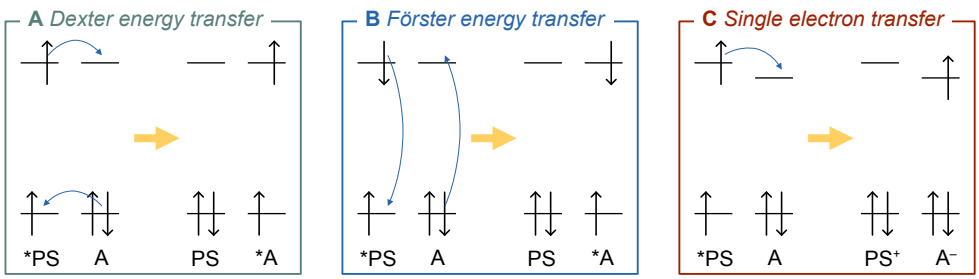

Figure 11. (A) Dexter energy transfer (B) Förster energy transfer (C) Single electron transfer. Note the conservation of spin in all processes. Adapted from ref. 71 with permission from the Royal Society of Chemistry.

1.4.1 Photoredox catalysis

A different type of photocatalysis, photoredox catalysis which proceeds through outer-sphere SET, has reached more widespread application than photocatalysis through energy transfer. Photoredox catalysis is a means to generate open shell intermediates (radicals) under mild conditions. Conventional radical chemistry relies on radical initiators and mediators, which have inherent safety issues. These can typically be intense UV-light, toxic tin reagents or explosive azobisisobutyronitrile (AIBN) and

peroxides, which can be avoided by instead using photoredox catalysis. Photoredox catalysis instead relies on visible light and a light absorbing photocatalyst. Furthermore, photoredox catalysis has enabled reactivity which was not previously attainable, such as alcohol-alcohol cross couplings[72], and can utilise highly reducing or oxidising excited states. The photoredox catalysts are usually noble metal complexes such as $[Ru^{II}(bpy)_3]^{2+}$ and $[Ir^{III}(dF(CF_3)ppy)_2(dtbbpy)]^+$ ($dF(CF_3)ppy$ = 2-(2,4-difluorophenyl)-5-(trifluoromethyl)pyridine, dtbbpy = 4,4'-di-*tert*-butyl-2,2'-bipyridine).[8,73] These complexes have the advantage of intense absorption of UV-vis light and redox potentials that provide a strong thermodynamic driving force for SET. Organic dyes such as Eosin Y and first-row metal transition metal complexes, notably copper complexes, have also found widespread applications.[74,75] Although proponents of organic dyes emphasise their sustainability due to the lack of a metal, organic dyes generally suffer from poor photostability. Transition metal complexes also have the advantage of easy tuning of their properties by ligand modification.

Seminal papers in photoredox catalysis were published in 2008, when MacMillan published an asymmetric alkylation of aldehydes[76], and Yoon published a [2+2] enone cycloaddition[77]. Shortly thereafter, Stephenson published a reductive dehalogenation reaction[78], also driven by irradiation of $[Ru(bpy)_3]Cl_2$, and the interest in photoredox catalysis exploded. It might therefore seem like the field is rather young. The groundwork was however done already in the 1970s,[9,79,80] and $[Ru(bpy)_3]Cl_2$ was first synthesised in 1936.[8]

A typical photoredox catalytic cycle goes through several elementary steps, the first being light absorption. Light of the right colour is absorbed by the photoredox catalyst and excites it into an excited state. The excited state will typically be both more reducing and more oxidising than the ground state because of the simultaneous presence of an excited electron and a hole (Fig. 12A).

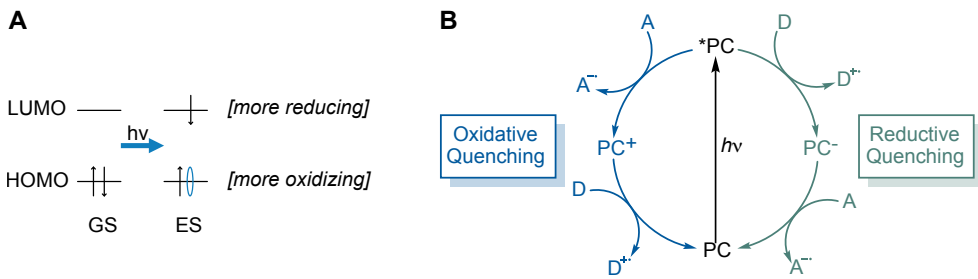

Figure 12. (A) The excited state of a photoredox catalyst is both more reducing and more oxidising than the ground state, due to the simultaneous presence of a high energy excited electron and a hole in the previous HOMO. (B) Simplified general description of photoredox catalysis through single electron transfer. PC = photoredox catalyst, A = electron acceptor, D = electron donor.

After excitation, the photoredox catalyst can interact with a suitable quencher (Fig. 12B). This can proceed in two fashions, either through oxidative quenching, where the PC gets oxidised and the quencher reduced by one electron, or vice versa, through reductive quenching, where the PC gets reduced, and the quencher oxidised. The quencher of the excited state can either be the substrate itself or it can be a sacrificial quencher. The PC, which now is either reduced or oxidised, needs to undergo another SET in the opposite direction in order to return to the original ground state. Direct SET from the excited *PC to the substrate is advantageous in the sense that the full thermodynamic driving force can be used; however, this requires the substrate to react fast enough with the *PC before deexcitation. Often sacrificial reductants/oxidants are used in large concentrations to ensure efficient quenching of the *PC.[81]

1.4.2 Kinetics of photoredox catalysis

The reaction outcome of a photoredox catalysis reaction depends on the kinetics and other parameters of the different fundamental steps involved (Scheme 1). The first parameter to consider is the absorption spectra of the PC. The wavelength of the absorption maximum (λ_{abs}) determines what colour of light that can be used. The preferential wavelength may differ depending on the application. For a photocatalyst that is envisioned to work with solar light or UV-absorbing substances, a λ_{abs} in the visible region is desirable. On the other hand, to have a strong driving force for chemical reactions, a large band gap might be required, and thus a λ_{abs} in the near-UV or even UV-region is preferential. Furthermore, the extinction coefficient ε determines the amount of light absorbed at a specific concentration of PC.

$PC + h\nu \rightarrow {}^*PC$	λ_{abs}, ε	(2)
${}^*PC \rightarrow PC + h\nu$	k_r, τ	(3)
${}^*PC \rightarrow PC + \text{heat}$	k_{nr}, τ	(4)
${}^*PC + Q \rightarrow [PC^- + Q^+]$	k_q, η_q	(5)
$[PC^- + Q^+] \rightarrow PC + Q$	k_{rET}	(6)
$[PC^- + Q^+] \rightarrow PC^- + Q^+$	k_{ce}, η_{ce}	(7)
$PC^- + Q^+ \rightarrow PC + Q$	k_{bd}	(8)
$PC^- + S \rightarrow PC + S^-$	k_s	(9)

Scheme 1. The different steps involved in photoredox catalysis and their associated parameters, here exemplified by reductive quenching of the photoredox catalyst. Q = quencher, S = substrate, k_r = rate of radiative decay, k_{nr} = rate of nonradiative decay, k_q = rate of quenching, η_q = quenching yield, k_{rET} = rate of in-cage reverse electron transfer, k_{ce} = rate of cage escape, η_{ce} = cage escape yield, k_{bd} = rate of back donation after cage escape, k_s = rate of SET to the substrate. Adapted with permission from ref. 82. Copyright 1987 American Chemical Society.

The steps in scheme 1 will be discussed for a reductive mechanism, the corresponding steps for an oxidative mechanism are identical (apart from the charges being inverted). Upon excitation of the photocatalyst, the non-productive routes (Scheme 1, eq. 3, 4, 6, 8) will be in direct competition with the productive routes (eq. 5, 7 9). After excitation, the *PC can relax back to the ground state both radiatively (eq. 3) and nonradiatively (eq. 4). Only if the quenching rate k_q by the quencher Q is faster than these relaxation steps can the PC be reduced via SET. The quenching yield η_q gives the fraction of *PC that undergoes quenching, which for photoredox catalysis is the same as the fraction of the absorbed photons that result in electron transfer. The additional possibility of energy transfer is not shown in scheme 1.

After SET, the PC^- and Q^+ will remain within close contact in the solvent cage. Here again, an unproductive in-cage reverse electron transfer (eq. 6) could occur if the rate of cage escape k_{ce} is too low. The cage escape yield η_{ce} gives the fraction of quenched PC that escapes the solvent cage, and the product of η_{ce} and the quenching efficiency η_q gives the quantum yield of charge separated products: $\Phi_{cs} = \eta_q\eta_{ce}$. The quantum yield is thus the fraction of absorbed photons that result in cage-escape products PC^- and Q^+, and therefore a key number when determining the efficiency of a photoredox catalysis reaction.[83]

Unfortunately, even after cage escape, charge back donation between PC^- and Q^+ back to PC and Q can occur (eq. 8), and electrostatic attraction between the charge-separated products may even favour this. This can be counteracted in different fashions, such as having the reduced PC^- being overall charge neutral, thus eliminating these electrostatic attractions. Another way is to use a quencher that rapidly decomposes upon quenching, which effectively removes Q^+ from the reaction mixture.[81] Finally, the reduced PC^- can reduce the substrate, driving the chemical reaction and restoring the PC to the ground state where it is again available for excitation.

Another important factor, which is sometimes overlooked in photoredox catalysis, is how well the PC survives all the above-mentioned steps. Ideally, all involved states of the photocatalyst should be stable under the reaction conditions. For $[Ru(bpy)_3]^{2+}$ a general problem is ligand dissociation in the excited state, via thermal activation of the ^{3}MC state, leading to decomposition of the photocatalyst.[84]

1.4.3 Cage escape yield

As alluded to above, an important but not well understood factor for the outcome of photoredox catalysis reactions is the cage escape yield η_{ce}.[82,83,85] Following the electron transfer between the photoredox catalyst and the quencher, they form a charge separated pair within the solvent cage (Fig. 13).

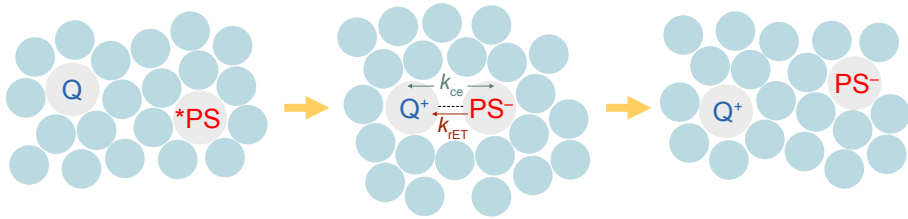

Figure 13. Schematic illustration of the cage escape following reductive quenching of a photosensitiser (PS) by a quencher (Q), and relevant kinetic parameters (k_{ce} and k_{rET}). The blue circles represent solvent molecules.

What then determines the quantum yield is the cage escape yield, given by the relative rates of the reverse electron transfer k_{rET} and cage escape k_{ce}, as shown in equation 10. This is because once the charge separated products have escaped the solvent cage, the probability of them recombining is diffusion controlled and therefore much lower than within the solvent cage.

$$\eta_{ce} = \frac{k_{ce}}{k_{ce}+k_{rET}} \qquad (10)$$

It is speculated that the rate of k_{rET} depends on factors such as spin-state, thermodynamic driving force for the reverse electron transfer and localisation of the charges.[85] Upon excitation of a d^6 complex to the ^{1}MLCT state, it typically undergoes fast intersystem crossing to the ^{3}MLCT state. Spin-allowed (reductive) quenching of this state by a closed shell quencher will result in an in-cage pair $^3\{PC^{\bullet-}$ --- $Q^{\bullet+}\}$. In-cage reverse electron transfer back to form the ^{1}PC and ^{1}Q is now spin forbidden (Fig. 14). The slow, spin-forbidden reverse electron transfer means that d^6 complexes usually exhibit large cage escape yields.

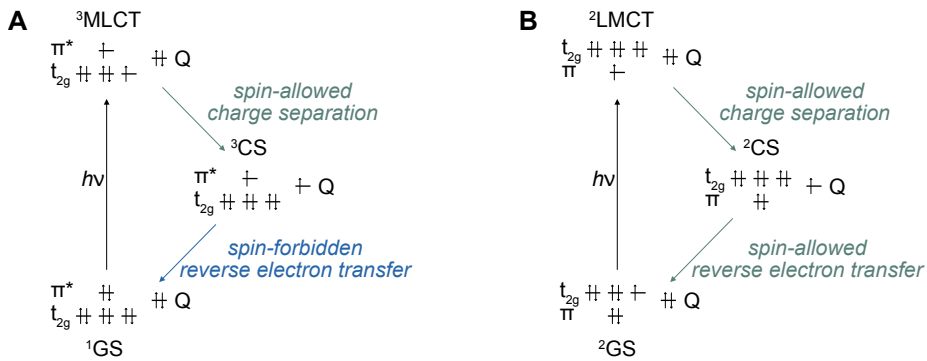

Figure 14. Schematic representation of the reductive quenching of (A) a ^{3}MLCT state and (B) a ^{2}LMCT state. Note that the excited state in (A) is shown after ISC ^{1}MLCT → ^{3}MLCT.

The case for d^5 complexes is different, since the spin-allowed reductive quenching of the ^{2}LMCT state will yield the charge separated pair $^2\{PC^{\bullet-}$ --- $Q^{\bullet+}\}$. From here, reverse electron transfer to form ^{2}PC and ^{1}Q is spin allowed, possibly increasing k_{rET} and hampering high cage escape yields for these complexes.

Another hypothesis, with some evidence, is that in-cage reverse electron transfer can happen within the inverted Marcus regime.[85] Semi-classical Marcus-theory states that reaction rates increase with increasing thermodynamic driving force, up until a point where the driving force equals the reorganisation energy. From there, the reaction rate decreases again, forming a parabola (Fig. 15).[86–89] If the reverse electron transfer occurs in the inverted Marcus regime, the driving force for back electron transfer should be maximised in order to slow down k_{rET}. Given this, photoredox catalysts should be designed to make in cage reverse electron transfer as exergonic as possible, in order to optimise for high cage escape yields. This could possibly be achieved by designing strong photo-reductants/oxidants, in combination with high excited state energies. Unfortunately, this might conflict with another target in artificial photosynthesis and photoredox catalysis; to use low energy light for better spectral overlap with sun light and fewer side reactions.

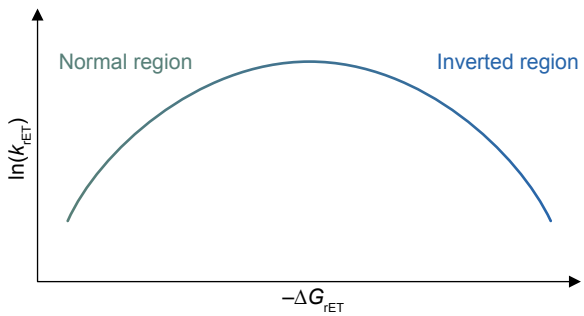

Figure 15. Generic Marcus parabola illustrating the dependence of the rate constant for in-cage reverse electron transfer (k_{rET}) on its driving force (ΔG_{rET}).

Obvious from equation 10, the cage escape yield also depends on the rate of cage escape, k_{ce}. This factor depends on many different properties of the system, including electrostatic forces[90], solvent polarity and viscosity[50,91–94], ionic strength and ion-pairing[93–96], and temperature[93,94,97]. Many factors of a reaction system, including the solvent and additives, are therefore necessary to optimise, as the cage escape yield has a determining effect on the overall yield of a photoredox catalysis reaction.[85]

1.4.4 Photoredox catalysis with iron complexes

Iron based photoredox catalysis can proceed through three main mechanisms: (1) Inner-sphere electron transfer resulting in bond homolysis (2) Outer-sphere electron transfer from an MC state (3) Outer-sphere electron transfer from a CT state.[98]

The first reaction mechanism typically proceeds by coordination of a carboxylate to an iron salt. Near-UV or UV irradiation will then homolytically cleave the Fe-O bond, followed by expulsion of carbon dioxide which leads to a carbon centred radical that can go on and react with a radical acceptor. Another reaction operating by the same type of mechanism is the generation of Cl-radicals from $FeCl_3$ by near-UV irradiation. The formed Cl-radicals in turn act as radical initiators in the product forming reaction.

The second class of reaction mechanisms, still rather limited, is outer-sphere SET from an MC state of an iron complex. There are a few examples of Fe-polypyridyl complexes, with short-lived CT states that are still capable of driving photoredox catalysis from their MC states.[17,99] This reaction mode however means that a significant part of the absorbed light energy is lost as heat.[100]

Finally, the last and emerging class of iron photoredox catalysis is outer sphere SET from a CT state, a mechanism that has been made possible by the extended lifetimes of the CT states of iron complexes in recent years. This mode of action is the subject of the photoredox catalysis part of this thesis. Photoredox catalysis using CT states has several advantages over that using MC states. As CT transitions are spin- and Laporte allowed, the absorption of these bands is much stronger than the MC bands. Furthermore, direct utilisation of the CT state harnesses a larger part of the excitation energy, since energy is lost in the IC from a CT state to an MC state. A CT state also already implies some charge separation within the photoredox catalyst, contrasting MC states where the excitation is on the metal core itself.[27] Early quenching studies had shown bimolecular quenching of the ^{2}LMCT state of $[Fe(phtmeimb)_2]^+$, thus laying the foundation for photoredox catalysis being possible with these new iron complexes.[38,47]

Concurrent with our studies into photoredox catalysis with $[Fe(phtmeimb)_2]^+$ and $[Fe(btz)_3]^{3+}$, several other research groups were working on the same topic. The first study showcasing the use of a CT state of an iron complex for photoredox catalysis was published by the group of Troian-Gautier in 2021. In the article, they applied $[Fe(phtmeimb)_2]^+$ in a dehalogenation reaction with excellent yields, and in a follow-up paper they expanded the methodology to a ring closing atom transfer reaction (Scheme 2).[50,101]

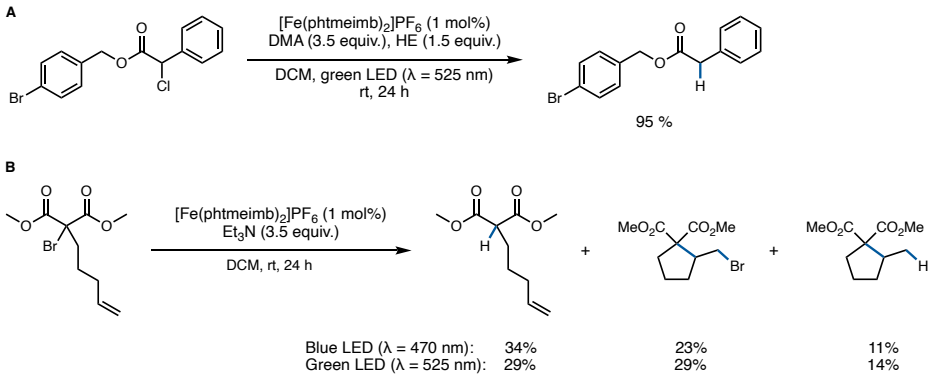

Scheme 2. (A) Dehalogenative hydrogen atom transfer reaction using $[Fe(phtmeimb)_2]^+$ as developed by Troian-Gautier. HE = Hantzsch ester, DMA = dimethylaniline. Isolated yield. (B) Ring-closing atom transfer reaction using $[Fe(phtmeimb)_2]^+$ as developed by Troian-Gautier.[50,101] ^{1}H-NMR yields. Adapted with permission from ref. 98.

Shortly after that, the group of Kang published a radical cationic [4+2] cycloaddition reaction driven by green light irradiation of $[Fe(btz)_3]^{3+}$ (Scheme 3).[102]

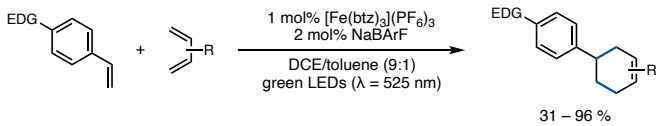

Scheme 3. Radical cationic [4+2] cycloaddition reaction driven by green light irradiation of $[Fe(btz)_3]^{3+}$ as developed by the group of Kang.[102] All yields are isolated yields. DCE = 1,2-dichlorethane, NaBArF = sodium tetrakis[3,5-bis(trifluoromethyl)-phenyl]borate, EDG = Electron Donating Group. Adapted with permission from ref. 98.

Taken together with the studies from our group, these reactions show the broader applicability of iron NHC complexes in photoredox catalysis and that this field has the potential to expand further.

1.5 Methods

The iron complexes in this thesis, as well as the artificial photosynthesis and photoredox catalysis reactions, have been studied by several methods and techniques. These will be shortly described below.

1.5.1 Steady-state absorption and emission spectroscopy

The steady-state absorption spectrum of a metal complex is determined by the intensity of the different transitions. At a given wavelength, the absorbance (A) is given by the Beer–Lambert law:

$$A = -\log\left(\frac{I_{tr}}{I_0}\right) = \varepsilon c l \qquad (11)$$

where I_{tr} is the intensity of the transmitted light, I_0 is the intensity of the incident light, ε is the molar absorption coefficient, c is the concentration of the analyte and l is the path length of the cell.

Using a fluorescence spectrometer one can obtain the emission spectra of luminescent compounds. The emission spectra will be redshifted compared to the absorption spectra. This wavelength shift, called Stokes-shift, is due to energy losses in the form of heat, when the excited state relaxes down to the emissive state. After a molecule absorbs a photon, it relaxes to the lowest excited state before emitting light (Kasha's rule), resulting in the emission occurring at a longer wavelength (lower energy) than the absorbed light. The absorption and emission spectra therefore provide crucial information about the $E_{0\text{-}0}$ transition, which is the energy difference between the lowest vibrational level of the ground state and the lowest vibrational level of the first excited electronic state. The wavelength at the intersection of the normalised absorption and emission spectra gives the $E_{0\text{-}0}$ energy, which can then be used to calculate excited state redox potentials (see electrochemistry section).

The emission quantum yield Φ_{em} is defined as the ratio between the number of photons emitted and the number of photons absorbed (eq. 12).[103]

$$\Phi_{em} = \frac{n_{\text{photons emitted}}}{n_{\text{photons absorbed}}} = \frac{I_{em}}{I_{abs}} \qquad (12)$$

It is often determined relative to a substance with a well-defined emission quantum yield, such as $[Ru(bpy)_3]^{2+}$.

The quantum yield can also be defined as a relationship between the different rate constants

$$\Phi_{em} = \frac{k_r}{k_r + k_{nr}} = \frac{k_r}{k_0} \qquad (13)$$

where k_r is the radiative rate constant, k_{nr} is the nonradiative rate constant and $k_0 = k_r + k_{nr}$. This means that Φ_{em} in combination with transient absorption spectroscopy can be used to get insights into the different rate constants in the excited state.

1.5.2 Transient absorption spectroscopy

All excited state dynamics in this thesis have been determined by transient UV-vis absorption spectroscopy. The principle behind this is simple, although it practically relies on advanced techniques. The excited state of a molecule will have a different absorption spectrum than the ground state. This can be used by passing two light pulses through a sample, the first one (pump) to excite the complex, and the second (probe) to measure the absorption of the sample after excitation. Analysing the difference between excited state absorption and ground state absorption (ΔOD, OD = optical density) will reveal two main features, excited state absorption (ESA) and ground state bleach (GSB). ESA will show at wavelengths where the extinction coefficient of the excited state is higher than that of the ground state. GSB will vice versa show at wavelengths where the excited state has a lower extinction coefficient than the ground state. By varying the time between the first and second light pulse, we can measure how fast different processes in and around the complex happen. Current state-of-the-art techniques have fs time resolution thanks to high precision optical delay stages. This allows us to get the kinetics for the decay of the different excited state. The radiative and nonradiative decay of an excited state can be described by

$$-\frac{\mathrm{d[ES]}}{\mathrm{d}t} = k_\mathrm{r}[\mathrm{ES}] + k_\mathrm{nr}[\mathrm{ES}] = k_0[\mathrm{ES}] \qquad (14)$$

where [ES] is the concentration of the excited state and t is the time.[103] This equation can be integrated to give

$$[\mathrm{ES}] = [\mathrm{ES}]_0 e^{-k_0 t} \qquad (15)$$

The lifetime τ of an excited state is furthermore defined as

$$\tau = \frac{1}{k_\mathrm{r}+k_\mathrm{nr}} = \frac{1}{k_0} \qquad (16)$$

By inserting $k_0 = \tau^{-1}$ (eq. 16) and $t = \tau$ into equation 15, we can obtain that the lifetime τ of an excited state represents the time required to reduce the number of molecules, that populate this excited state, to $e^{-1} \approx 37\%$ of the initial population.

Transient absorption spectroscopy can also be used to calculate the cage escape yield, by comparing the quenching yield of the excited state to the formation of cage escape products, since the quantum yield of charge separated products Φ_{cs} is defined as

$$\Phi_\mathrm{cs} = \eta_\mathrm{q}\eta_\mathrm{ce} \qquad (17)$$

where η_q is the quenching yield and η_{ce} is the cage escape yield. η_q can be determined by Stern–Volmer analysis, see below. Luminescence lifetimes can also be determined by

time correlated single photon counting, but transient absorption spectroscopy can give additional insights into the excited state deactivation dynamics, not visible by other techniques.

1.5.3 Stern–Volmer analysis

Two types of quenching of an excited state exist, as well as a combination between the two. These two types are dynamic (or collisional) quenching, and static quenching (Fig 16). In dynamic quenching, the PS and the quencher are free in solution, and may occasionally collide with each other. Upon excitation of the PS, it will, if luminescent, emit light. Some of the *PS will collide with a quencher (Q) before radiative decay occurs, and the emission will be quenched. If we increase the concentration of quencher, the likelihood that an *PS collides with a Q increases, and both the emission intensity as well as the excited state lifetime of the emissive state will decrease.

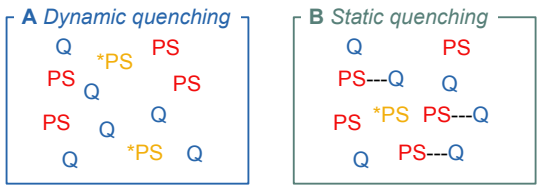

Figure 16. The two types of quenching. (A) Dynamic quenching (B) Static quenching.

The other type of quenching is static quenching. Here, some of the PS are already in close contact with a quencher. Upon excitation of one of these close contact pairs, the *PS will be quenched instantly, before any emission can occur. Effectively, it is as if some of the PS have been removed from the solution, and with increasing quencher concentrations, the emission will decrease. Some PS will remain free in solution, and upon excitation of these, they will emit light. Given that there is no dynamic quenching, the excited state lifetime of these *PS will be *exactly as if no quencher at all was present*. With static quenching, we will therefore see a decrease of the emission intensity upon added quencher, but no change in excited state lifetime. Often a combination of static and dynamic quenching is operating, in particular at high quencher concentrations.

The excited state quenching of a photosensitiser can hence be investigated using steady-state and transient UV-vis absorption spectroscopy. By measuring the emission intensity and excited state lifetimes at different quencher concentrations, a Stern–Volmer plot can be constructed, which allows us to determine important reaction parameters such as the quenching rate.[103,104] However, a Stern–Volmer analysis will not be able to distinguish between different quenching mechanisms such as energy transfer

and electron transfer, as both types of quenching will reduce the emission (and excited state lifetime). The comparison of emission Stern–Volmer plots and excited state lifetime Stern–Volmer plots enables us to differentiate between static and dynamic quenching. The Stern–Volmer equation for dynamic emission quenching is

$$\frac{I^0_{em}}{I_{em}} = 1 + K_{SV}[Q] = 1 + k_q\tau_0 \cdot [Q] \qquad (18)$$

where I^0_{em} and I_{em} are the emission in the absence and presence of quencher, respectively, K_{SV} is the Stern–Volmer constant, k_q is the quenching rate, τ_0 is the lifetime of the emissive state without quencher present and [Q] is the quencher concentration. By plotting I^0_{em} / I_{em} vs [Q] we can obtain the Stern–Volmer constant from the slope of the curve, and furthermore, if we know the excited state lifetime τ_0 of the photoactive state we can obtain the quenching rate k_q.

The other variant of quenching is static quenching, where the photocatalyst and the quencher are already in close contact before the quenching event. By comparing the Stern–Volmer plot based on excited state lifetimes (eq. 19) with that of the luminescence quenching, we can differentiate between dynamic quenching, static quenching, and a combination of the two (Fig. 17).

$$\frac{\tau_0}{\tau} = 1 + K_D[Q] \qquad (19)$$

From equation 19, where τ_0 and τ are the excited state lifetimes in the absence and presence of quencher, respectively, and K_D is the dynamic quenching component, we can see that a plot of τ_0 / τ vs [Q] will give a straight horizontal line in the case of pure static quenching (where K_D = 0). In many cases, a combination of static and dynamic quenching is operating, which will give a quadratic plot for the emission quenching, and a straight line for τ_0 / τ vs [Q] (Fig. 17C).

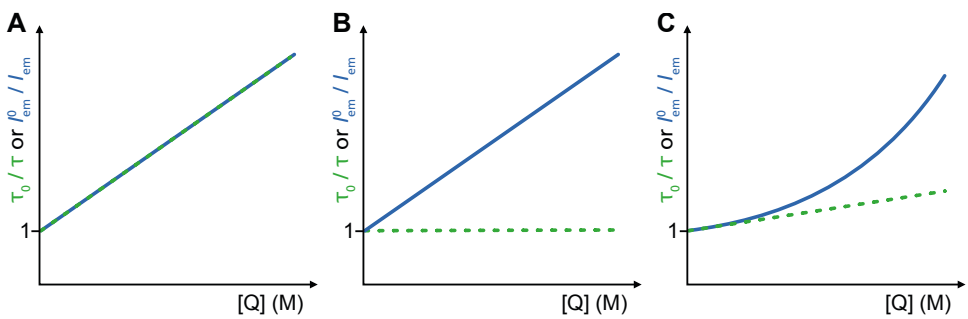

Figure 17. Schematic Stern–Volmer plots displaying (A) dynamic quenching (B) static quenching and (C) a combination of dynamic and static quenching. Blue solid line: Steady-state emission data. Green dashed line: Time-resolved emission data. Adapted from ref. 105.

1.5.4 Electrochemistry

Knowledge of the reduction and oxidation potentials of a photocatalyst is important for predicting reactivity. By comparing the reduction and oxidation potentials of the photocatalyst to the quencher or substrate, one can estimate if the reaction is thermodynamically feasible. The rate of electron transfer also depends on kinetic parameters, such as the reorganisation energy and the electronic coupling between the photocatalyst and the quencher. This means that even if the reaction has a thermodynamic driving force, the kinetics might still not be favourable.[103] The reduction and oxidation potentials of a photocatalyst can be measured using cyclic voltammetry. The photocatalyst is then dissolved in an electrolyte solution in an electrochemical cell. A setup consisting of a working electrode, a counter electrode and a reference electrode is immersed in the solution, and the cell is purged with an inert gas. The applied potential at the working electrode is then gradually changed as a function of the reference electrode potential, until a set point, and the sweep direction is then reversed. The resulting current is recorded, and a plot of current vs applied potential reveals any reduction or oxidation events. For a reversible reduction/oxidation, the midpoint between the peak currents gives the halfwave potential ($E_{½}$). The value is recorded against a reference redox couple, which for organic solvents typically is the reversible oxidation of Ferrocene ($Fc^{+/0}$). The $E_{½}$ corresponds to the point where half of the analyte is oxidised/reduced, comparable to the pK_a value in acid-base chemistry.

By combining the $E_{½}$ with the estimated excited state energy $E_{0–0}$ obtained from absorption and emission spectroscopy, we can calculate the excited state reduction and oxidation potentials of a photosensitiser (PS) according to the Rehm-Weller equations[106,107]

$$E(PS^{+}/{}^{*}PS) = E_{½}(PS^{+}/PS) - E_{0–0}({}^{*}PS/PS) \quad (20)$$

$$E({}^{*}PS/PS^{-}) = E_{½}(PS/PS^{-}) + E_{0–0}({}^{*}PS/PS) \quad (21)$$

In these equations, it is assumed that all the excited-state energy is fully available, with any additional contributions — such as Coulombic or entropic interactions between the reactants and/or the solvent — being neglected. This approximation is generally acceptable in polar solvents.[103,108]

1.5.5 Actinometry

The photoredox catalysis and hydrogen evolution reactions presented in this thesis were studied using chemical actinometry. This method gives the product quantum yield (Φ_{prod}) of a reaction, that is how many moles of product are formed per mole of absorbed photons.

$$\Phi_{prod} = \frac{n_{\text{prod}}}{n_{\text{photons absorbed}}} \tag{22}$$

Practically, Φ_{prod} is often determined by comparative actinometry. This is done by running a reference reaction with a well-known quantum yield, using the same light source as for the reaction of interest. By matching the absorbance of the reference reaction with the reaction of interest, and accurately determining the yield, one can calculate the number of photons absorbed in a certain time period. Comparison of this value to the yield, in the same time period, of the reaction of interest allows for the determination of the quantum yield. Originally, the decomposition of potassium ferrioxalate was used as a standard actinometer, however, nowadays a range of different systems are available, suitable for different wavelengths.[109] Φ_{prod} can give insight into whether a chain propagation mechanism is operating or not. If $\Phi_{prod} > 1$, a chain propagation mechanism must be operating. A $\Phi_{prod} < 1$ does however not disprove a chain propagation mechanism, as the low efficiency could be due to low yields of the different elemental steps preceding product formation, such as the quenching and cage escape steps.

1.6 Aim of the thesis

This thesis has two overarching aims. The first is to increase the excited state lifetimes of iron complexes in order to make them more competent as photosensitisers and photocatalysts. The second aim is to apply iron complexes as photosensitisers in artificial photosynthesis and photoredox catalysis, which are traditionally run using noble metal photosensitisers and photocatalysts.

In order to achieve this, we need to better understand the photophysics and photochemistry of iron complexes. The idea behind this is that if we understand the photophysics and photochemistry, we can also control it. Thereby we can design new iron complexes with improved properties for use as photoredox catalysts and photosensitisers. Understanding the photophysics and photochemistry, we can design based on rational reasoning.

In the first two papers, the objective was to introduce an activation barrier for conversion from the CT states to MC states, thereby extending the CT state lifetimes. In Paper I, the hypothesis was that an extended π-system on the ligand would lover the energy of the CT states, increasing the activation barrier for deexcitation through MC states. Paper II proposed that incorporating a strongly σ-donating and π-accepting cyclometallated phenyl group, in combination with NHC ligands, would increase the ligand field splitting, raising the MC state energies and potentially slow down deactivation through these states.

The goal of Paper III was to develop a technique to streamline gas analysis in the field of artificial photosynthesis. The hypothesis was that by utilising rotational Raman spectroscopy, gas compositions could be analysed rapidly and non-invasively.

In Paper IV, the objective was to demonstrate the use of iron complexes as a competent photosensitiser, in the context of a hydrogen evolution reaction. Despite the rather short excited state lifetime, we knew that $^*[Fe(phtmeimb)_2]^+$ could be quenched by amines, and we hypothesized that this could be used to to drive a hydrogen evolution reaction.

Finally, in Paper V, the atom transfer radical addition reaction was used to benchmark what photoredox catalysis iron complexes are capable of. The reaction was chosen for its synthetic utility, as it installs two groups in a single reaction. The hypothesis was that the iron catalyst would operate by the same type of mechanism as more established noble metal photoredox catalysts.

2 Extending the π-system of a luminescent iron *N*-heterocyclic carbene complex to increase the barrier for internal conversion (Paper I)

The discovery of long-lived LMCT excited states of Fe^{III} complexes was a serendipity but has developed into a prosperous route.[38,52–54,110] These complexes have since then rapidly been adopted by numerous research groups for use in photoredox catalysis and artificial photosynthesis.[48,50,51,101,102,111,112] At the same time, the need for d^6 Fe^{II} complexes with long-lived ^{3}MLCT states persists for several reasons.[36,40,41] An advantage of d^6 complexes is that after excitation to the ^{1}MLCT state, they usually undergo fast ISC to the ^{3}MLCT state. From this state, fluorescence back to the ^{1}GS is spin forbidden, typically extending the lifetime of the ^{3}MLCT state. This has so far been hard to exploit in d^6 Fe^{II} complexes, as the main deactivation pathway of their ^{3}MLCT states is through IC to the ^{3}MC state. For d^5 Fe^{III} complexes, the case is reversed, as deexcitation from the ^{2}LMCT state to the ^{2}GS is spin allowed, which shortens the lifetime of the excited state.

Another reason that long-lived Fe^{II} complexes are needed is related to the spin multiplicity after electron transfer in photoredox catalysis reactions. After the fast ISC from the ^{1}MLCT state to the ^{3}MLCT state, reductive quenching can take place with a closed shell quencher, ^{1}Q. As discussed in the introduction, charge recombination within the in-cage pair $^3\{PC^{\bullet-}$ --- $Q^{\bullet+}\}$ is spin forbidden, since this would lead to a singlet ground state combination, ^{1}{PC --- Q}. It has been hypothesised that this might be the reason for the higher cage escape yields of d^6 complexes compared to d^5 complexes.[83]

With this in mind, we sought to design an iron complex where we would increase the barrier for the typical IC ^{3}MLCT → ^{3}MC. As outlined in the introduction, one strategy to achieve this is to lower the ^{3}MLCT compared to the ^{3}MC state. Lowering the ^{3}MLCT energy consists of making the metal easier to oxidise and/or the ligand easier to reduce. The second tactic is more feasible, since a large variety of possible ligands

exist, and their modification is straightforward. A challenge in this is to have a ligand that is a strong σ-donor to maintain the strong ligand field, while at the same time being a relatively good electron acceptor.

$[Fe^{III}(phtmeimb)_2]^+$ has a record long ^{2}LMCT lifetime, however, the Fe^{II} ^{3}MLCT lifetime is on the order of picoseconds.[105] This complex was therefore picked as a starting point for our design, with the goal to increase the Fe^{II} ^{3}MLCT lifetime (and possibly the Fe^{III} ^{2}LMCT lifetime). Given that modifications on the phenyl group of the ligand had no effect on the photophysical properties[110], I opted to focus on altering the imidazole NHC ligands to potentially influence the electronic structure of the complex. The chosen strategy was to lower the energy of the *π-orbital of the NHC ligands by extending the π-conjugation of the ligand.[21,24]

A first synthetic target, which had been proposed by us as well as by others[113], was to replace the methylimidazoles by methyl-benzimidazoles to obtain the phenyl tris(benzimidazol-2-ylidene)borate ligand (**8**, Fig. 18). Although a slightly weaker σ-donor, it could have more π-accepting properties and at the same maintain enough σ-donation to destabilise the MC states. Benzimidazole-NHC ligands have in the past successfully been used to increase the ^{3}MLCT lifetime of an Fe^{II} complex.[21] A version of the proposed ligand, hydrido tris(benzimidazol-2-ylidene)borate (**7**), has previously been employed in a nickel nitrosyl complex.[64] However, no instance of two ligands of this type being incorporated into a single complex has been reported.

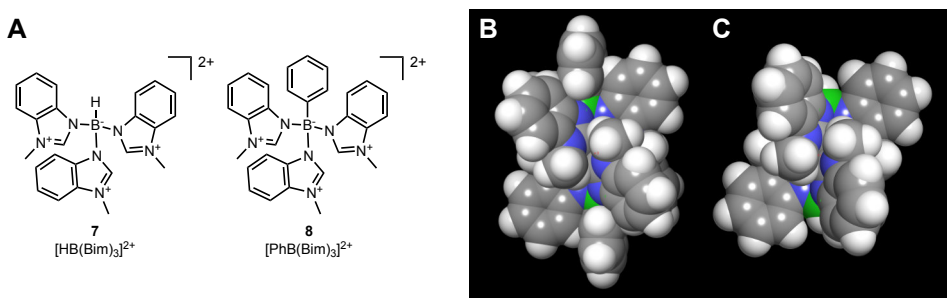

Figure 18. (A) Scorpionate pre-ligands featuring benzimidazoles. (B) Structures of $[Fe^{III}(PhB(Bim)_3)_2]^+$ and (C) $[Fe^{III}(HB(Bim)_3)_2]^+$ optimised using PBE0-D3 theory and the LANL-2DZ basis set. Displayed are the van der Waals-spheres of all atoms.

In order to assess the feasibility of the envisioned design, the potential complexes were modelled and minimised using density functional theory (DFT) calculations (Fig. 18). Each complex was modelled based on the crystal structure of $[Fe^{III}(phtmeimb)_2]PF_6$ and optimised using PBE0-D3 theory and the LANL-2DZ basis set. The computations did not point to any major steric obstacles by clashing of the ligands.

2.1 Attempted syntheses of $[Fe^{III}(PhB(Bim)_3)_2]^+$ and $[Fe^{III}(HB(Bim)_3)_2]^+$

The synthesis of the ligands was rather straightforward, following a literature synthesis for the H-substituted ligand[64] and an adapted version of the phtmeimb ligand synthesis.[38] The H-substituted ligand could be made starting from $Me_3N{\bullet}BH_3$ and bromine to obtain $Me_3N{\bullet}BHBr_2$,[114] which was used without any purification and reacted in the next step with *N*-methylbenzimidazole to give the pre-ligand 7 as a pure white salt after washing with diethyl ether and petroleum ether (Scheme 4).

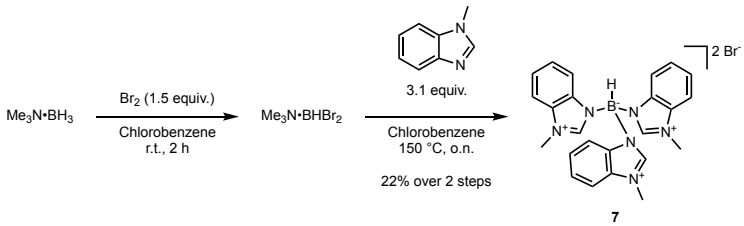

Scheme 4. Synthesis of $[HB(Bim)_3]Br_2$ (hydridotris(3-methylbenzimidazol-3-ium-1-yl)borate dibromide) pre-ligand in two steps. r.t. = room temperature.

The phenyl version of the ligand could instead be synthesised by a substitution reaction on dichlorophenylborane facilitated by the addition of trimethylsilyl trifluoromethanesulfonate (Scheme 5). When needed, the PF_6^- counterion could easily be exchanged for a bromide using tetrabutylammonium bromide in acetone.

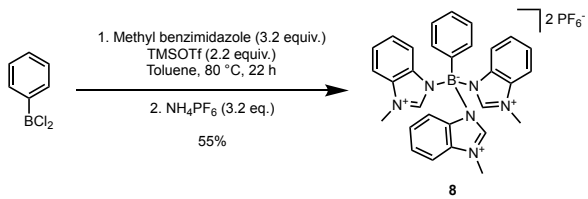

Scheme 5. Synthesis of $[PhB(Bim)_3](PF_6)_2$ (tris(3-methylbenzimidazol-3-ium-1-yl)(phenyl)borate bis(hexafluorophosphate) pre-ligand from dichlorophenylborane. TMSOTf = trimethylsilyl trifluoromethanesulfonate.

With the ligands in hand, the next step involved the coordination of the synthesised ligands with iron. This endeavour presented significant difficulties, resulting in no successful complexation. A summary of the 25 reaction conditions investigated is provided below. The first method investigated for complexation was deprotonation with a strong base, followed by addition of $FeBr_2$. Reaction conditions using potassium

tert-butoxide proved unsuccessful, even though the initial deprotonation to form the carbene should be more favoured for benzimidazole than for imidazole.

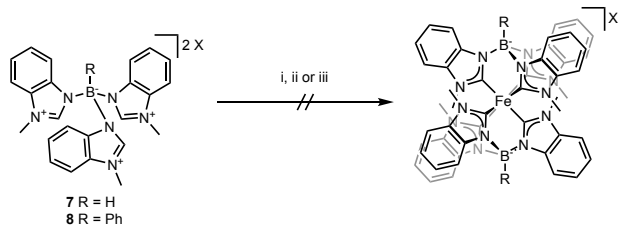

Scheme 6. Attempted syntheses of $[Fe(PhB(Bim)_3)_2]PF_6$ and $[Fe(HB(Bim)_3)_2]Br$ by deprotonation with KO^{t}Bu and coordination with $FeBr_2$. i) R = Ph, X = PF_6^-, 1. KO^{t}Bu (1 M in THF, 3.5 equiv.), –78 °C, 30 min, 2. $FeBr_2$ (0.7 equiv. in THF) –78 °C to r.t., 16 h. ii) R = Ph, X = PF_6^-, 1. DMF, $FeBr_2$ (0.7 equiv.), 0 °C, 2. KO^{t}Bu (1 M in THF, 3.5 equiv.), 0 °C to r.t., 2 h iii) R = H, X = Br^-, 1. KO^{t}Bu (1 M in THF, 3.5 equiv.), –78 °C, 30 min, 2. $FeBr_2$ (0.7 equiv. in THF) –78 °C to r.t., 16 h.

Subsequently, the formation of the silver carbene and transmetallation to iron was attempted. Both the H- and Ph-substituted ligands cleanly formed the corresponding silver carbene when reacted with Ag_2O under reflux conditions in DCM. The carbene formation could be seen on crude ^{1}H NMR by the disappearance of the acidic proton of the benzimidazole. The silver carbene also formed in acetonitrile, although the reaction did not go to completion. The subsequent transmetallation to iron was attempted both with $FeBr_2$ and $FeBr_3$, but to no avail (Scheme 7).

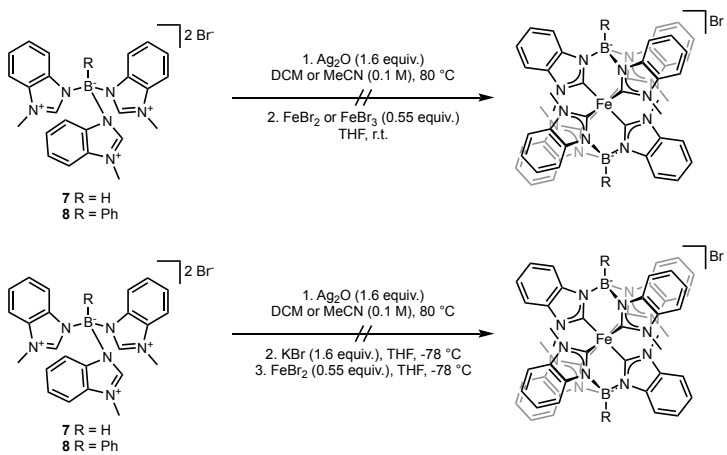

Scheme 7. Attempted synthesis of $[Fe(HB(Bim)_3)_2]Br$ and $[Fe(PhB(Bim)_3)_2]Br$ by formation of the silver carbene and subsequent transmetallation to $FeBr_2$ and $FeBr_3$.

The silver carbene method was taken further, and inspired by works in the group of Smith[64], potassium bromide was introduced either prior to, or together with $FeBr_2$, to

form the uncoordinated carbene, which would subsequently coordinate to iron. However, this approach did also not yield the desired product.

Alternatively, following a procedure by Liu *et al.*, another complexation method using iron powder (Fe^0) was attempted (Scheme 8).[115] This method was also unsuccessful, likely due to the necessity of ligand pre-association with the metal. In the study by Liu *et al.*, the ligand featured two pyridine groups capable of binding to the metal before the carbene.

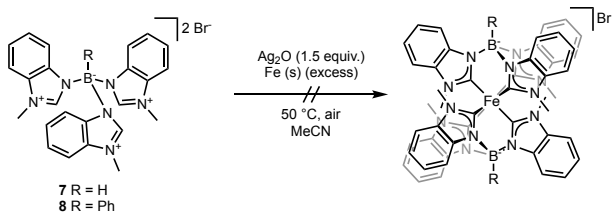

Scheme 8. Attempted synthesis of $[Fe(HB(Bim)_3)_2]Br$ and $[Fe(HB(Bim)_3)_2]Br$ by formation of the silver carbene and in situ transmetallation to Fe^0.[115]

Finally, reaction of the ligands with $[Zr^{IV}(Me_2N)_4]$ and transmetallation to $FeBr_2$ or $FeBr_3$ proved equally unsuccessful (Scheme 9).

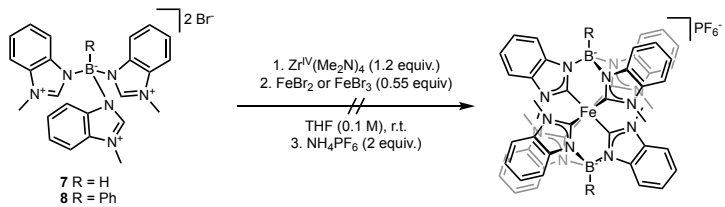

Scheme 9. Attempted synthesis of $[Fe(HB(Bim)_3)_2]Br$ and $[Fe(PhB(Bim)_3)_2]Br$ using $[Zr^{IV}(Me_2N)_4]$ and transmetallation to $FeBr_2$ and $FeBr_3$.

As a control reaction, the formation of $[Fe(phtmeimb)_2]Br$ from the corresponding silver carbene was investigated. This was indeed feasible using Ag_2O in DCM, followed by KBr and $FeBr_2$ in THF at -78 °C (Scheme 10).

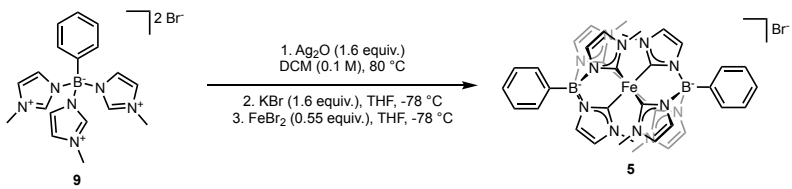

Scheme 10. Synthesis of $[Fe(phtmeimb)_2]Br$ via transmetallation from the silver carbene.

The reasons for the failed complexations of $[PhB(Bim)_3]^{2+}$ and $[HB(Bim)_3]^{2+}$ with iron could be manifold. One hypothesis is that after coordination of one carbene to the iron, the rotation around the B–N bond becomes restricted due to steric reasons. This means that unless all three carbenes point in the right direction from the beginning, the coordination of all three is not possible. The probability of the carbenes all pointing towards each other is likely to be low.

2.2 $[Fe^{III}(PhB(ImPy)_3)_2]PF_6$ and $[Fe^{II}(PhB(ImPy)_3)_2]$

In the light of the unsuccessful complexations of the benzimidazole substituted ligand, a step back to the drawing board was necessary. An alternative ligand, which should have similar extended π-orbitals is the ligand tris(imidazo[1,5-*a*]pyridin-4-ium-2-yl)(phenyl)borate ($[PhB(ImPy)_3]^{2+}$, **10**, Scheme 11). Replacing the benzimidazoles with imidazo[1,5-*a*]pyridines[116] was anticipated to facilitate rotation around the B–N bond, potentially allowing successful complexation of the ligand to iron.

2.2.1 Synthesis

The two ligands $[PhB(ImPy)_3]^{2+}$ (**10**) and $[HB(ImPy)_3]^{2+}$ (**11**) were synthesised in excellent yields according to the same procedures as the benzimidazole versions (Scheme 11).

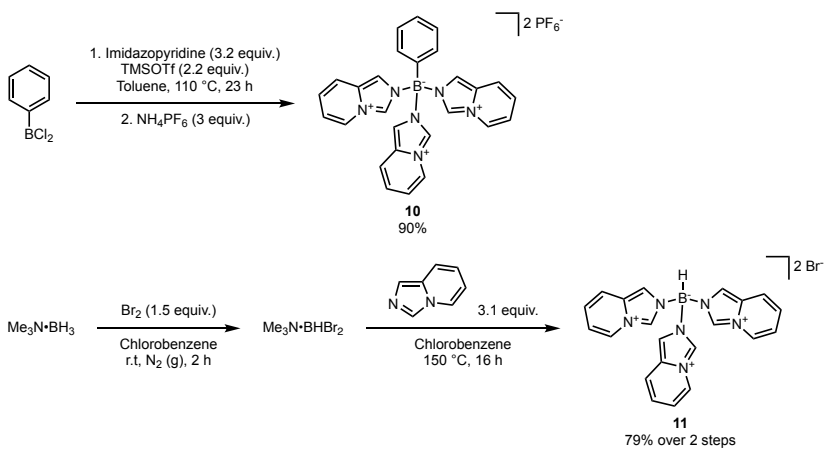

Scheme 11. Synthesis of $[PhB(ImPy)_3](PF_6)_2$ ((tris(imidazo[1,5-*a*]pyridin-4-ium-2-yl)(phenyl)borate bis(hexafluorophosphate)) and $[HB(ImPy)_3](PF_6)_2$ ((tris(imidazo[1,5-*a*]pyridin-4-ium-2-yl)(hydrido)borate dibromide) pre-ligands.

After some optimisation, conditions for the synthesis of $[Fe^{III}(PhB(ImPy)_3)_2]PF_6$ were found. As for $[Fe^{III}(phtmeimb)_2]PF_6$, the synthesis could either be performed via the silver carbene and transmetallation with added KBr, or by direct deprotonation with potassium *tert*-butoxide (Scheme 12). The route via direct deprotonation was chosen as it required fewer reaction components as well as fewer steps.

One noteworthy difference compared to the synthesis of $[Fe(phtmeimb)_2]PF_6$ was the instant colour change of the ligand upon deprotonation with potassium *tert*-butoxide. Furthermore, the best yields were obtained when the solution of $FeBr_2$ was added immediately after the addition of base. All in all, this points to **10** being more acidic than the phtmeimb pre-ligand.

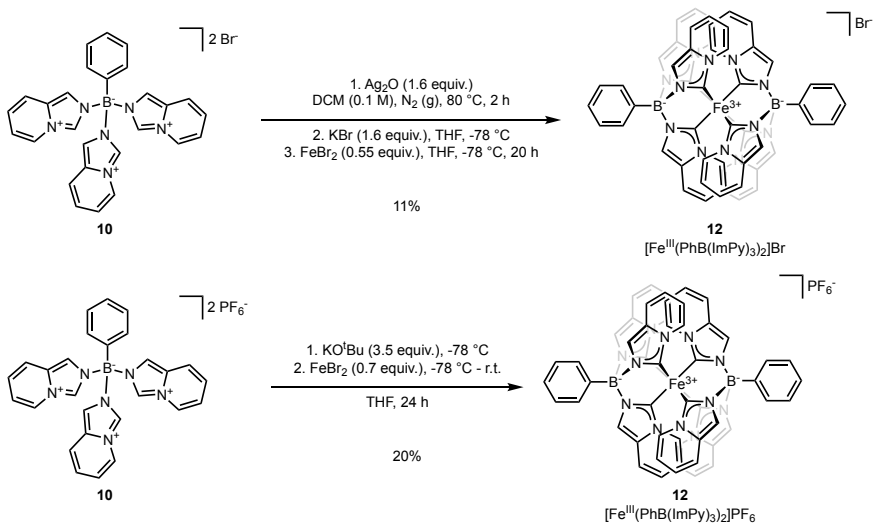

Scheme 12. Synthesis of $[Fe^{III}(PhB(ImPy)_3)_2]Br$ and $[Fe^{III}(PhB(ImPy)_3)_2]PF_6$ via the silver carbene and direct deprotonation, respectively.

As the aim of this project was to also study the influence of the extended π-system on the MLCT states of the Fe^{II} complex, a reduction of the complex was necessary. This could be achieved by reduction with lithium aluminium hydride ($LiAlH_4$) in THF (Scheme 13), which gave rise to inversion of the colour from green (Fe^{III}) to red (Fe^{II}). The obtained $[Fe^{II}(PhB(ImPy)_3)_2]$ was prone to oxidation, in particular in solution, and therefore extremely sensitive to any traces of oxygen. NMR spectra from samples prepared under inert conditions allowed characterisation of the complex. Furthermore, single crystals suitable for X-ray diffraction analysis could be grown under nitrogen atmosphere by slow vapour diffusion of toluene into a THF solution.

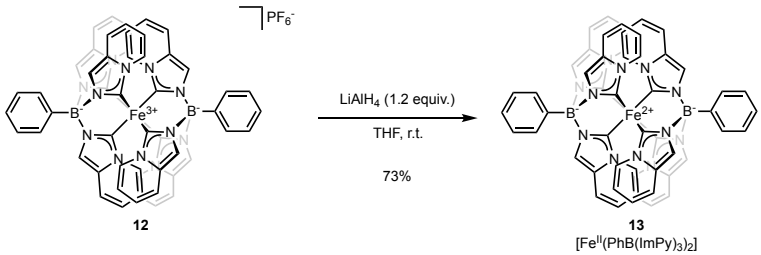

Scheme 13. Reduction of $[Fe^{III}(PhB(ImPy)_3)_2]PF_6$ to $[Fe^{II}(PhB(ImPy)_3)_2]$ by $LiAlH_4$ in THF.

2.2.2 Magnetisation, Mößbauer and EPR studies

The spin state of $[Fe^{III}(PhB(ImPy)_3)_2]PF_6$ was determined both in solution and in the solid state. Evans' NMR method gave a magnetic susceptibility in acetonitrile solution of 2.09 ± 0.005 Bohr magnetons (μ_B), in line with what is expected for a low spin Fe^{III} complex. This was corroborated by solid state direct current magnetization measurements consistent with a S = ½ spin system. Curiously, ^{57}Fe Mößbauer measurements displayed a two-line pattern with splitting of the peaks. This can be explained by the crystal structure of $[Fe^{III}(PhB(ImPy)_3)_2]PF_6$, where two different conformers of the complex co-crystallise in an asymmetric unit cell. The two conformers have markedly different sizes of the ligand cages surrounding the Fe^{3+}, thereby giving rise to the two-line pattern in the Mößbauer spectrum. EPR measurements of $[Fe^{III}(PhB(ImPy)_3)_2]PF_6$ resulted in very broad signals, which is explained by the high octahedricity, in line with other similar iron complexes.[38]

2.2.3 Photophysics of $[Fe^{III}(PhB(ImPy)_3)_2]^+$

The photophysics of $[Fe^{III}(PhB(ImPy)_3)_2]^+$ were studied using steady-state and transient absorption spectroscopy, as well as by DFT calculations. $[Fe^{III}(PhB(ImPy)_3)_2]^+$ shows a broad near-IR absorption peaking at 710 nm and 780 nm (Fig. 19). The absorption has both a higher extinction coefficient (ε = 7.10 and 7.41 × 10^3 M^{-1} cm^{-1}) and is significantly red-shifted compared to the parent complex $[Fe(phtmeimb)_2]^+$, reflecting the raised π-orbital due to increased conjugation on the ligand. This red-shift is in agreement with the DFT calculations (Fig. 20). The absorption band is assigned as a LMCT transition, which is supported by the spectroelectrochemistry and DFT calculations. Excitation into this band gives rise to fluorescence (λ_{em} = 870 nm), with an excitation spectrum that matches the LMCT band very well (Fig. 19). Calculations assign this to a transition from the π-orbitals on the imidazopyridines to the metal, in line with what is seen in $[Fe(phtmeimb)_2]^+$ (Fig. 20).

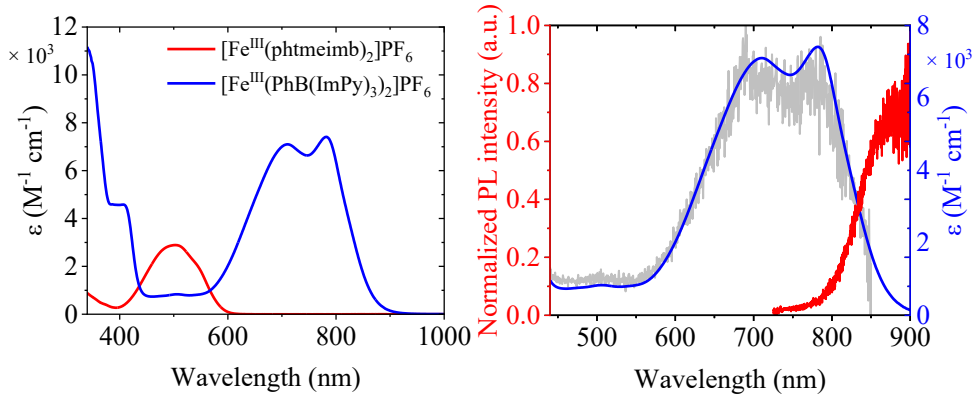

Figure 19. UV-Vis-NIR absorption spectra of $[Fe^{III}(PhB(ImPy)_3)_2]PF_6$ and $[Fe^{III}(phtmeimb)_2]PF_6$ in acetonitrile (left), emission spectrum (red, λ_{ex} = 708 nm) and excitation spectra (gray, λ_{em} = 870 nm) of $[Fe^{III}(PhB(ImPy)_3)_2]PF_6$ in acetonitrile (right).

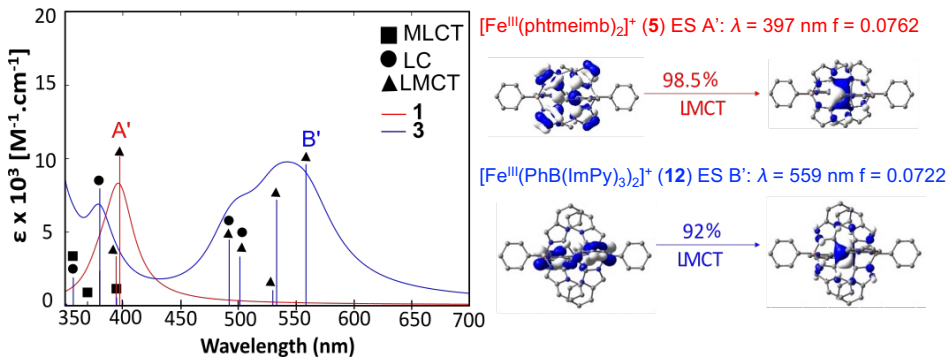

Figure 20. Calculated UV-Vis spectra of $[Fe^{III}(phtmeimb)_2]^+$ (**5**) and $[Fe^{III}(PhB(ImPy)_3)_2]^+$ (**12**).

Cyclic voltammetry of the complex revealed two reversible one-electron waves, corresponding to the reduction and oxidation to $[Fe^{II}(PhB(ImPy)_3)_2]$ and $[Fe^{IV}(PhB(ImPy)_3)_2]^{2+}$ respectively. By combining this data with the estimated E_{0-0} from the absorption and emission spectroscopy, we can use the Rehm–Weller equations (eq. 20 and 21) to estimate the excited state oxidation and reduction potentials. From this, we can construct the following Latimer diagram (Fig. 21).

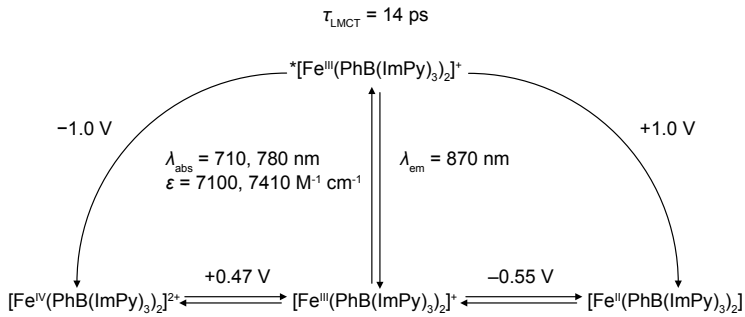

Figure 21. Latimer diagram displaying key electrochemical and photophysical properties of [Fe^{III}(PhB(ImPy)$_3$)$_2$]$^+$. All potentials are given vs SCE. They were originally measured vs Fc$^{+/0}$ in acetonitrile and converted using a conversion constant of +0.38 V.[58]

The lifetime of the ^{2}LMCT state could be determined by transient absorption spectroscopy to be 14 ps. The nature of the excited state could be corroborated by spectroelectrochemistry, from which spectra for the Fe^{II}, Fe^{III} and Fe^{IV} complexes as well as for the Fe^{IV} complex irreversibly oxidised at the ligand could be obtained. The reason for this relatively short excited state lifetime is not entirely clear. DFT calculations indicate that the barrier for deactivation ^{2}LMCT → ^{4}MC was increased from 0.04 eV to 0.16 eV when comparing [Fe^{III}(phtmeimb)$_2$]$^+$ and [Fe^{III}(PhB(ImPy)$_3$)$_2$]$^+$, due to the lowered energy of the ^{2}LMCT state of the latter. The main deactivation pathway may however be the spin-allowed direct nonradiative decay ^{2}LMCT → ^{2}GS, as for *[Fe(phtmeimb)$_2$]$^+$.

2.2.4 Photophysics of [Fe^{II}(PhB(ImPy)$_3$)$_2$]

The UV-vis absorption spectrum of [Fe^{II}(PhB(ImPy)$_3$)$_2$] (λ_{abs} = 516 nm, ε = 6.2 × 10^3 M^{-1} cm^{-1}) is also significantly red-shifted compared to [Fe^{II}(phtmeimb)$_2$], and resembles more the absorption spectrum of [Fe^{III}(phtmeimb)$_2$]$^+$ (Fig. 22). Computational analysis supports the assignment of the main absorption band at to an MLCT transition (Fig. 23). Notably, DFT calculations suggest that this band arises from a π^*_{NHC} ← t_{2g} transition, whereas for [Fe^{II}(phtmeimb)$_2$] it corresponds to a π^*_{Ph} ← t_{2g} transition. This is consistent with the extended π-conjugation of the imidazo[1,5-*a*]pyridine, which is expected to lower the energy of the π*-orbital on the NHC-moiety.

Excitation of the MLCT band leads to a long-lived excited state with a lifetime of 120 ns. We suspect that this excited state is a ^{3}MC state, given that the excited-state lifetime is unusually long compared to what is typically observed for iron complexes. The lack of spectra of the ligand-reduced complex makes it impossible to compare the transient absorption spectrum of this excited state to a spectroelectrochemical difference spectrum, which would facilitate assignment of the excited state. Our hypothesis is that

the ^{3}MC state forms within the instrument response function (<150 fs) of the transient absorption spectroscopy setup. The ultrafast formation of the ^{3}MC state may be attributed to the stronger electronic coupling between the ^{3}MLCT and ^{3}MC states, promoted by the electron's location in the π^*_{NHC} orbital (closer to the metal) in the ^{3}MLCT state, rather than in the π^*_{Ph} (further away from the metal) as in $[Fe^{II}(phtmeimb)_2]$ (Fig. 23). This spatial proximity of the orbitals enhances the electronic coupling, which leads to fast IC between the states.

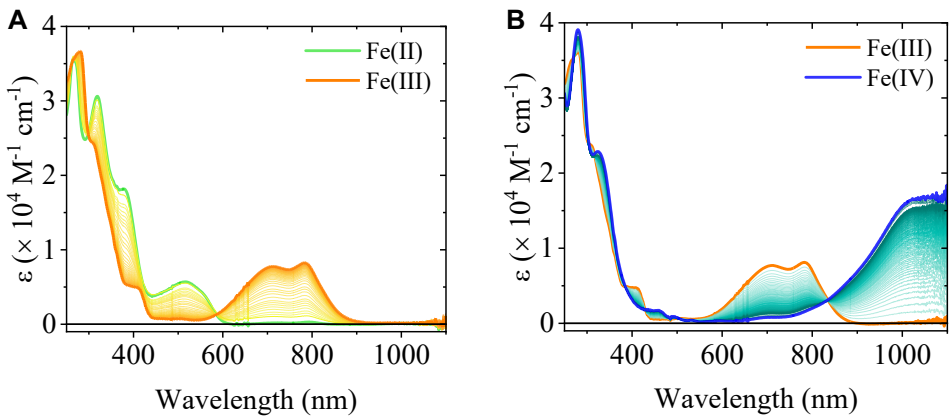

Figure 22. UV-Vis-NIR spectroelectrochemistry of $[Fe^{III}(PhB(ImPy)_3)_2]PF_6$ (orange line). (A) Reduction to $[Fe^{II}(PhB(ImPy)_3)_2]$ (green line) at −1.01 V vs SCE (B) Oxidation to $[Fe^{IV}(PhB(ImPy)_3)_2](PF_6)_2$ (blue line) at 0.99 V vs SCE

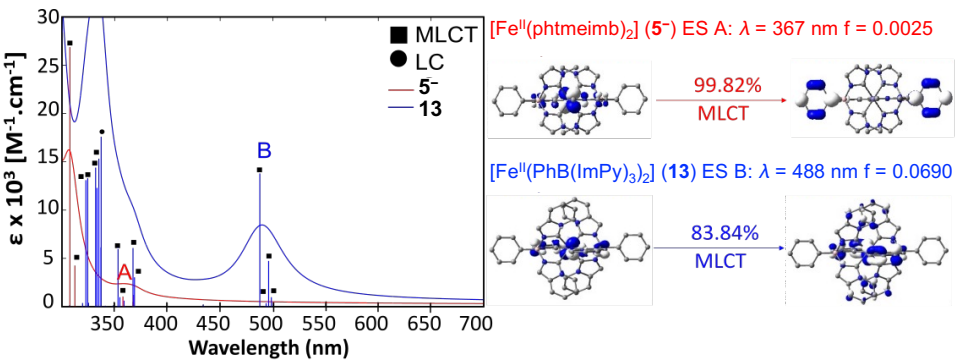

Figure 23. Calculated UV-Vis spectra of $[Fe^{II}(phtmeimb)_2]$ (**5**$^-$) and $[Fe^{II}(PhB(ImPy)_3)_2]$ (**13**).

2.3 Conclusion

Despite the investigation of several routes for the synthesis of $[Fe^{III}(PhB(Bim)_3)_2]^+$ and $[Fe^{III}(HB(Bim)_3)_2]^+$, their complexations were never successful. This could be due to steric hindrance to get the right reactive conformation of the ligand in the complexation step, hindering the association of all six carbenes.

Instead, a different benzannulated version of the ligand ($[PhB(ImPy)_3](PF_6)_2$) with an extended π-system was synthesized. The corresponding complex, $[Fe^{III}(PhB(ImPy)_3)_2]PF_6$, could be synthesized following two different methodologies, either by direct deprotonation of the ligand using potassium *tert*-butoxide, or via the silver carbene. The dark green complex had a stronger absorption than the parent complex $[Fe^{III}(phtmeimb)_2]^+$, and was characterised using a wide range of techniques. Reduction with $LiAlH_4$ resulted in the air-sensitive red Fe^{II} complex, $[Fe^{II}(PhB(ImPy)_3)_2]$, which could be characterised by NMR and single crystal X-ray diffraction.

The Fe^{III} complex, $[Fe^{III}(PhB(ImPy)_3)_2]^+$, had a significantly red-shifted LMCT band and emission compared to the parent complex, $[Fe^{III}(phtmeimb)_2]^+$. Despite the increased energy barrier for ISC from the ^{2}LMCT state to the ^{4}MC state, the ^{2}LMCT lifetime was shortened from 2.0 ns to 14 ps. This shortened excited state lifetime must come from faster nonradiative decay $^2\text{LMCT} \rightarrow {}^2\text{GS}$, possibly caused by a smaller energy gap between these states.

$[Fe^{II}(PhB(ImPy)_3)_2]$ displayed an absorption band at λ = 516 nm, and excitation into this band resulted in an excited state with a lifetime of 120 ns. While this is exceptionally long-lived excited state for an iron complex, we cannot at this point with certainty determine the nature of this state. A similarly long-lived MC state can be found in the iron complex $[Fe^{II}(tren(py)_3)]^{2+}$ ($tren(py)_3$ = tris(2-pyridyl-methylimino-ethyl)amine), which has a ^{5}MC state with a lifetime of 55 ns.[17] However, this long lifetime can be attributed to the quintet nature of the excited state. To find comparably long-lived ^{3}MC states, we need to look at complexes of other metals. For instance, d^6 $[Co^{III}(phtmeimb)_2]^+$ has a luminescent ^{3}MC state with a lifetime of 1 μs in solution.[117] Other examples of luminescent MC states are found in d^3 Cr^{III} complexes, where the lifetime is extended by the MC states being nested above the ground state.[118]

Although the extended lifetime makes $[Fe^{II}(PhB(ImPy)_3)_2]$ appealing for potential applications such as photoredox catalysis, the oxygen sensitivity of the Fe^{II} complex in solution presents a challenge. However, if $[Fe^{III}(PhB(ImPy)_3)_2]^+$ could be reduced in situ to $[Fe^{II}(PhB(ImPy)_3)_2]$, one could imagine using $*[Fe^{II}(PhB(ImPy)_3)_2]$ for photoredox catalysis under conditions where it is oxidized by a suitable electron acceptor. Given the recent developments using MC states in photoredox catalysis, this complex presents a promising avenue for further exploration.

3 A combined strategy of cyclometallation and *N*-heterocyclic carbenes (Paper II)

As outlined in the introduction, one strategy to improve the ^{3}MLCT and ^{2}LMCT lifetimes of iron complexes is to increase the ligand field splitting. Thereby MC states are raised in energy compared to the CT states, introducing an energy barrier for deexcitation through the MC states. A strong-field ligand that is both a good σ-donor and a π-acceptor is a cyclometallated benzene. Based on this knowledge, the tridentate ligand ImP (ImP = bis(2,6-bis(3-methylimidazol-2-ylidene-1-yl)phenylene), containing one cyclometallated phenyl-ring and two *N*-heterocyclic carbene moieties, was proposed to give beneficial photophysical properties (Scheme 14). Complexation with iron yielded the complex $[Fe^{III}(ImP)_2]PF_6$ (**15**). This complex had already been synthesised by Hollis and Webster[119], but at the onset of our investigations, the photophysical properties remained unknown. During our exploration of the complex, a preprint, and later a paper[52], by the group of Bauer, were published, which investigated the photophysical properties of $[Fe^{III}(ImP)_2]PF_6$. In their paper, they reported a high energy ^{2}MLCT band (λ = 351 nm, ε = 6000 M^{-1} cm^{-1}) and a significantly weaker ^{2}LMCT band (λ = 585 nm, ε = 540 M^{-1} cm^{-1}). Moreover, they reported luminescence from both these states ($\lambda_{em, MLCT}$ = 430 nm and $\lambda_{em, LMCT}$ = 735 nm).

As we had observed the feasibility of using Fe^{II} complexes in photoredox catalysis, we chose to also synthesise $[Fe^{II}(ImP)_2]$ and study its photophysical properties. We envisioned the synthesis of $[Fe^{II}(ImP)_2]$ by reduction of the corresponding Fe^{III} complex, $[Fe^{III}(ImP)_2]PF_6$. For this reason, it was first necessary to synthesise the Fe^{III} complex in pure form, to be used for the subsequent reduction. Reading the paper by the group of Bauer, we were puzzled by the reported dual luminescence of $[Fe^{III}(ImP)_2]PF_6$. Dual luminescence breaking Kasha's rule is a rare phenomenon, and only a handful cases exist.[120,121] Furthermore, the lack of corresponding long-lived features in the transient absorption data was perturbing. In the course of our investigation, we therefore decided to also re-examine the photophysical properties of $[Fe^{III}(ImP)_2]PF_6$.

3.1 Results and discussion

Our synthesis of $[Fe^{III}(ImP)_2]PF_6$ was based on that first described by Hollis and Webster[119], and later adapted by Bauer[52] (Scheme 14). Two different aspects of our synthesis might be worth noting: the synthesis was run in the dark, although light was allowed during setup and work up of the reaction, and the complex was purified using size exclusion chromatography (Biobeads SX-1). The reduction to $[Fe^{II}(ImP)_2]$ could be achieved by suspending the complex in dry THF and treating it with a slight excess of $LiAlH_4$ as the reducing agent. Most notable in the reduction was the drastic colour change from dark blue to bright orange.

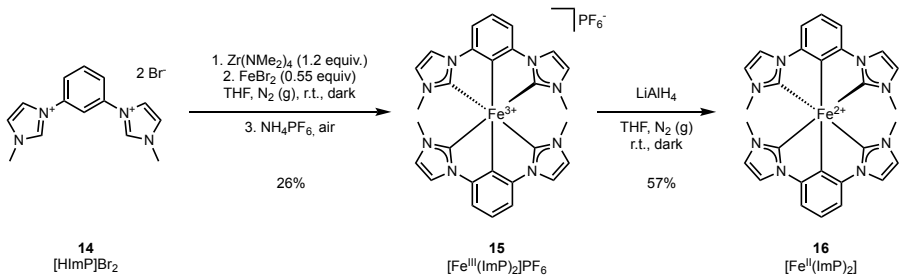

Scheme 14. Synthesis of $[Fe^{III}(ImP)_2]PF_6$ and $[Fe^{II}(ImP)_2]$. Scheme adapted from Paper II with permission from the Royal Society of Chemistry.

3.1.1 Photophysics of $[Fe^{III}(ImP)_2]^+$

The photophysical investigations reproduced much of what Bauer and co-workers had observed, including a broad ^{2}LMCT band between 450 nm and 650 nm (Fig. 24). The observed red emission, peaking at about 750 nm, was replicated by photoexcitation of $[Fe^{III}(ImP)_2]PF_6$ at 585 nm, with its excitation spectra closely matching the ground state absorption spectrum. The lifetime of the ^{2}LMCT state was likewise found to be 240 ps, virtually identical to the previously lifetime.

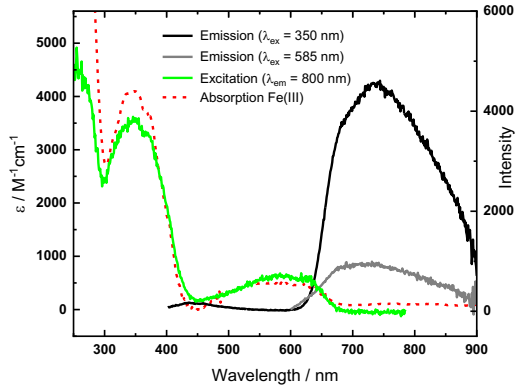

Figure 24. Absorption, emission and excitation spectra of $[Fe^{III}(ImP)_2]PF_6$ in acetonitrile at room temperature. Reproduced from Paper II with permission from the Royal Society of Chemistry.

The high energy ^{2}MLCT band at 350 nm could also be observed, however, excitation at this wavelength only produced a minimal blue emission. In addition, the emission intensity ratio was very different from what was reported previously. It was therefore concluded that the reported blue emission must arise from an impurity, rather than from the complex itself. Excitation at 350 nm led to the population of an excited state, denoted as ^{2}MLCT', which decayed with a lifetime of 0.5 ps to populate the ^{2}LMCT state as well as a relaxed MLCT state, denoted ^{2}MLCT. The lifetime of the ^{2}MLCT state was measured to be 9 ps (6 ps in the previous report). This lifetime clearly does not match with the reported lifetime of the blue emission (4.6 ns). We therefore suspected the blue emission to rather originate from a minor but strongly emissive impurity. All in all, the excited state landscape can be summarised as in figure 25.

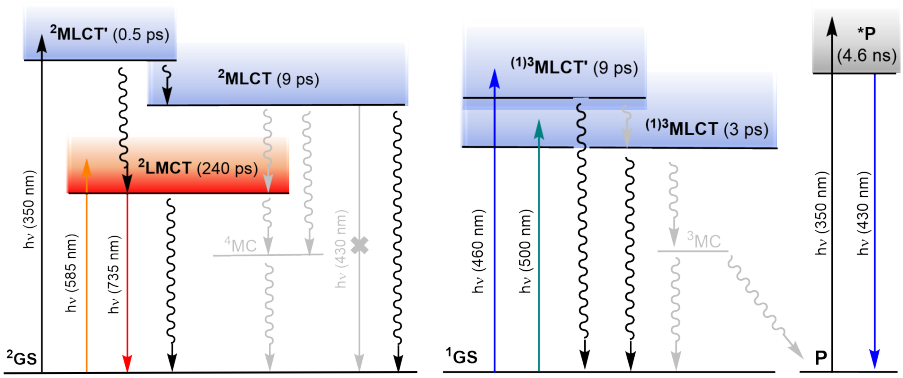

Figure 25. Schematic state energy diagram of $[Fe^{III}(ImP)_2]^+$ (left) and $[Fe^{II}(ImP)_2]$ (right). Reproduced from Paper II with permission from the Royal Society of Chemistry.

3.1.2 Photophysics of $[Fe^{II}(ImP)_2]$

UV-vis absorption spectroscopy of $[Fe^{II}(ImP)_2]$ showed two MLCT bands, one at 320 nm and one twice as intense at 400 nm (ε = 12 000 $M^{-1}cm^{-1}$, Fig. 26). No absorption above 550 nm was observed. The lowest energy MLCT band populates the LUMO and LUMO+1, whereas the higher energy band primarily populates the LUMO+3 and LUMO+4. Emission spectroscopy (λ_{ex} = 350 nm) in acetonitrile showed a weak, broad, red emission band corresponding to the emission of $[Fe^{III}(ImP)_2]^+$. As $[Fe^{II}(ImP)_2]$ is very prone to oxidation, any sample of $[Fe^{II}(ImP)_2]$ was inevitably contaminated by some $[Fe^{III}(ImP)_2]^+$. The minor emission originating from the oxidised $[Fe^{III}(ImP)_2]^+$ was confirmed by the excitation spectrum of the red emission, which matched the absorption spectrum of $[Fe^{III}(ImP)_2]^+$.

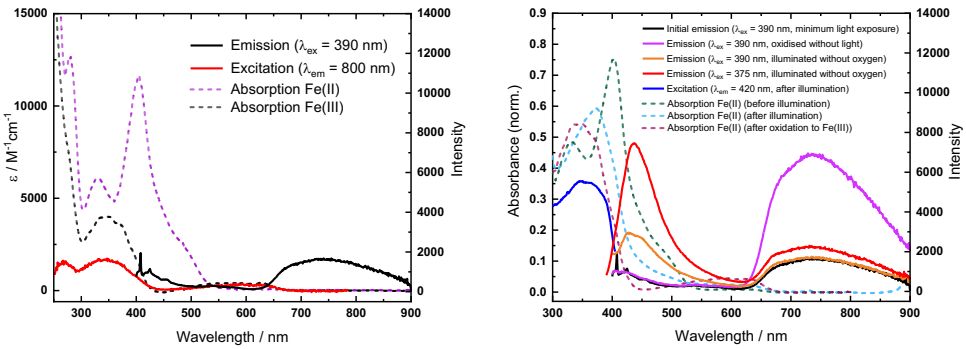

Figure 26. Left: Absorption, emission and excitation spectra of $[Fe^{II}(ImP)_2]$ in acetonitrile at room temperature. Right: Effects of light exposure and oxidation by atmospheric oxygen. Reproduced from Paper II with permission from the Royal Society of Chemistry.

Transient absorption spectroscopy (λ_{ex} = 450 nm) in acetonitrile revealed population of two different MLCT states, denoted ^{3}MLCT and ^{3}MLCT', within the instrument response function (<140 fs). The kinetics indicate that they to some extent form in parallel through intersystem crossing from a short-lived ^{1}MLCT state, but also that the some of the ^{3}MLCT state forms from the ^{3}MLCT' state. Their respective lifetimes obtained from global analysis are 2.7 and 9.1 ps respectively (Fig. 25).

To investigate the origin of the emissive impurity, several experiments as well as computations were performed. Photostability studies of $[Fe^{III}(ImP)_2]^+$ proved the complex to be rather stable in this oxidation state. However, photostability studies of the reduced $[Fe^{II}(ImP)_2]$ showed that the complex was stable under blue light irradiation (λ = 450 nm) in THF, but not under the same irradiation in acetonitrile (Fig. 27). Under irradiation in acetonitrile, a new absorption band (λ = 380 nm)

appeared, which does not correspond to oxidation to $[Fe^{III}(ImP)_2]^+$. Concomitant with the appearance of this new absorption band, the appearance of the blue emission (λ_{em} = 430 nm) was visible. The blue emission only appeared when $[Fe^{II}(ImP)_2]$ was irradiated, and dark conditions only showed slow oxidation to $[Fe^{III}(ImP)_2]^+$. It therefore seems likely that the blue emission originates from some sort of photoproduct of $[Fe^{II}(ImP)_2]$.

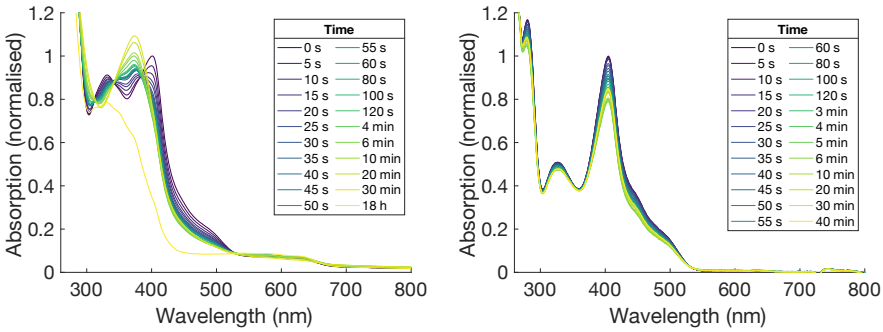

Figure 27. Photostability of $[Fe^{II}(ImP)_2]$ in acetonitrile (left) and THF (right) under N_2 (g), blue light irradiation (λ = 450 nm) at room temperature, monitored by UV-vis absorption spectroscopy. Reproduced from Paper II with permission from the Royal Society of Chemistry.

Computational calculations made plausible a ligand detachment in the ^{3}MC and ^{5}MC states, forming a five-coordinate complex. Upon this partial detachment, a solvent molecule of acetonitrile can coordinate to the metal. Contrarily to the expected coordination of the nitrogen to the iron centre, a van der Waals coordination into the formed pocket was found to be the most stable configuration.

The ligand precursor $(HImP)^{2+}$ was therefore studied by steady-state and transient absorption UV-vis absorption and emission spectroscopy. Its absorption (λ_{abs} = 365 nm) and emission (λ_{em} = 410 nm, τ = 4.6 ns) were similar to that of the blue emission previously observed for samples of $[Fe^{III}(ImP)_2]^+$. All in all, this pointed to that the blue emission originated from an impurity that formed by light absorption of $[Fe^{II}(ImP)_2]$. The impurity could arise through a pathway where the ligand detaches, first by one NHC moiety, and then possibly completely, to form an emissive ligand derivative.

3.2 Conclusion

$[Fe^{III}(ImP)_2]^+$ still has a remarkably long-lived ^{2}LMCT state (τ = 240 ps) with broad red emission. However, the blue, long-lived emission seems to originate from an emissive impurity, that originates from photodecomposition of $[Fe^{II}(ImP)_2]$. This points to the need for pure samples, as a very small impurity with a high emission

quantum yield can give false positive results. As examples of dual emission with metal complexes at room temperature are still extremely rare[120,121], cross checking emission lifetimes with transient absorption data is important to avoid false assignments of emission.

Nevertheless, an arylated derivative of $[Fe^{III}(ImP)_2]^+$ with similar excited state properties (λ_{abs} = 635 nm, τ_{LMCT} = 267 ps) has recently been shown by Wellauer *et al.* to engage in photoredox catalysis.[112] This is another example that complexes with rather short excited state lifetimes might still be useful in photoredox catalysis, as seen in later chapters.

4 Non-invasive monitoring of multiple gases using rotational Raman spectroscopy (Paper III)

Artificial photosynthesis reactions often produce gaseous reaction products, such as hydrogen and carbon monoxide, which require specialised analysis methods for identification and quantification. This chapter is somewhat an intermezzo in this thesis, as it describes a novel technique instead of a new complex or reaction. However, new technologies and scientific breakthroughs often go hand in hand, one enabling the other. The techniques most commonly used for quantification of gaseous products are gas chromatography (GC), mass spectrometry (MS), Clark electrodes, gas burettes and pressure sensors[122,123]. Methods where small optical sensors are introduced in the reaction vessel and the readout occurs from the outside have also been developed for oxygen detection.[124]

The most common analysis methods, GC and MS, require sampling with at gas tight syringe, which pierces the reaction vessel, leaving a hole behind where gas can escape. Furthermore, the sampling itself is cumbersome and analysis times are in the range of 5–10 minutes/sample. Clark electrodes enable real time monitoring of one gas per electrode, but they also require piercing of the reaction vessel. Pressure sensors and gas burettes have the disadvantage that they cannot discriminate between different gases. Hitherto, methods that can identify and quantify several gases at the same time without penetration of the reaction vessel are absent in the field of artificial photosynthesis.

Raman spectroscopy could present a solution to this. Incident light that hits a molecule is scattered in all directions. The main part of the light keeps the same wavelength and energy and is called Rayleigh scattering. However, a minor part of the photons change their energy, and give rise to a Raman spectrum. The photons can either lose energy (Stokes part) or gain energy (anti-Stokes part) from the molecule. In rotational Raman spectroscopy, the energy difference between the incident light and the scattered photons depends on the rotational energy levels of the molecule. For a molecule to have a rotational Raman spectrum, the polarizability of the molecule must be anisotropic, i.e. it must depend on the orientation of the molecule. This is why all linear molecules have rotational Raman spectra, even linear symmetric molecules that are not IR active.

It also means that spherical molecules such as methane and SF_6 are rotational Raman silent, which is also the case for noble gases such as argon.

4.1 A new Raman-based gas analyser

In this project, we developed a Raman based gas analyser[125,126] and the associated software. We also showcased the utility of the instrument by doing real time simultaneous quantification of hydrogen and oxygen in a benchmark hydrogen evolution reaction. This enabled us to prove that the onset of hydrogen evolution depended on the concentration of oxygen in the reaction.

Rotational Raman spectra have previously not been used to any large extent for this purpose, as the intensity of Raman scattering is less than one millionth of the incident light.[127] This means that for quantitative purposes, strong lasers and very sensitive detectors are needed. However, if these limitations can be overcome, almost all of the gases of interest in artificial photosynthesis are Raman active (H_2, O_2, N_2, CO_2, CO). The intensity of the Raman signal is also directly proportional to the gas content at ambient pressures, making calibration uncomplicated. Furthermore, the Raman lines of hydrogen are clearly separated from the other gases, making analysis of hydrogen particularly straightforward. Also the other gases (O_2, N_2, CO_2, CO), which have overlapping Raman spectra, can be quantified simultaneously, since they all possess a unique spectrum, and the distance between the Raman lines, as well as their intensity, depends on the gas (Fig. 28).[128]

The Raman based gas analyser uses a backscattering geometry, which simplifies the optical layout. Laser light travels from a source (532 nm, 200 mW) and is directed onto the sample. The same lens can be used to focus the light on the sample as well as to collimate the Raman scattering (L1 in Fig. 29). As the Rayleigh scattering is 10^6 to 10^{12} times stronger than the Raman scattering,[129] a long pass filter (Semrock 532 nm RazorEdge® ultra-steep) is used to remove the Rayleigh scattering. The light is then guided onto a CCD array (Andor iDus 401, 1024 × 127 pixels) and the analysis is done with a custom-made software.

This enables sampling of the headspace of regular 4.9 mL clear glass vials, with each measurement taking 15–25 seconds. Before measurements, a two-point calibration would be made, with one measurement of a pure sample of the analyte gas, and one measurement of an argon filled vial. The reference spectrum of an argon filled vial compensates for the presence of air in the spectrometer. Prior to gas evolution reactions, the reaction vial is purged with Raman silent argon gas.

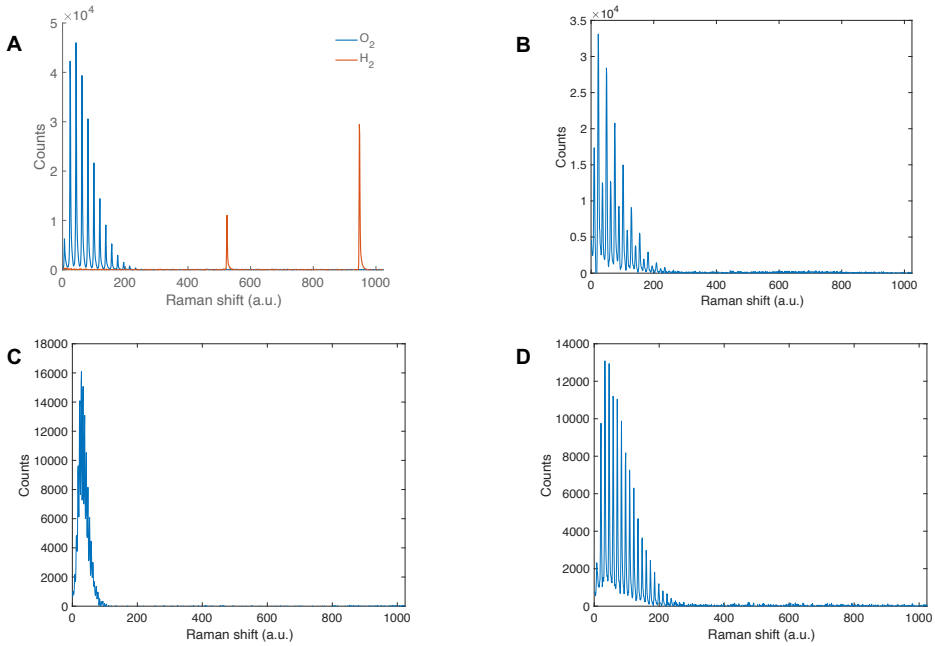

Figure 28. Rotational Raman spectrum of (A) Oxygen and hydrogen (B) Nitrogen (C) Carbon dioxide and (D) Carbon monoxide. Reproduced from Paper III with permission from the Royal Society of Chemistry.

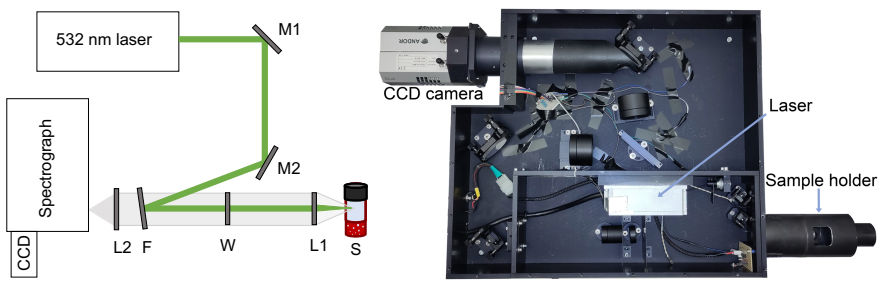

Figure 29. Left: Technical drawing of the Raman-based gas analyser. M = mirror, L = Lens, F = Edge filter, W = CaF_2 window, S = Sample. Right: Photo from above of the Raman gas analyser with the top cover removed. Reproduced from Paper III with permission from the Royal Society of Chemistry.

The sample setup has the benefit that many reactions can be run in parallel in small reaction volumes, minimising the amounts of precious catalysts and other reagents used, as well as enabling high throughput. This was particularly helpful in the development of an iron photosensitised hydrogen evolution reaction (see next chapter), where the optimisation was limited only by the number of reactions that could be run in parallel in the photoreactor (nine). Furthermore, since the green laser samples the

gas content in the headspace through the clear glass vial, the reaction can be sealed to avoid any leakage in or out from the vial. The green laser hits the vial from the side, which means that the reaction can be illuminated from below by a second light source. Thereby, the gas contents of the headspace can be measured in real time during the reaction, enabling kinetic plots to be made.

To establish the accuracy and precision of the Raman based gas analyser, calibration curves were made for the different gases. The calibration curves for hydrogen and oxygen were made in parallel with commercial Clark electrodes (Unisense), which enabled the direct comparison between the two methods. The calibration curves for hydrogen demonstrated exceptional precision, with R^2 = 0.998 up to 35000 µM and R^2 > 0.999 for concentrations between 40 and 5000 µM hydrogen in argon. In comparison to the Clark electrodes, measurements were accurate to within 3.5%. Also for oxygen, the calibration curves (0–8000 µM, R^2 = 0.9994) matched the Clark electrodes. For gas mixtures with overlapping Raman spectra, such as carbon monoxide in carbon dioxide and oxygen in nitrogen, calibration curves were recorded which showed that the differentiation of the gases is possible. A limitation with the analysis of reactions where large amounts of gases were produced was that at total pressures above 2 bar, some gas leaked through the septum of the vial.

It is well-known that oxygen has a detrimental effect on hydrogen formation reactions, in particular through the formation of reactive oxygen species (ROS).[130–132] These can be formed via energy transfer from the long-lived ^{3}MLCT state of a PS to oxygen, forming reactive singlet oxygen. The consumption of oxygen in parallel with hydrogen formation is however not well studied, and we thought this would be a perfect use for the Raman based gas analyser, as it can track several gases simultaneously and in real time.

We chose to study an established system consisting of a PS: $[Ir^{III}(dF(CF_3)ppy)_2(dtbbpy)]PF_6$ (0.03 mM), a proton reduction catalyst: $[Co^{II}(qpy)(OH_2)_2]ClO_4$ (qpy = 2,2':6',2'':6'',2'''-quaterpyridine) (0.6 mM), a sacrificial reductant: triethanolamine (TEOA) (0.2 M) and water (5% v/v) in acetonitrile (2 mL).[133] Before irradiation of the solution, it was purged with argon. The reactions were carried out in 4.9 mL glass vials with screw cap septum lids (silicone/PTFE) using UV LED irradiation (λ = 375 nm, 45 mW) from below the vials. Additionally, we tested green and blue LED irradiation (λ = 525 nm and 450 nm), but saw no effect on the data, signifying that light sources below the sample do not interfere with the gas analysis. To the reactions, different amounts of oxygen were added with a gas tight syringe before the irradiation was started. The oxygen decrease was monitored in parallel with the hydrogen increase, and we could observe that the onset of the hydrogen formation was delayed and did not start until the oxygen content had fallen to very low levels (<300 µM in the gas phase). We could also fit the oxygen decrease to a monoexponential decay and get very similar rate constants (k = 1.84–2.54 × 10^{-4} s^{-1})

for the consumption of oxygen independent of the starting concentrations of oxygen (Fig. 30). The decay of the oxygen levels can be explained in two fashions; either by the formation of reactive oxygen species as discussed above, or by reduction to water and hydrogen peroxide.[134–136]

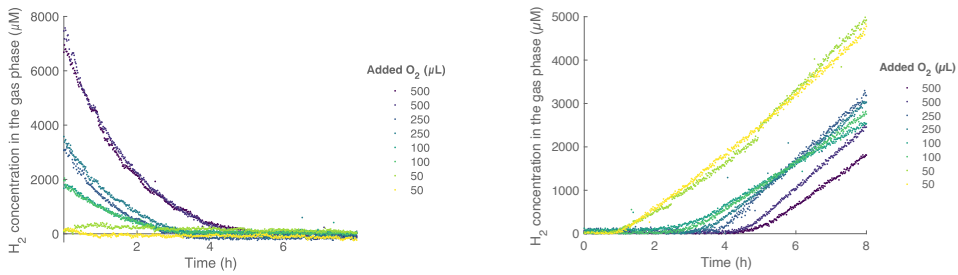

Figure 30. Simultaneous measurement of oxygen (left) and hydrogen (right) in a hydrogen formation reaction, under argon with different added amounts of oxygen initially. Experimental conditions: $[Ir^{III}(dF(CF_3)ppy)_2(dtbbpy)]PF_6$ (0.03 mM), $[Co^{II}(qpy)(OH_2)_2]ClO_4$ (0.6 mM), TEOA (0.2 M) and water (5% v/v) in acetonitrile (2 mL), headspace volume 2.9 mL. Reproduced from Paper III with permission from the Royal Society of Chemistry.

4.2 Conclusion

Even though the field of artificial photosynthesis and other gas evolving reactions are thriving, the Raman based gas analyser presented in this chapter has not been adopted by a larger audience yet. It is still produced on demand by a research group at the University of Jyväskylä, and not marketed by any company. A large part of the work in this project was the development of the analysis software together with the research group at the University of Jyväskylä, to make the software more stable and account for fluctuations in laser intensity. The gas analyser presented here has since then been further improved with a heated sample holder, to avoid problems with condensation droplets from aqueous solvents.[137] One could also imagine the use of this setup in conjunction with other in situ techniques, such as IR, to get deeper understanding of the mechanisms operating in gas forming reactions.

5 Artificial photosynthesis reactions driven by an Fe-NHC complex (Paper IV)

To decrease carbon dioxide emissions, a significant increase in renewable energy production is needed. The most promising renewable energy source is the sun. It supplies the earth with an average of 100 000 TW, which is enough energy in an hour to supply the worlds energy demand for the whole year.[138] This energy can be converted to electricity or stored in the form of solar-fuels, such as hydrogen or methanol. Hydrogen gas is already today used as a reagent in the chemical industry, as well as a fuel in niche applications. The demand is however set to increase as, for instance, the iron and steel industry are decarbonising.[139,140] Today, 96% of all hydrogen is still made from fossil gas through steam reforming and the water-gas shift reaction.[141] The current transition to green hydrogen is based on electrolysing water into its components hydrogen and oxygen, which would require enormous amounts of electricity, entering into direct competition with other electricity demands.[142] In fact, the amount of electricity needed to produce all of the current yearly hydrogen output from electricity would be 3,600 TWh, more than the annual electricity production of the European Union.[143]

5.1 Hydrogen evolution reactions

An alternative solution — which was pioneered by seminal work of Lehn and Sauvage,[79] Whitten,[144] and Grätzel[145–147] in the late 1970s — is the direct reduction of water by photoredox catalysis, nowadays part of what is called artificial photosynthesis.[148,149] The early examples used $[Ru(bpy)_3]^{2+}$ as a photosensitiser, which in conjunction with a proton reduction catalyst and a sacrificial reductant reduces protons to hydrogen gas. Since then, also other photosensitisers have been applied, such as Pt-terpyridine complexes,[150,151] Re-phenanthroline complexes,[152] Zn-porphyrins,[153] Cu complexes,[154,155] polymeric carbon nitride,[156] and Eosin Y[157]. Even though the later ones are based on earth-abundant elements, such examples are still rare. Furthermore, many

of these photosensitisers suffer from poor photostability, resulting in short-lived systems. The group of Bauer in 2017 published an example of light driven hydrogen formation using an iron photosensitiser (Scheme 15).[158] Later, they merged a cobaloxime proton reduction catalyst with the iron complex into a dyad.[159] Unfortunately, both systems suffered from low turnover numbers (TON = 5).

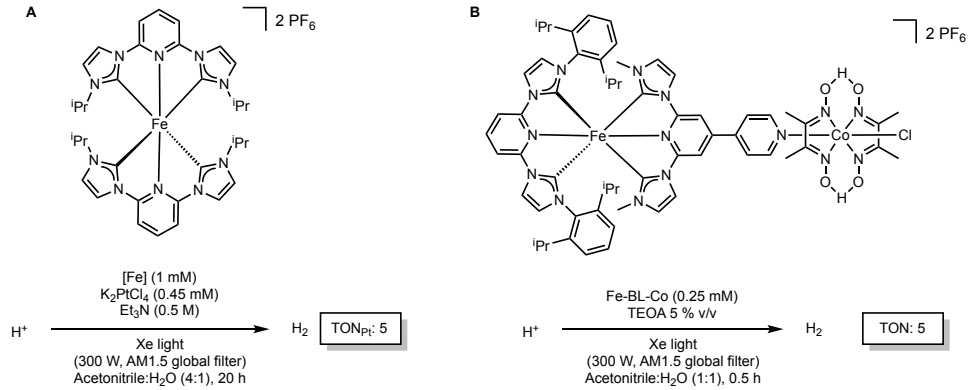

Scheme 15. Hydrogen formation reactions developed by the group of Bauer based on an iron NHC complex and Pt-colloids (A) and an iron-cobalt dyad (B). ^{i}Pr = 2-propyl.

5.1.1 Results and discussion

The excited state of $[Fe^{III}(phtmeimb)_2]^+$ is a very strong reductant ($E°(Fe^{IV/*III}) = -1.5$ V vs SCE), which should be able to reduce common proton reduction catalysts.[38] $*[Fe^{III}(phtmeimb)_2]^+$ is also a strong oxidant ($E°(Fe^{*III/II}) = +1.4$ V vs SCE), and the reduced $[Fe^{II}(phtmeimb)_2]$ is still a good reductant ($E_{1/2}(Fe^{III/II}) = -0.78$ V vs SCE). This opens the possibility of using amine-based reductive quenchers, such as triethanolamine (TEOA, $E_{1/2} = +0.82$ V[145] vs SCE) and triethylamine (Et_3N, $E_{1/2} = 0.94$ V[160] vs SCE), to quench the ^{2}LMCT $*Fe^{III}$. The obtained ground state $[Fe^{II}(phtmeimb)_2]$ would then be reducing enough to reduce the proton reduction catalyst.

Initial optimisation of the reaction conditions for hydrogen formation was based on Pt-colloids, generated by in situ reduction of K_2PtCl_4, and commonly used as proton reduction catalysts.[79] A concentration of 1 mM was chosen for the PS $[Fe(phtmeimb)_2]PF_6$ to ensure complete absorption of the light. The wavelength of λ = 530 nm is close to the local absorption maximum of $[Fe(phtmeimb)_2]^+$, and green light irradiation therefore directly excites the PS into the reactive ^{2}LMCT state. A standard sacrificial reductant triethylamine (Et_3N) was used since it has previously been shown to quench the PS effectively.[47] Table 1 displays selected results from the optimisation of the hydrogen evolution reaction catalysed by Pt-colloids. In addition to the

parameters varied in table 1, also the solvent, PS, proton source and concentrations were optimised. Different organic acids as well as water were investigated as proton sources, with $[HNEt_3][BF_4]$ performing the best. The system was most effective at a concentration of 0.05 mM of the K_2PtCl_4 precursor, as higher concentrations caused the Pt-catalyst to precipitate out of solution. Under the optimised circumstances, the formation of hydrogen occurred at a rate of around 6.5 mmol h^{-1}, which corresponds to a formal turnover frequency (TOF) of almost 130 h^{-1} with respect to the initial concentration of K_2PtCl_4. Over 22 hours, hydrogen generation continued at a relatively constant pace and produced 120 µmol of hydrogen, corresponding to a formal TON of 1176. (Table 1, entry 3). The TON with respect to the iron PS (TON_{Fe}) was 58.8, and the initial TOF_{Fe} was 3.23 h^{-1}.

Table 1. Hydrogen formation using $[Fe(phtmeimb)_2]PF_6$ as PS in conjunction with Pt-colloids as proton reduction catalyst.

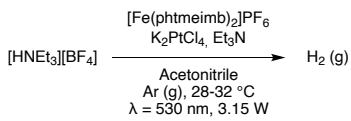

Entry	[PRC] (mM)	Time (h)	H_2 (µmol)	TON_{Pt}[a]	Initial TOF_{Pt} (h^{-1})	TON_{Fe}	Initial TOF_{Fe} (h^{-1})
1[b]	0.45	21	48.0	53.3		24.0	
2	0.9	21	5.79	3.22		2.90	
3	0.05	22	117.6	1176	129	58.8	3.23
4	0.01	20	12.2	612	68	6.10	0.34
5[b]	0.005	17	7.12	712		3.56	

Reaction conditions: $[Fe(phtmeimb)_2]PF_6$ (1 mM), K_2PtCl_4 (see column 2), $[HNEt_3][BF_4]$ (165 mM) and Et_3N (0.500 M) in acetonitrile (total volume 2 mL) in a 4.9 mL clear glass vial. The amount of hydrogen in the headspace was measured at regular time intervals by Raman spectroscopy. [a]TON = mol of hydrogen / mol of K_2PtCl_4. [b]average of 2 replicates. Adapted from Paper IV with permission from the Royal Society of Chemistry.

In an attempt to move to a fully earth-abundant system, the literature was screened for proton reduction catalysts with suitable reduction potentials. Two different cobaloximes with reduction potentials compatible with $[Fe(phtmeimb)_2]^+$ were found: $[Co(dmgBF_2)_2(H_2O)_2]$ ($E°(Co^{II/I})$ = –0.55[161] V vs SCE) and $[Co(dmgH)_2(py)Cl]$ ($E°(Co^{II/I})$ = –1.1[162] to –0.94[157] V vs SCE) (Fig. 31).[152,163–165] Only $[Co(dmgH)_2(py)Cl]$ proved to be effective; $[Co(dmgBF_2)_2(H_2O)_2]$ produced no more than 2 µmol of hydrogen (Table 2, entry 5), comparable to using no proton reduction catalyst at all (Table 2, entry 6).

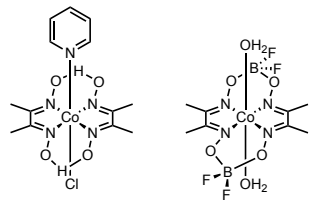

17 [Co(dmgH)$_2$(py)Cl] **18** [Co(dmgBF$_2$)$_2$(H$_2$O)$_2$]

Figure 31. Proton reduction catalysts used for hydrogen evolution reactions.[163,165]

With the [Co(dmgH)$_2$(py)Cl] proton reduction catalyst, however, very similar rates of hydrogen production (6.5 μmol h^{-1}) compared to Pt-colloids could be seen (Table 2). However, stabilising the complex by adding free ligand (dimethylglyoxime = dmgH$_2$) was necessary for maintaining hydrogen production (Table 2, entries 1 and 2). A ligand concentration of 3 mM produced the best results, at this concentration, the hydrogen formation rate was constant for the first 10 h or more (Fig. 32B). Under these conditions, the TON with respect to the proton reduction catalyst could be improved by simply reducing the loading of the cobaloxime (entries 3 and 4).

Table 2. Hydrogen formation using [Fe(phtmeimb)$_2$]PF$_6$ and [Co(dmgH)$_2$(py)Cl].

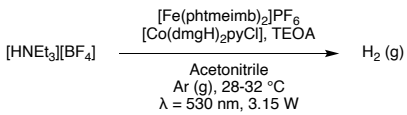

Entry	[PRC] (mM)	Time (h)	H_2 (μmol)	TON_{Co}	Initial TOF_{Co} (h^{-1})	TON_{Fe}[a]	Initial TOF_{Fe} (h^{-1})
1[a]	0.1	4	9	45	-	9	-
2[b,c]	0.1	17	100	498	-	100	-
3	0.01	21	21	1024	152	21	1.52
4	0.005	21	13	1311	152	13	0.76
5[d]	0.1	17	2	10	-	2	-
6[e]	-	17	2	-	-	1	-
7[f]	0.1	18	0	-	-	-	-

Reaction conditions: [Fe(phtmeimb)$_2$]PF$_6$ (0.5 mM), [Co(dmgH)$_2$(py)Cl] (see column 2), dmgH$_2$ (3 mM), [HNEt$_3$][BF$_4$] (165 mM) and TEOA (0.377 M) in acetonitrile (total volume 2 mL) in a 4.9 mL clear glass vial. The amount of hydrogen produced was measured at regular time intervals by Raman spectroscopy. [a]no added dmgH$_2$. [b]average of 2 replicates. [c]66 mM [HNEt$_3$][BF$_4$] used. [d][Co(dmgBF$_2$)$_2$(py)H$_2$O] used as proton reduction catalyst. [e]1 mM of PS used. [f]DCM used as solvent. Adapted from Paper IV with permission from the Royal Society of Chemistry.

Running the hydrogen formation reaction at different light intensities revealed that under the studied conditions, the TOF was limited by the rate of photoinduced charge separation, that is the quantum yield Φ of the PS (Fig. 32A and B). Therefore, improving the photosensitiser should also increase the TOF. This can be seen by comparing the initial rates of hydrogen formation using $[Fe(phtmeimb)_2]PF_6$ and $[Ru(bpy)_3]Cl_2$ (Fig. 32 B and D), where it is obvious that $[Ru(bpy)_3]Cl_2$ has a much higher initial rate of hydrogen formation.

However, comparison of the absorption spectra of the reaction solutions before and after irradiation revealed that $[Fe(phtmeimb)_2]PF_6$ exhibits significantly greater photostability than $[Ru(bpy)_3]Cl_2$ in the hydrogen formation reactions (Fig. 32C). Additionally, hydrogen production using $[Ru(bpy)_3]Cl_2$ as a photosensitiser ceased much earlier (Fig. 32D).

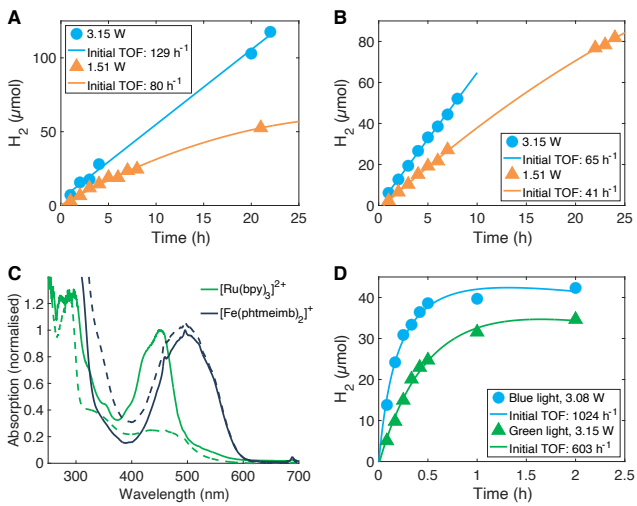

Figure 32. (A) Time trace of hydrogen formation using $[Fe(phtmeimb)_2]PF_6$ (1 mM), K_2PtCl_4 (0.05 mM), $[HNEt_3][BF_4]$ (165 mM), Et_3N (500 mM) in acetonitrile at 3.15 W (blue) and 1.51 W (orange) light intensity (λ = 530 nm). (B) Time trace of hydrogen formation using $[Fe(phtmeimb)_2]PF_6$ (0.5 mM), $[Co(dmgH)_2(py)Cl]$ (0.1 mM), $dmgH_2$ (3 mM), $[HNEt_3][BF_4]$ (165 mM), TEOA (377 mM) in acetonitrile at 3.15 W (blue) and 1.51 W (orange) light intensity (λ = 530 nm). (C) Absorption spectra of the hydrogen formation reaction solution, with $[Ru(bpy)_3]Cl_2$ (blue) and $[Fe(phtmeimb)_2]PF_6$ (green) as PS, before (solid line) and after irradiation (dashed line, 14 h and 22 h respectively). (D) Time trace of hydrogen formation with $[Ru(bpy)_3]Cl_2$ as the PS using green (λ = 530 nm) and blue (λ = 455 nm) light. Otherwise, the conditions are identical to B. Note the different time scales in A, B and D. Adapted from Paper IV with permission from the Royal Society of Chemistry.

Quenching data obtained by transient absorption spectroscopy of the excited $*[Fe^{III}(phtmeimb)_2]^+$ showed a slightly higher quenching rate for Et_3N ($k_q = 7.8 \times 10^9$ M^{-1} s^{-1}) than for TEOA ($k_q = 1.3 \times 10^9$ M^{-1} s^{-1}), which is also reflected in the higher quenching yield η_q (88% vs 51%, Table 3). For both quenchers, the cage escape yield

(η_{ce}) was very low, 2% and 3% respectively. The low cage escape yields also explain the very low quantum yields (Φ_{H_2} = 1.1% and 1.3%). Other studies have shown that the choice of solvent can have a large impact on the cage escape yield and have demonstrated cage escape yields of up to 63% with aniline based quenchers in DCM.[50] We did however not observe any hydrogen formation in DCM (Table 2, entry 7), which shows that the solvent choice influences many reaction parameters at the same time.

Direct oxidative quenching of $*[Fe^{III}(phtmeimb)_2]^+$ by $[Co(dmgH)_2pyCl]$ was also possible (Table 3, entry 3), which proceeded predominantly via static quenching. However, the large difference in concentration between the cobaloxime proton reduction catalyst and the amine sacrificial electron donors (>3 orders of magnitude) indicates that the principal pathway is through quenching of $*[Fe^{III}(phtmeimb)_2]^+$ by the amines.

Table 3. Excited state quenching data for $[Fe(phtmeimb)_2]^+$ and quantum yield of hydrogen formation in acetonitrile.

Quencher	K_{SV} (M^{-1})[a]	k_q (10^9 $M^{-1}s^{-1}$)[b]	η_q ; [Q] (mM)[c]	η_{ce}[d]	Φ_{H_2}[e]
Et_3N	15.6	7.8	88% ; 500	2%	1.1%[f]
TEOA	2.62	1.3	51% ; 377	3%	1.3%[g]
$[Co(dmgH)_2pyCl]$	114.2	-[h]	<1% ; 0.1	-[i]	-[j]

[a]Stern–Volmer constant [b]Bimolecular quenching rate constant. [c]Quenching yield with donor concentration used for hydrogen formation. [d]Cage escape yield. [e]Quantum yield of hydrogen formation. [f]With colloidal Pt. [g]With $[Co(dmgH)_2(py)Cl]$. [h]Predominatly static quenching with minor dynamic component (5.4×10^9 $M^{-1}s^{-1}$). [i]No detectable quenching products. [j]No hydrogen formation via oxidative quenching with $[Co(dmgH)_2(py)Cl]$. Adapted from Paper IV with permission from the Royal Society of Chemistry.

With these data at hand, we proposed the mechanism depicted in scheme 16. As the sacrificial quencher concentration is much higher than the proton reduction catalyst concentration, a first reductive quenching step by the sacrificial reductant is likely. The reduced $[Fe^{II}(phtmeimb)_2]$ can then do single electron transfer to the proton reduction catalyst. In the decomposition pathway of the sacrificial amine, a highly reducing α-amino radical (estimated E^o = −2.0 V[166] to −1.6 V[167] vs SCE) is generated, which is also capable of reducing the proton reduction catalyst. We propose that this α-amino radical is the species actually responsible for the more demanding $Co^{II} \rightarrow Co^{I}$ reduction.

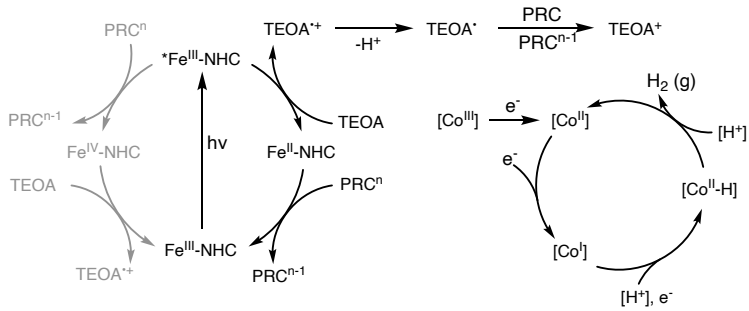

Scheme 16. Proposed mechanism for the cobaloxime catalysed hydrogen formation. Reproduced from Paper IV with permission from the Royal Society of Chemistry.

5.1.2 Conclusion

In conclusion, this study represents the first instance of substantial hydrogen production driven by an iron-based photosensitiser. Although the reaction proceeded more slowly compared to when using a more efficient photosensitiser, $[Ru(bpy)_3]Cl_2$, $[Fe(phtmeimb)_2]PF_6$ demonstrated significantly better stability under the reaction conditions. This stability suggests that further optimization of the iron photosensitiser could lead to notable improvements in both quantum yields and turnover numbers. Current efforts are also focused on employing water as the proton source and investigating the challenges encountered so far. Additionally, a long-term objective is to eliminate the use of sacrificial reductants, potentially by transitioning to photoelectrochemical systems or by coupling the reaction to an oxygen evolution reaction, thereby achieving true photocatalytic water splitting.

5.2 Studies towards CO_2 reduction driven by an Fe-NHC complex

Encouraged by the successful implementation of our photosensitiser in hydrogen formation reactions, we ventured into another aspect of artificial photosynthesis, CO_2 reduction.[168] CO_2 capturing and utilisation is foreseen to be a necessity to minimise global warming.[169] The reduction of CO_2 into chemical building blocks and fuels is even more challenging than the reduction of protons to hydrogen. Single electron reduction of CO_2 to $CO_2^{\bullet-}$ is highly endergonic and requires a reduction potential of –2.2 V vs SCE.[170] Additionally, due to the structural change from linear CO_2 to bent $CO_2^{\bullet-}$, a large kinetic overpotential is necessary. By instead doing proton-coupled reduction of CO_2, the reduction can be made more thermodynamically favourable. In this way, the reduced protons are either incorporated into the CO_2 reduction product

or forming water. Depending on how many steps CO_2 is reduced, a range of different products can be formed as shown below (potentials in aqueous solutions at pH 7).[58,171]

$$CO_2 + 2H^+ + 2e^- \rightarrow HCO_2H \qquad E^o = -0.86 \text{ V vs SCE} \qquad (22)$$

$$CO_2 + 2H^+ + 2e^- \rightarrow CO + H_2O \qquad E^o = -0.77 \text{ V vs SCE} \qquad (23)$$

$$CO_2 + 4H^+ + 4e^- \rightarrow C + 2H_2O \qquad E^o = -0.45 \text{ V vs SCE} \qquad (24)$$

$$CO_2 + 4H^+ + 4e^- \rightarrow HCHO + H_2O \qquad E^o = -0.73 \text{ V vs SCE} \qquad (25)$$

$$CO_2 + 6H^+ + 6e^- \rightarrow CH_3OH + H_2O \qquad E^o = -0.63 \text{ V vs SCE} \qquad (26)$$

$$CO_2 + 8H^+ + 8e^- \rightarrow CH_4 + 2H_2O \qquad E^o = -0.49 \text{ V vs SCE} \qquad (27)$$

$$2H^+ + 2e^- \rightarrow H_2 \qquad E^o = -0.65 \text{ V vs SCE} \qquad (28)$$

A challenge with CO_2 reduction is that a reduction catalyst needs to be able to store a large number of electrons, since the more reduced products consume up to eight electrons in the process. This also increases the likelihood of back electron transfer from the reduced catalyst to the (excited) photosensitiser. We opted for the reduction to CO, a two-electron process. CO can be used a chemical building block in for instance formylation reactions or mixed with hydrogen to form syngas. The formation of hydrogen from protons is a directly competing reaction in many CO_2 reduction reactions, and much of the research in this field is centred at directing the selectivity between the two.

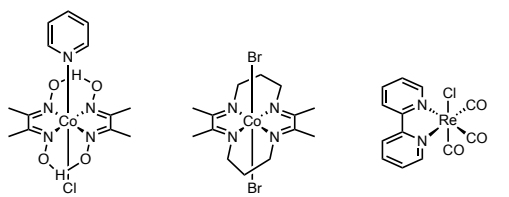

17 [Co(dmgH)$_2$(py)Cl] **19** [Co(TIM)Br$_2$] **20** *fac*-[Re(bpy)(CO)$_3$Cl]

Figure 33. CO_2 reduction catalysts investigated in this work.[165,172,173]

The cobalt-based catalysts (Fig. 33) did not show any substantial CO_2 reduction (Table 4), although the [Co(dmgH)$_2$pyCl] (entries 3 and 4) was able to produce substantial amounts of hydrogen gas under the reaction conditions. This is not surprising, given the previous work where this catalyst was used for proton reduction, and one could imagine at least two different proton sources for the hydrogen evolved. The dissolved

CO_2 will make a slightly acidic solution together with any water in the solvent, which could then provide the necessary protons for hydrogen formation. Alternatively, it could be the amine sacrificial reductant after oxidative quenching, $TEOA^{\bullet+}$, that provided the protons.

Table 4. Results from photocatalytic CO_2 reduction reactions using cobalt based CO_2 reduction catalysts.

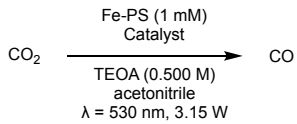

Entry	Catalyst	[Cat] (mM)	PS	H_2 (µmol)	CO (µmol)	TON_{H2}	TON_{CO}
1	$[Co(TIM)Br_2]$	5	$[Fe(phtmeimb)_2]PF_6$	0	0		
2	$[Co(TIM)Br_2]$	5	$[Fe(btz)_3](PF_6)_3$	0	0		
3[a]	$[Co(dmgH)_2pyCl]$	0.5	$[Fe(phtmeimb)_2]PF_6$	60.7	3.41	60.7	3.41
4[a,b]	$[Co(dmgH)_2pyCl]$	0.05	$[Fe(phtmeimb)_2]PF_6$	51.1	0	511	
5[a]	$[Co(dmgH)_2pyCl]$	0.5	$[Fe(btz)_3](PF_6)_3$	0	0		

Reaction conditions: PS (1 mM), CO_2 reduction catalyst (see column 3), TEOA (0.500 M), acetonitrile, total reaction volume 2 mL in a 4.9 mL clear glass vial, 21–22 h reaction time. The vial was purged with CO_2 prior to irradiation. The H_2 and CO_2 content was determined in the gas phase using Raman spectroscopy. All samples are duplicates. [a]3 mM $dmgH_2$ added to stabilise the catalyst. [b]0.5 mM PS.

Another class of CO_2 reduction catalysts that has been used previously are rhenium bipyridyl complexes, which have been used both as standalone photocatalysts[173] and together with photosensitisers[174]. Notably, this class of complexes has very low absorption above 500 nm, and has been used with transition metal photosensitisers and green light for the reduction of CO_2 to CO.[175] Initial experiments were promising, as the combination of $[Fe(phtmeimb)_2]PF_6$, *fac*-$[Re(bpy)(CO)_3Cl]$ and TEOA in DMF was able to reduce CO_2 to CO (Table 5, entries 3 and 5).

Rather quickly it was however discovered that the Re complex was able to act as a photocatalyst on its own, meaning that the photosensitiser was not taking part in the reaction. Lowering the concentration of *fac*-$[Re(bpy)(CO)_3Cl]$ did still produce comparable amounts of CO with or without the Fe PS (entries 9 and 10). It seems like the minuscule absorption by *fac*-$[Re(bpy)(CO)_3Cl]$ at λ = 530 nm is enough to drive the reaction, which is peculiar since the same type of complex has previously not produced any CO under green light irradiation.[175]

Table 5. Results from photocatalytic CO_2 reduction reactions using *fac*-[Re(bpy)(CO)$_3$Cl] as CO_2 reduction catalyst.

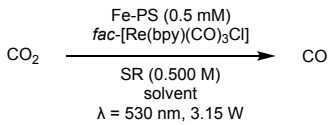

Entry	PS	[Cat] (mM)	SR	Solvent	CO (µmol)	TON_{CO}
1	$[Fe(phtmeimb)_2]PF_6$	0.5	TEOA	MeCN	0	0
2	$[Fe(phtmeimb)_2]PF_6$	0.5	Et_3N	MeCN	0	0
3	$[Fe(phtmeimb)_2]PF_6$	0.5	TEOA	DMF	40.5	40.5
4	$[Fe(phtmeimb)_2]PF_6$	0.5	Et_3N	DMF	0	0
5	$[Fe(phtmeimb)_2]PF_6$	0.25	TEOA	DMF	2.59	5.2
6	$[Fe(phtmeimb)_2]PF_6$	0.1	TEOA	DMF	0	0
7	$[Fe(btz)_3](PF_6)_3$	0.5	TEOA	MeCN	0	0
8	$[Fe(btz)_3](PF_6)_3$	0.5	TEOA	DMF	8.1	8.1
9	-	0.5	TEOA	DMF	35.8	35.8
10	-	0.25	TEOA	DMF	4.0	8.1
11	-	0.1	TEOA	DMF	0	0

Reaction conditions: PS (0.5 mM), CO_2 reduction catalyst (see column 3), sacrificial reductant (SR, 0.500 M) in acetonitrile (MeCN) or dimethylformamide (DMF), total reaction volume 2 mL in a 4.9 mL clear glass vial, 18–20 h reaction time. The vial was purged with CO_2 prior to irradiation. The CO_2 content was determined in the gas phase using Raman spectroscopy. No H_2 was detected in any reaction. All samples are at least duplicates.

The use of iron photosensitisers for CO_2 reduction still remains an open quest. The iron photosensitisers studied here may be compatible with other CO_2 reduction catalysts, or new designs of the photosensitisers and catalysts might be needed to obtain a working system. The reasons why the CO_2 reduction did not pan out could be many, such as inefficient electron transfer from the Fe^{II} state to the catalysts, poor cage escape yields, or back electron transfer from the one electron reduced catalyst to the Fe PS before accumulation of the two electrons needed for reduction of CO_2. More thorough investigations into the photochemistry of these systems are therefore needed to understand how to optimise them.

6 ATRA reaction driven via biphotonic photoredox catalysis using $[Fe(btz)_3](PF_6)_3$ (Paper V)

The Atom Transfer Radical Addition (ATRA)[176] is a means to add an alkyl halide over an alkene and was pioneered in 1945 by Kharasch[177,178], using peroxides as radical initiators, and further developed by Curran[179,180] in the late 1980s. In 2011, during the second wave of photoredox catalysis, the group of Stephenson realised that the reaction could be driven by visible light irradiation of $[Ir^{III}(dF(CF_3)ppy)_2(dtbbpy)]PF_6$.[181] It has since become a benchmark reaction in photoredox catalysis.[182] The synthetic value lies in the atom economical simultaneous installation of an alkyl group and a halide in a regioselective fashion. The halide provides a useful synthetic handle for further functionalisation. We chose to investigate this reaction, with the aim to drive the reaction using a photoactive iron complex as the photoredox catalyst.

6.1 Results and discussion

The ATRA reaction between perfluorooctyl iodide and 5-hexenol was chosen as a model reaction (Scheme 17). The photocatalytic reaction can be run in a reductive or oxidative quenching cycle (cf. Fig. 12B). In the initial investigations, the reaction was therefore optimised both with and without added sacrificial reductants, such as sodium ascorbate and Et_3N. At first $[Fe^{III}(phtmeimb)_2]PF_6$ was used as the photocatalyst, chosen for its long ^{2}LMCT lifetime. Unfortunately, this complex gave inconsistent results with wildly varying yields. When switching to $[Fe^{III}(btz)_3](PF_6)_3$ — with a shorter ^{2}LMCT lifetime of τ = 100 ps compared to τ = 2.0 ns for $[Fe^{III}(phtmeimb)_2]PF_6$ — the reaction yields became much more reproducible. After some optimisation, the optimal conditions were found to be 1 equivalent of the alkene and 1.33 equivalents of the alkyl halide. In the reductive route 0.5 mol% of $[Fe^{III}(btz)_3](PF_6)_3$ and 0.34 equivalents of Et_3N were used, and in the oxidative route 1.5 mol% of $[Fe^{III}(btz)_3](PF_6)_3$. The reductive route had the advantage of shorter reaction times, typically 10 minutes vs 40 minutes for the oxidative route. On the other hand, the

oxidative route is more atom economical, as it obviates the use of Et_3N as a sacrificial reductant. In both reaction modes, a scope of >12 different products was produced (Scheme 17).

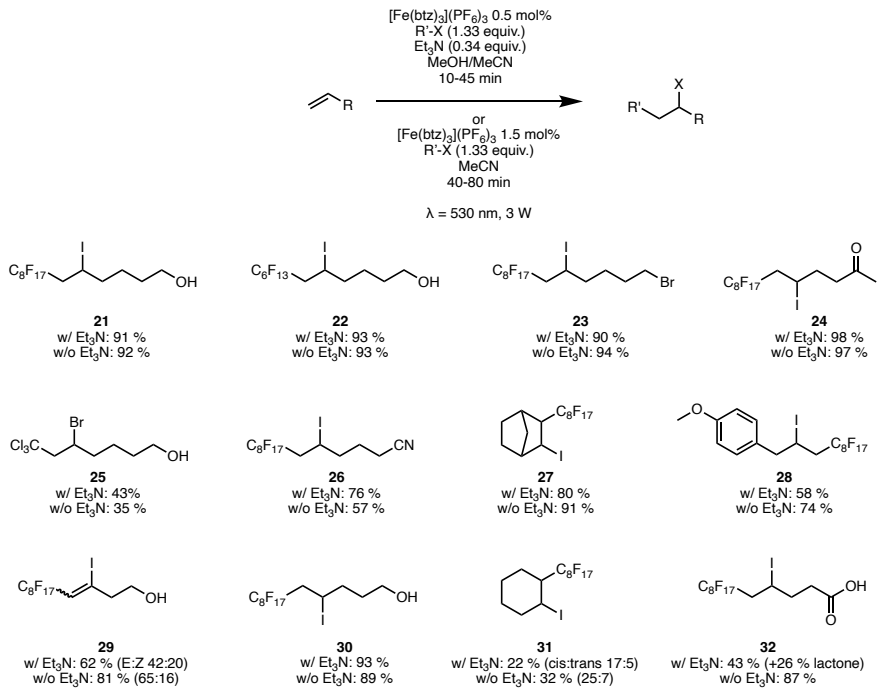

Scheme 17. Product scope of the reductive and oxidative ATRA using $[Fe(btz)_3](PF_6)_3$ as the photoredox catalyst.

Not all alkenes did successfully participate in the ATRA reaction (Scheme 18). Common for several of these unsuccessful substrates is the conjugation of the alkene to an electron-withdrawing group. The resulting low-lying LUMO and its interaction with the excited photosensitiser could be a reason for the absence of product. Another reason could be an incompatibility in energy levels between the singly occupied molecular orbital (SOMO) of the perfluorooctyl radical and frontier orbitals of the alkene.

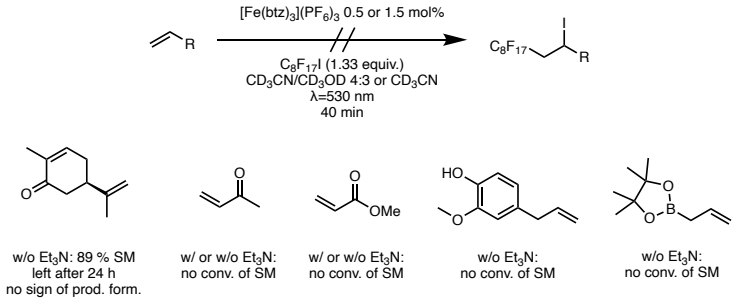

Scheme 18. Unsuccessful substrates in the ATRA reaction.

The ATRA reaction of a substrate set up for an intramolecular reaction showed that the reaction was possible with a bromomalonate (Scheme 19), which was not reactive in the intermolecular reaction. Selectivity studies showed a strong preference for terminal alkenes over internal (none of the internal addition products was detected) and preferential initial addition to an alkene over an alkyne (Scheme 19).

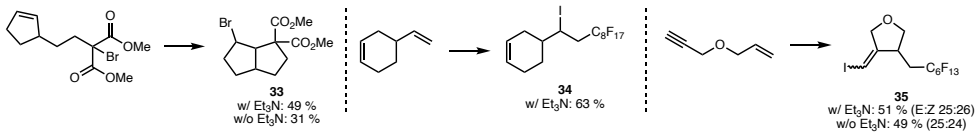

Scheme 19. Intramolecular ATRA reaction and selectivity studies. Same conditions as in scheme 18.

Together with our collaborators in Uppsala, we tried to elucidate the mechanism behind the ATRA reactions. The quenching of the excited state was investigated under conditions as close to the reaction conditions as possible (Table 6). The quenching experiments for the reductive route were done in the same solvent system, acetonitrile/methanol 4:3. Dynamic quenching of $*[Fe^{III}(btz)_3]^{3+}$ by Et_3N (k_q = 8.4 × 10^9 M^{-1} s^{-1}) was observed in the reaction solvent used for the reductive ATRA, with a similar quenching rate as previously observed for $*[Fe^{III}(phtmeimb)_2]^{+}$ with Et_3N in acetonitrile (k_q = 7.8 × 10^9 M^{-1} s^{-1}, cf. tables 3 and 6). The lower quenching efficiency η_q is due to the shorter excited state lifetime of $*[Fe^{III}(btz)_3]^{3+}$ compared to $*[Fe^{III}(phtmeimb)_2]^{+}$. Despite these similarities in quenching rates, the big difference is in the cage escape yields. The cage escape yield after single electron transfer from Et_3N to $*[Fe^{III}(btz)_3]^{3+}$ is here 29%, an order of magnitude higher than what was observed in the hydrogen evolution reaction for $*[Fe^{III}(phtmeimb)_2]^{+}$ and Et_3N. In the solvent mixture used for the reductive ATRA, no quenching of $*[Fe^{III}(btz)_3]^{3+}$ by the alkyl halide, $C_8F_{17}I$, or the alkene, 5-hexenol, was observed.

Reductive quenching of $*[Fe^{III}(btz)_3]^{3+}$ by Et_3N results in $[Fe^{II}(btz)_3]^{2+}$, which also absorbs light at 530 nm, the wavelength used in the ATRA reaction. The quenching of $*[Fe^{II}(btz)_3]^{2+}$ was therefore investigated, and it was found that $*[Fe^{II}(btz)_3]^{2+}$ is indeed quenched by $C_8F_{17}I$ (Table 6).

Table 6. Excited state quenching data for the reductive ATRA reaction in acetonitrile/methanol (4:3)

	$[Fe^{III}(btz)_3]^{3+}$ (τ_{LMCT} = 94 ps)				$[Fe^{II}(btz)_3]^{2+}$ (τ_{MLCT} = 330 ps)
	K_{SV} (M^{-1})	k_q (10^9 $M^{-1}s^{-1}$)	η_q ; [Q] (M)	η_{ce}	$\eta_q\eta_{ce}$; [Q] (M)
Et_3N	0.81[a]	8.4	31% ; 0.50	29%[b]	0 ; ≤0.50[e]
$C_8F_{17}I$	n.a.[c]	n.a.	0 ; ≤0.45[d]	n.a.	18%[b] ; 0.45[f, g]
5-hexenol	n.a.	n.a.	0 ; ≤0.14[d]	n.a.	0 ; ≤0.14[e]

K_{SV} = Stern–Volmer quenching rate, k_q = bimolecular rate constant, η_q = quenching yield, [Q] = quencher concentration, η_{ce} = cage escape yield, $\eta_q\eta_{ce}$ = quantum yield of the charge separated products. [a]Stern–Volmer constant from steady-state emission quenching. [b]±20%. [c]Not applicable. [d]No emission quenching up to indicated quencher concentration. [e]No detectable products in ns-transient absorption. [f]From ns-transient absorption. [g]$\eta_{ce} \geq 30\%$ with $\eta_q(0.45\ M) \leq 60\%$ (based on $k_q \leq 2\times10^{10}\ M^{-1}s^{-1}$). Table adapted from Paper V with permission of the Royal Society of Chemistry.

This led us to hypothesise that the reaction could be driven by dual excitation of both the Fe^{III} and the Fe^{II} complex by so-called consecutive photoinduced electron transfer.[183–186] Both species absorb light at λ = 530 nm, the irradiation wavelength of the reaction. To support this mechanism, an experiment was devised to verify the involvement of both species (Fig. 34). Irradiation (λ = 525 nm) of a vial containing the photoredox catalyst, $[Fe(btz)_3](PF_6)_3$, the sacrificial reductant, Et_3N, and the alkene, 5-hexenol, but no alkyl halide, led to a colour change from red to brown. The absorption spectrum of this reaction mixture after irradiation was consistent with that of $[Fe^{II}(btz)_3]^{2+}$, showing accumulation of the Fe^{II} complex. Addition of perfluorooctyl iodide and stirring in the dark did not lead to any conversion of the starting materials (Fig. 34, B → C), a clear indication that the Fe^{II} ground state cannot drive the reaction.

On the other hand, addition of perfluorooctyl iodide to the accumulated $[Fe^{II}(btz)_3]^{2+}$ and irradiation with red light (λ = 700 nm), which is only absorbed by $[Fe^{II}(btz)_3]^{2+}$ and not by $[Fe^{III}(btz)_3]^{3+}$, led to 5% conversion of the alkene to the product (Fig. 34, B → D). These two experiments clearly indicated that under the reductive reaction conditions, the reaction was driven by the excited $*Fe^{II}$. Since the ground state Fe^{III} is not reduced by triethylamine, the reaction must proceed via dual excitation of both $[Fe^{III}(btz)_3]^{3+}$ and $[Fe^{II}(btz)_3]^{2+}$. Furthermore, the 5% conversion by only 0.5 mol% of photoredox catalyst points to the operating radical chain mechanism.

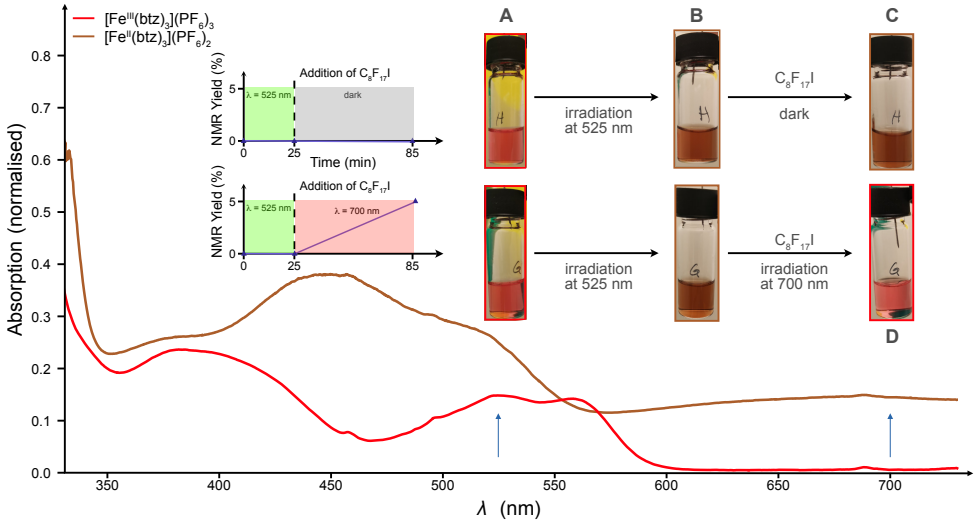

Figure 34. Wavelength-switching experiment for the visible-light-driven ATRA reaction of $C_8F_{17}I$ with 5-hexen-1-ol using $[Fe(btz)_3](PF_6)_3$ as photoredox catalyst and Et_3N as sacrificial reductant supporting the involvement of consecutive photoinduced electron transfer. The absorption spectra of the reaction solutions containing $[Fe^{III}(btz)_3](PF_6)_3$ (red line) and in-situ generated $[Fe^{II}(btz)_3](PF_6)_2$ (brown line) are shown. Blue arrows indicate the irradiation wavelenghts (λ = 525 nm and λ = 700 nm. (A) A solution of $[Fe(btz)_3](PF_6)_3$ (0.357 mM), 5-hexenol (71.4 mM), Et_3N (23.6 mM) & mesitylene (15 µL, internal standard) in acetonitrile/methanol (4:3) was irradiated at λ = 525 nm for 25 min. (B) Addition of $C_8F_{17}I$ (95 mM). (C) Reaction solution after addition of alkyl halide and storing in the dark for 1 h; no product formation. (D) Reaction solution after addition of the alkyl halide and irradiation at λ = 700 nm for 60 min; 5% NMR yield of product. Figure adapted from Paper V with permission from the Royal Society of Chemistry.

Therefore, the reaction mechanism of the reductive ATRA is proposed to proceed through the excitation of $[Fe^{III}(btz)_3]^{3+}$ and subsequent quenching of the ^{2}LMCT state by Et_3N to yield $[Fe^{II}(btz)_3]^{2+}$ (Scheme 20). Excitation of Fe^{II} to $*Fe^{II}$ makes it reducing enough to perform single electron transfer to the alkyl halide, which then undergoes radical addition to the alkene. The thus-formed alkyl radical can initiate radical chain propagation, which also operates under our reaction conditions (Φ_{prod} = 6). Substantial accumulation of Fe^{II} is not likely under the reaction conditions since the extinction coefficient ε of $[Fe^{II}(btz)_3]^{2+}$ at λ = 530 nm is higher than that of $[Fe^{III}(btz)_3]^{3+}$. Furthermore, the quantum yield for the quenching of $*[Fe^{II}(btz)_3]^{2+}$ by perfluorooctyl iodide is higher than for quenching of $*[Fe^{III}(btz)_3]^{3+}$ by Et_3N.

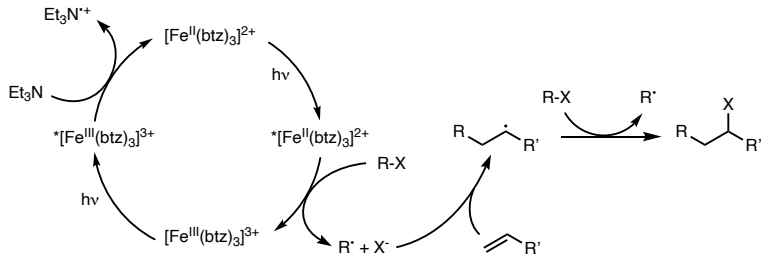

Scheme 20. Proposed reaction mechanism for the reductive ATRA using Et_3N as the sacrificial reductant.

Under the conditions used in the oxidative route, quenching of $*[Fe^{III}(btz)_3]^{3+}$ by perfluorooctyl iodide could be seen (Table 7), with a quenching rate comparable to the quenching rates in the reductive ATRA. However, the cage escape yield η_{ce} was too low to detect any oxidised iron complex, formally $[Fe^{IV}(btz)_3]^{4+}$. This would explain the higher photoredox catalyst loading needed in the oxidative route.

Table 7. Excited state quenching data for the oxidative ATRA reaction in acetonitrile.

	$[Fe^{III}(btz)_3]^{3+}$ (τ_{LMCT} = 100 ps)			
	K_{SV} (M^{-1})	k_q (10^9 $M^{-1}s^{-1}$)	η_q ; [Q] (M)	η_{ce}
$C_8F_{17}I$	0.43[a]	4.3	9% ; 0.12	<0.15[d]
5-hexen-1-ol	n.a.[b]	n.a.	0% ; ≤0.14[c]	n.a.

[a]From steady-state emission quenching. [b]Not applicable. [c]No emission quenching up to indicated quencher concentration. [d]Estimated from absence of detectable ns-transient absorption. Table adapted from Paper V with permission from the Royal Society of Chemistry.

Based on the data presented in table 7, we propose that in the oxidative mechanism $*[Fe^{III}(btz)_3]^{3+}$ must undergo oxidative quenching by perfluorooctyl iodide (Scheme 21) to form the oxidised complex. The complex is most likely oxidised on the metal, and formally denoted as $[Fe^{IV}(btz)_3]^{4+}$ but could also be $[Fe^{III}(btz^{\bullet+})(btz)_2]^{4+}$.[54] The formed alkyl radical can then add to the alkene and initiate a radical chain reaction in the same fashion as in the reductive ATRA. A radical chain mechanism operating was also substantiated by the quantum yield of $\Phi = 4.5$. $[Fe^{IV}(btz)_3]^{4+}$ is known to be very short-lived but might survive long enough to get reduced back to the initial $[Fe^{III}(btz)_3]^{3+}$ by the alkyl radical (left part of Scheme 21). The presence of the highly unstable oxidised complex in the catalytic cycle would also explain why the photoredox catalyst degrades over the course of the reaction. To investigate the longevity of the photoredox catalyst, repeated addition of new starting materials at the end of the reaction was performed. In the reductive route, the activity of the photoredox catalyst was largely preserved over several cycles, whereas in the oxidative route the yield in subsequent reactions dropped substantially.

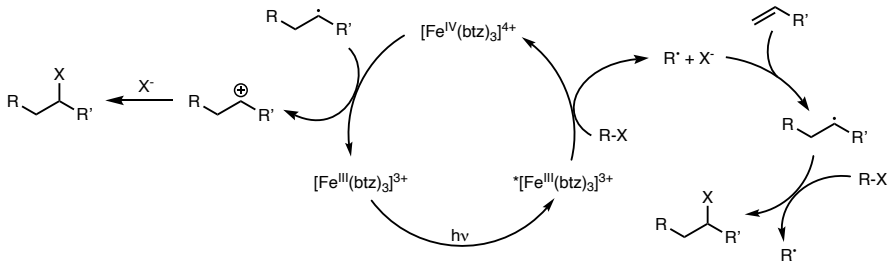

Scheme 21. Proposed reaction mechanism for the oxidative ATRA.

6.2 Conclusion

In this study, a fluorinated alkyl chain and an iodine were installed simultaneously in one photocatalytic reaction. Fluorinated compounds play an important role in medicinal chemistry, where the installation of a single trifluoromethyl group can have drastic effects on the bioactivity of a molecule.[187,188]

During the work on photoredox catalysis driven by direct quenching of the CT state of an iron complex, several important discoveries were made. The mechanism in the reductive cycle was very different from that of $[Ru(bpy)_3]^{2+}$ in the same reaction. It marked the first instance of single electron transfer from the ^{3}MLCT state of an iron complex, and furthermore is an example of consecutive photoinduced electron transfer – a reaction mode still rare in photoredox catalysis. The consecutive excitation of two different oxidation states in the reductive route provides a larger thermodynamic driving force than what is available in a conventional single excitation catalytic cycle.[186] This is resemblant of the Z-scheme in natural photosynthesis and enables access to more extreme reduction potentials than single-photon photoredox catalysis. In our case, this is possible because of the relatively long-lived excited states of both the Fe^{III} and Fe^{II} complexes, which provides a promising strategy for enhanced reactivity. To design such systems, it is essential to prioritise ligands that create a large ligand field, as this extends both the Fe^{III} τ_{LMCT} as well as the Fe^{II} τ_{MLCT}. Additionally, ligands and metal centres should exhibit reversible redox behaviour, ensuring the stability of both Fe^{II} and Fe^{III} oxidation states — an inherent feature of many iron complexes.

Furthermore, the project demonstrates what a profound effect changes in solvent composition can have. The oxidative route was possible in pure acetonitrile, however, no quenching of $*[Fe^{III}(btz)_3]^{3+}$ by the alkyl halide was observed in the solvent mixture used in the reductive route (acetonitrile/methanol 4:3).

This project showcased that iron complexes can actually be used for outer-sphere photoredox catalysis, despite their relatively short excited state lifetimes. The

consecutive photoinduced electron transfer mechanism revealed the potential for novel reaction mechanisms possible with this type of iron complexes. With further developments of iron-based photoredox catalysts, it is likely that even more chemical transformations can be realised, and that this class of photoredox catalysts could become adopted by the wider organic synthesis community.

7 Concluding remarks and outlook

This thesis had two overarching aims. The first was to increase the excited state lifetimes of iron complexes in order to make them more competent as photosensitisers and photocatalysts. The second aim was to apply iron complexes as photosensitisers in artificial photosynthesis and in photoredox catalysis.

Although the first aim was not fully achieved, several discoveries were made. The first design strategy was to extend the π-system of the ligand, by replacing imidazole with imidazo[1,5-*a*]pyridine, to go from $[Fe^{III}(phtmeimb)_2]^+$ to $[Fe^{III}(PhB(ImPy)_3)_2]^+$. This led to a significant redshift of the LMCT band. At the same time, the ^{2}LMCT lifetime was drastically shortened. As DFT calculations indicated that the ^{2}LMCT → ^{4}MC barrier was raised, we explain this shorter lifetime by the smaller energy gap between the ^{2}LMCT state and the ^{2}GS. For $[Fe^{II}(PhB(ImPy)_3)_2]$, we discovered a very long-lived excited state with a lifetime of 120 ns. The nature of this excited state remains to be determined.

Another design strategy was to incorporate a strongly σ-donating and π-accepting cyclometallated phenyl group in combination with NHC ligands in an iron complex, in order to increase the ligand field splitting further. In the investigation of the resulting complex, $[Fe^{III/II}(ImP)_2]^{+/0}$, it was discovered that the reported ns lifetime of the $^*Fe^{III}$ complex originated from an emissive impurity, not visible in the steady-state and time-resolved absorption spectra. $[Fe^{II}(ImP)_2]$ was synthesised and characterised for the first time. The lifetimes of the charge transfer excited states were concluded to be τ_{LMCT} = 240 ps and τ_{MLCT} = 9 ps, for the Fe^{III} and Fe^{II} complex, respectively. Again, the ps CT excited state lifetime can be explained by the spatial closeness between the hole and the electron in the CT states.

In chapter four, a rotational Raman-based gas analyser was presented. This instrument enabled the rapid investigation of many reaction parameters in the artificial photosynthesis reactions also studied in this thesis. It holds to the potential to be a platform both for swift screening and optimisation in gas evolving reactions, as well as for mechanistic investigations by real time monitoring of gas compositions.

In the two final studies presented in this thesis, iron complexes were employed as a photosensitiser and a photocatalyst. Although labelled differently, the role of the iron

complex is the same both as a photosensitiser and as photocatalyst, to donate and accept electrons from and to the excited state.

In the context of artificial photosynthesis, this was the first example of an iron complex acting as a photosensitiser in a high-yielding hydrogen formation reaction. It was also shown that $[Fe(phtmeimb)_2]^+$ was remarkably photostable under the reaction conditions. However, changing the proton source to water, or venturing into reduction of carbon dioxide, proved more challenging, and has so far been unsuccessful. Iron complexes with more long-lived excited states, as well as redox potentials tuned for these applications, are therefore needed.

Lastly, this thesis also contains one of the first examples of a CT state of an iron complex being used for outer-sphere photoredox catalysis. Depending on the conditions, the reaction could go either through an oxidative or reductive quenching cycle. In the reductive quenching cycle, we discovered an unusual biphotonic mechanism enabling the use of the excited state of two different oxidation states of $[Fe^{III/II}(btz)_3]^{3+/2+}$. A broad substrate scope of different alkenes could be established, showing the synthetic utility of the method. We also investigated the mechanism using a range of different techniques, determining quenching yields as well as cage escape yields. This is rarely done in photoredox catalysis, which holds back both understanding and progress in the field.[189]

At the current point, creating long-lived Fe^{II} ^{3}MLCT states suitable for photoredox catalysis seems to be a much more daunting task, than doing the same with Fe^{III} ^{2}LMCT states. A possible explanation for this is that many of the designs, in particular those based on NHC ligands, rely on a strategy with strongly σ-donating ligands to raise the e_g orbitals and thereby increasing the ligand field splitting. However, this approach also tends to stabilise a more oxidised iron core (Fe^{III} vs Fe^{II}), because of the strong electron donation from the ligands. NHC ligands may well not be the most effective strategy for Fe^{II} complexes, as the two most long-lived Fe^{II} ^{3}MLCT states currently belong to a cyclometallated phenanthroline iron complex[40], and a macrocyclic iron complex with nested potentials[41]. Nonetheless, one Fe^{II} complex, $[Fe^{II}(btz)_3]^{2+}$, has now by us been employed in photoredox catalysis, in a process where it was reduced $Fe^{III} \rightarrow Fe^{II}$ in situ in the catalytic cycle.

From the comparison of the excited state dynamics of $[Fe^{III}(phtmeimb)_2]^+$, $[Fe^{III}(PhB(ImPy)_3)_2]^+$ and $[Fe^{III}(ImP)_2]^+$, several conclusions can be drawn. The spin-allowed deexcitation ^{2}LMCT $\rightarrow$ ^{2}GS in combination with the higher lying ^{4}MC excited state changes how these excited complexes decay back to the ground state. From the ^{2}LMCT state there are three possible paths back to the GS: (1) fluorescence ^{2}LMCT $\rightarrow$ ^{2}GS, (2) nonradiative direct decay ^{2}LMCT $\rightarrow$ ^{2}GS, and (3) nonradiative decay via the ^{4}MC state. Temperature dependent transient absorption spectroscopy studies of $[Fe^{III}(phtmeimb)_2]^+$ have shown that at room temperature, the barrier from the ^{2}LMCT

state to the ^{2}MC state is so high, that the main deactivation pathway of $^*[Fe^{III}(phtmeimb)_2]^+$ is through nonradiative direct decay ^{2}LMCT → ^{2}GS.[190] Impeding vibrational relaxation could enhance both the luminescence quantum yield and the excited-state lifetime. This may be achieved by increasing the structural rigidity of the complex, thereby slowing down vibrational relaxation.[191–193]

This non-radiative decay also depends on the energy gap between the states, as exemplified by $[Fe^{III}(PhB(ImPy)_3)_2]^+$, where the low energy gap leads to a ^{2}LMCT state lifetime of 14 ps. In the case of $[Fe^{II}(PhB(ImPy)_3)_2]$, if we presume that the 120 ns excited state is a ^{3}MC state, the ultrafast ^{3}MLCT → ^{3}MC IC could be due to increased electronic coupling between the states. DFT calculations suggest that the MLCT state is localised on the NHC-ligands instead of on the phenyl group as in $[Fe^{II}(phtmeimb)_2]$, closer in space to the MC state.

From this, we can conclude that several strategies must be combined in order to further increase the CT lifetimes of photoactive iron complexes. In addition to the successful strategy of using strongly σ-donating ligands, new designs should also aim to increase the rigidity of the complexes to slow down non-radiative direct decay to the ground state, while at the same time maintaining a spatial separation of the HOMO and LUMO orbitals.

Another aspect, still underexplored in the context of photoactive Fe^{III} complexes, is the possible implication of the excited state being of ^{2}LMCT character. It has been proposed to give special properties to the excited state.[32,194] One key difference is the absence of ISC in the ^{2}LMCT state, which is typically observed for $^*Fe^{II}$ complexes (^{1}MLCT → ^{3}MLCT). Consequently, a larger portion of the absorbed light energy may be available for photocatalytic processes. However, this has so far not been extensively studied and a clear experimental impact is missing.

Apart from excited state lifetimes, other parameters will also have to be considered in order to improve the yields and usability of iron complexes in artificial photosynthesis and photoredox catalysis. A better understanding of the individual elemental steps is still needed, such as understanding the cage escape yield and how to improve it. While some have pointed to the role of the solvent[50], other factors such as the charge of the photocatalyst before and after electron transfer most probably also play an important role. The synthesis of Fe^{II} complexes with long-lived ^{3}MLCT states is still an important goal, as these hold promise of higher cage escape yields due to the spin-forbidden in-cage charge recombination.

While the excited-state lifetimes of iron complexes still lag behind those of noble metal catalysts, the work described in this thesis has demonstrated the superior photostability of Fe-NHC complexes and the potential of using two oxidation states in biphotonic mechanisms. Furthermore, the excited state reduction and oxidation potentials of $[Fe(phtmeimb)_2]^+$ and $[Fe(btz)_3]^{3+/2+}$ exceed those of commonly used ruthenium and

iridium photocatalysts. With continued exploration of innovative designs, including strategies such as enhancing rigidity and optimising orbital separation, iron complexes hold the potential to eventually rival noble metal complexes, paving the way for a more sustainable and cost-effective future in artificial photosynthesis and photoredox catalysis.

8 Acknowledgements

There are a number of people without whom this thesis would not have been possible, and I would like to thank them here.

First and foremost, I would like to thank my supervisor, Kenneth. I have always admired your never-ending enthusiasm for chemistry. Thank you for guidance, encouragement, and support. It's been fun and rewarding years working in your group.

I would also like to thank my co-supervisor Ulf and my department representative Ulf, for interesting discussions about research and what it means to be a PhD-student. An extended thanks to Ulf for letting me lecture in the basic organic chemistry courses, which I highly enjoyed.

Reiner, Catherine, and Minli, I am grateful for clarifying discussions and scientific exchanges on shared projects and papers. Marwa, Mawuli and especially Elena, thank you for explaining computational chemistry and photophysics in a very pedagogic way. Jussi, Mika and in particular Pasi, thank you for your endless support and troubleshooting when working with the gas analyser. My sincere thanks to all collaborators and co-authors for their valuable contributions to our collaborations.

Göran and Zoltan, I appreciate your great work with the more advanced NMR measurements in this thesis, and you trying to teach me advanced pulse schemes and other things. Anders, thank you for assistance with the computational chemistry.

I want to acknowledge the two students I supervised, Niklas and Christian, for your project work. I learned a lot from supervising you.

All the students I have been teaching, whether it has been in lab courses, exercise sessions or lectures, I have truly loved teaching you. A huge thank you for being curious, asking a thousand questions and (unknowingly) trying out pedagogical tools. I want to acknowledge Sophie, Saywan, and Lovisa for your continued support with the teaching.

The Junior FeCAB group, thanks for giving me a head-start into my PhD-studies. I would never have learnt about photophysics so quick if it hadn't been for the people from Chemical Physics. Thank you, Linnea, Iria, Yen, Edoardo, Nils and Pavel. Thank you, Jens, for technical assistance and scientific discussions.

Work at CAS runs smoothly thanks to the support of some special people – Sara and Maria, thank you for all the help and support with administrative matters throughout

the years. Kornelije, you have provided much appreciated technical assistance. Sofia, Fiona, and Annette, your assistance with mass spectrometry has been greatly helpful. Also thank you to Berit for keeping CAS such a nice place, and Bodil for administrative assistance. Katarina and all of KC purchasing are acknowledged for their help with procuring chemicals and instruments.

All the postdocs in the group, it has been very educative and fun to have you around. Thank you Om, Hao, Alpesh, Suresh, Dnyaneshwar, Yogesh, Kumkum, Arvind and Abhishek. A special thanks to Simon, for introducing me to almost every piece of knowledge I needed at the beginning of my PhD, whether it was about photoredox catalysis, hydrogen production or gas analysis.

To all the PhD-students in the group, it has been great having you as colleagues. Samuel, who would have thought that when we started our chemistry studies together ten years ago, that we now would graduate three weeks apart? It has been a lot of fun, and a constant source of assurance to have you around. Thank you for always being up for a discussion about life or chemistry. Aleks, we started our PhD-studies the same day, and worked on the same projects for over two years. I would never have gotten this far in my PhD without you. Thank you for our never-ending questions and bouncing of ideas. Samuel and Aleks, thanks also for your feedback on my thesis. Anna, thank you for being an awesome lab-mate, and showing off the best dance moves in lab 9. Vicky, you enjoyed listening to Retro FM in the lab more than I did, but you by far outweighed that with your friendliness and humour. Lisa, I have always been impressed by your knowledge and understanding. Your constant friendliness and valuable conversations have been very helpful, especially during times when I needed to share my thoughts and frustrations. Valtýr, it was a pleasure having you in the group, and thank you for being so generous and inviting. Hailiang, it was fun to have you in the group for a short period before you graduated. Eric, you have brought much joy to the group, continue with that. Clara, I wish you all the best with the photocatalysis projects, I know you will do great!

Finally, a great thank you to family and friends, for making these years a lot of fun when not being in the lab. Tora, tack för att du både stått ut med djupa suckar och gjort livet roligare & djupare under dessa år. Tack. ♡

9 References

(1) Balzani, V.; Bergamini, G.; Ceroni, P. Light: A Very Peculiar Reactant and Product. *Angew. Chem. Int. Ed.* **2015**, *54* (39), 11320–11337.

(2) Hockin, B. M.; Li, C.; Robertson, N.; Zysman-Colman, E. Photoredox catalysts based on earth-abundant metal complexes. *Catal. Sci. Technol.* **2019**, *9* (4), 889–915.

(3) Wegeberg, C.; Wenger, O. S. Luminescent First-Row Transition Metal Complexes. *JACS Au* **2021**, *1* (11), 1860–1876.

(4) Dierks, P.; Vukadinovic, Y.; Bauer, M. Photoactive iron complexes: more sustainable, but still a challenge. *Inorg. Chem. Front.* **2022**, *9* (2), 206–220.

(5) Pyykkö, P. Relativistic effects in structural chemistry. *Chem. Rev.* **1988**, *88* (3), 563–594.

(6) Kaupp, M. The role of radial nodes of atomic orbitals for chemical bonding and the periodic table. *J. Comput. Chem.* **2007**, *28* (1), 320–325.

(7) McCusker, J. K. Electronic structure in the transition metal block and its implications for light harvesting. *Science* **2019**, *363* (6426), 484–488.

(8) Burstall, F. H. 34. Optical activity dependent on co-ordinated bivalent ruthenium. *J. Chem. Soc.* **1936**, 173.

(9) Bock, C. R.; Meyer, T. J.; Whitten, D. G. Electron transfer quenching of the luminescent excited state of tris(2,2'-bipyridine)ruthenium(II). Flash photolysis relaxation technique for measuring the rates of very rapid electron transfer reactions. *J. Am. Chem. Soc.* **1974**, *96* (14), 4710–4712.

(10) Liu, Y.; Persson, P.; Sundström, V.; Wärnmark, K. Fe *N*-Heterocyclic Carbene Complexes as Promising Photosensitizers. *Acc. Chem. Res.* **2016**, *49* (8), 1477–1485.

(11) Kasha, M. Characterization of electronic transitions in complex molecules. *Discuss. Faraday Soc.* **1950**, *9*, 14–19.

(12) Behera, S. K.; Park, S. Y.; Gierschner, J. Dual Emission: Classes, Mechanisms, and Conditions. *Angew. Chem. Int. Ed.* **2021**, *60* (42), 22624–22638.

(13) Del Valle, J. C.; Catalán, J. Kasha's rule: a reappraisal. *Phys. Chem. Chem. Phys.* **2019**, *21* (19), 10061–10069.

(14) Demchenko, A. P.; Tomin, V. I.; Chou, P. T. Breaking the Kasha Rule for More Efficient Photochemistry. *Chem. Rev.* **2017**, *117* (21), 13353–13381.

(15) Dunlop, D.; Ludvíková, L.; Banerjee, A.; Ottosson, H.; Slanina, T. Excited-State (Anti)Aromaticity Explains Why Azulene Disobeys Kasha's Rule. *J. Am. Chem. Soc.* **2023**, *145* (39), 21569–21575.

(16) Gawelda, W.; Cannizzo, A.; Pham, V. T.; Van Mourik, F.; Bressler, C.; Chergui, M. Ultrafast nonadiabatic dynamics of $[Fe^{II}(bpy)_3]^{2+}$ in solution. *J. Am. Chem. Soc.* **2007**, *129* (26), 8199–8206.

(17) Woodhouse, M. D.; McCusker, J. K. Mechanistic Origin of Photoredox Catalysis Involving Iron(II) Polypyridyl Chromophores. *J. Am. Chem. Soc.* **2020**, *142* (38), 16229–16233.

(18) Chan, A. Y.; Ghosh, A.; Yarranton, J. T.; Twilton, J.; Jin, J.; Arias-Rotondo, D. M.; Sakai, H. A.; McCusker, J. K.; MacMillan, D. W. C. Exploiting the Marcus inverted region for first-row transition metal–based photoredox catalysis. *Science* **2023**, *382* (6667), 191–197.

(19) Yarranton, J. T.; McCusker, J. K. Ligand-Field Spectroscopy of Co(III) Complexes and the Development of a Spectrochemical Series for Low-Spin d^6 Charge-Transfer Chromophores. *J. Am. Chem. Soc.* **2022**, *144* (27), 12488–12500.

(20) Liu, Y.; Harlang, T.; Canton, S. E.; Chábera, P.; Suárez-Alcántara, K.; Fleckhaus, A.; Vithanage, D. A.; Göransson, E.; Corani, A.; Lomoth, R.; Sundström, V.; Wärnmark, K. Towards longer-lived metal-to-ligand charge transfer states of iron(II) complexes: An N-heterocyclic carbene approach. *Chem. Commun.* **2013**, *49* (57), 6412–6414.

(21) Liu, L.; Duchanois, T.; Etienne, T.; Monari, A.; Beley, M.; Assfeld, X.; Haacke, S.; Gros, P. C. A new record excited state ^{3}MLCT lifetime for metalorganic iron(II) complexes. *Phys. Chem. Chem. Phys.* **2016**, *18* (18), 12550–12556.

(22) Duchanois, T.; Etienne, T.; Cebrián, C.; Liu, L.; Monari, A.; Beley, M.; Assfeld, X.; Haacke, S.; Gros, P. C. An Iron-Based Photosensitizer with Extended Excited-State Lifetime: Photophysical and Photovoltaic Properties. *Eur. J. Inorg. Chem.* **2015**, *2015* (14), 2469–2477.

(23) Harlang, T. C. B. B.; Liu, Y.; Gordivska, O.; Fredin, L. A.; Ponseca, C. S.; Huang, P.; Chábera, P.; Kjaer, K. S.; Mateos, H.; Uhlig, J.; Lomoth, R.; Wallenberg, R.; Styring, S.; Persson, P.; Sundström, V.; Wärnmark, K. Iron sensitizer converts light to electrons with 92% yield. *Nat. Chem.* **2015**, *7* (11), 883–889.

(24) Darari, M.; Domenichini, E.; Francés-Monerris, A.; Cebrián, C.; Magra, K.; Beley, M.; Pastore, M.; Monari, A.; Assfeld, X.; Haacke, S.; Gros, P. C. Iron(II) complexes with diazinyl-NHC ligands: impact of π-deficiency of the azine core on photophysical properties. *Dalton Trans.* **2019**, *48* (29), 10915–10926.

(25) Mengel, A. K. C.; Förster, C.; Breivogel, A.; Mack, K.; Ochsmann, J. R.; Laquai, F.; Ksenofontov, V.; Heinze, K. A Heteroleptic Push–Pull Substituted Iron(II) Bis(tridentate) Complex with Low-Energy Charge-Transfer States. *Chem. Eur. J.* **2015**, *21* (2), 704–714.

(26) Englman, R.; Jortner, J. The energy gap law for radiationless transitions in large molecules. *Mol. Phys.* **1970**, *18* (2), 145–164.

(27) Balzani, V.; Ceroni, P.; Juris, A. *Photochemistry and Photophysics*; Wiley-WCH: Weinheim, 2014.

(28) Caspar, J. V.; Meyer, T. J. Application of the energy gap law to nonradiative, excited-state decay. *J. Phys. Chem.* **1983**, *87* (6), 952–957.

(29) El-Sayed, M. A. Spin—Orbit Coupling and the Radiationless Processes in Nitrogen Heterocyclics. *J. Chem. Phys.* **1963**, *38* (12), 2834–2838.

(30) Kaufhold, S.; Wärnmark, K. Design and Synthesis of Photoactive Iron *N*-Heterocyclic Carbene Complexes. *Catalysts* **2020**, *10* (1), 132.

(31) Lindh, L.; Chábera, P.; Rosemann, N. W.; Uhlig, J.; Wärnmark, K.; Yartsev, A.; Sundström, V.; Persson, P. Photophysics and Photochemistry of Iron Carbene Complexes for Solar Energy Conversion and Photocatalysis. *Catalysts* **2020**, *10* (3), 315.

(32) Chábera, P.; Lindh, L.; Rosemann, N. W.; Prakash, O.; Uhlig, J.; Yartsev, A.; Wärnmark, K.; Sundström, V.; Persson, P. Photofunctionality of iron(III) N-heterocyclic carbenes and related d transition metal complexes. *Coord. Chem. Rev.* **2021**, *426*, 213517.

(33) Wenger, O. S. Is Iron the New Ruthenium? *Chem. Eur. J.* **2019**, *25* (24), 6043–6052.

(34) Lindh, L.; Pascher, T.; Persson, S.; Goriya, Y.; Wärnmark, K.; Uhlig, J.; Chábera, P.; Persson, P.; Yartsev, A. Multifaceted Deactivation Dynamics of Fe(II) *N*-Heterocyclic Carbene Photosensitizers. *J. Phys. Chem. A* **2023**, *127* (48), 10210–10222.

(35) Kunnus, K.; Vacher, M.; Harlang, T. C. B.; Kjær, K. S.; Haldrup, K.; Biasin, E.; van Driel, T. B.; Pápai, M.; Chabera, P.; Liu, Y.; Tatsuno, H.; Timm, C.; Källman, E.; Delcey, M.; Hartsock, R. W.; Reinhard, M. E.; Koroidov, S.; Laursen, M. G.; Hansen, F. B.; Vester, P.; Christensen, M.; Sandberg, L.; Németh, Z.; Szemes, D. S.; Bajnóczi, É.; Alonso-Mori, R.; Glownia, J. M.; Nelson, S.; Sikorski, M.; Sokaras, D.; Lemke, H. T.; Canton, S. E.; Møller, K. B.; Nielsen, M. M.; Vankó, G.; Wärnmark, K.; Sundström, V.; Persson, P.; Lundberg, M.; Uhlig, J.; Gaffney, K. J. Vibrational wavepacket dynamics in Fe carbene photosensitizer determined with femtosecond X-ray emission and scattering. *Nat. Commun.* **2020**, *11* (1).

(36) Chábera, P.; Kjaer, K. S.; Prakash, O.; Honarfar, A.; Liu, Y.; Fredin, L. A.; Harlang, T. C. B.; Lidin, S.; Uhlig, J.; Sundström, V.; Lomoth, R.; Persson, P.; Wärnmark, K. Fe^{II} Hexa *N*-Heterocyclic Carbene Complex with a 528 ps Metal-to-Ligand Charge-Transfer Excited-State Lifetime. *J. Phys. Chem. Lett.* **2018**, *9* (3), 459–463.

(37) Guo, M.; Temperton, R.; D'Acunto, G.; Johansson, N.; Jones, R.; Handrup, K.; Ringelband, S.; Prakash, O.; Fan, H.; de Groot, L. H. M.; Hlynsson, V. F.; Kaufhold, S.; Gordivska, O.; Velásquez González, N.; Wärnmark, K.; Schnadt, J.; Persson, P.; Uhlig, J. Using Iron L-Edge and Nitrogen K-Edge X-ray Absorption Spectroscopy to Improve the Understanding of the Electronic Structure of Iron Carbene Complexes. *Inorg. Chem.* **2024**, *63* (27), 12457–12468.

(38) Kjær, K. S.; Kaul, N.; Prakash, O.; Chábera, P.; Rosemann, N. W.; Honarfar, A.; Gordivska, O.; Fredin, L. A.; Bergquist, K.-E.; Häggström, L.; Ericsson, T.; Lindh, L.; Yartsev, A.; Styring, S.; Huang, P.; Uhlig, J.; Bendix, J.; Strand, D.; Sundström, V.; Persson, P.; Lomoth, R.; Wärnmark, K. Luminescence and reactivity of a charge-transfer excited iron complex with nanosecond lifetime. *Science* **2019**, *363* (6424), 249–253.

(39) Jay, R. M.; Eckert, S.; Fondell, M.; Miedema, P. S.; Norell, J.; Pietzsch, A.; Quevedo, W.; Niskanen, J.; Kunnus, K.; Föhlisch, A. The nature of frontier orbitals under systematic ligand exchange in (pseudo-)octahedral Fe(II) complexes. *Phys. Chem. Chem. Phys.* **2018**, *20* (44), 27745–27751.

(40) Leis, W.; Argüello Cordero, M. A.; Lochbrunner, S.; Schubert, H.; Berkefeld, A. A Photoreactive Iron(II) Complex Luminophore. *J. Am. Chem. Soc.* **2022**, *144* (3), 1169–1173.

(41) Malme, J. T.; Clendening, R. A.; Ash, R.; Curry, T.; Ren, T.; Vura-Weis, J. Nanosecond Metal-to-Ligand Charge-Transfer State in an Fe(II) Chromophore: Lifetime Enhancement via Nested Potentials. *J. Am. Chem. Soc.* **2023**, *145* (11), 6029–6034.

(42) Dixon, I. M.; Alary, F.; Boggio-Pasqua, M.; Heully, J.-L. The $(N_4C_2)^{2-}$ Donor Set as Promising Motif for Bis(tridentate) Iron(II) Photoactive Compounds. *Inorg. Chem.* **2013**, *52* (23), 13369–13374.

(43) Dixon, I. M.; Alary, F.; Boggio-Pasqua, M.; Heully, J.-L. Reversing the relative ^{3}MLCT– ^{3}MC order in Fe(II) complexes using cyclometallating ligands: a computational study aiming at luminescent Fe(II) complexes. *Dalton Trans.* **2015**, *44* (30), 13498–13503.

(44) Dixon, I. M.; Khan, S.; Alary, F.; Boggio-Pasqua, M.; Heully, J.-L. L. Probing the photophysical capability of mono and bis(cyclometallated) Fe(II) polypyridine complexes using inexpensive ground state DFT. *Dalton Trans.* **2014**, *43* (42), 15898–15905.

(45) Braun, J. D.; Lozada, I. B.; Kolodziej, C.; Burda, C.; Newman, K. M. E.; van Lierop, J.; Davis, R. L.; Herbert, D. E. Iron(II) coordination complexes with panchromatic absorption and nanosecond charge-transfer excited state lifetimes. *Nat. Chem.* **2019**, *11* (12), 1144–1150.

(46) Reinhard, M. E.; Sidhu, B. K.; Lozada, I. B.; Powers-Riggs, N.; Ortiz, R. J.; Lim, H.; Nickel, R.; Lierop, J. van; Alonso-Mori, R.; Chollet, M.; Gee, L. B.; Kramer, P. L.; Kroll, T.; Raj, S. L.; Driel, T. B. van; Cordones, A. A.; Sokaras, D.; Herbert, D. E.; Gaffney, K. J. Time-Resolved X-ray Emission Spectroscopy and Synthetic High-Spin Model Complexes Resolve Ambiguities in Excited-State Assignments of Transition-Metal Chromophores: A Case Study of Fe-Amido Complexes. *J. Am. Chem. Soc.* **2024**, *15*, 40.

(47) Rosemann, N. W.; Chábera, P.; Prakash, O.; Kaufhold, S.; Wärnmark, K.; Yartsev, A.; Persson, P. Tracing the Full Bimolecular Photocycle of Iron(III)–Carbene Light Harvesters in Electron-Donating Solvents. *J. Am. Chem. Soc.* **2020**, *142* (19), 8565–8569.

(48) Schwarz, J.; Ilic, A.; Johnson, C.; Lomoth, R.; Wärnmark, K. High turnover photocatalytic hydrogen formation with an Fe(II) N-heterocyclic carbene photosensitiser. *Chem. Commun.* **2022**, *58* (35), 5351–5354.

(49) Cui, Z.; Ding, J.; Gao, Y.; Li, F. Organic Light-Emitting Diodes Based on an Iron(III) Complex with Doublet Emission. *CCS Chemistry* **2022**, *4* (9), 2953–2958.

(50) Aydogan, A.; Bangle, R. E.; Cadranel, A.; Turlington, M. D.; Conroy, D. T.; Cauët, E.; Singleton, M. L.; Meyer, G. J.; Sampaio, R. N.; Elias, B.; Troian-Gautier, L. Accessing Photoredox Transformations with an Iron(III) Photosensitizer and Green Light. *J. Am. Chem. Soc.* **2021**, *143* (38), 15661–15673.

(51) Ilic, A.; Strücker, B. R.; Johnson, C. E.; Hainz, S.; Lomoth, R.; Wärnmark, K. Aminomethylations of electron-deficient compounds—bringing iron photoredox catalysis into play. *Chem. Sci.* **2024**, *15* (30), 12077–12085.

(52) Steube, J.; Kruse, A.; Bokareva, O. S.; Reuter, T.; Demeshko, S.; Schoch, R.; Argüello Cordero, M. A.; Krishna, A.; Hohloch, S.; Meyer, F.; Heinze, K.; Kühn, O.; Lochbrunner, S.; Bauer, M. Janus-type emission from a cyclometalated iron(III) complex. *Nat. Chem.* **2023**, *15* (4), 468–474.

(53) Johnson, C. E.; Schwarz, J.; Deegbey, M.; Prakash, O.; Sharma, K.; Huang, P.; Ericsson, T.; Häggström, L.; Bendix, J.; Gupta, A. K.; Jakubikova, E.; Wärnmark, K.; Lomoth, R. Ferrous and ferric complexes with cyclometalating N-heterocyclic carbene ligands: a case of dual emission revisited. *Chem. Sci.* **2023**, *14* (37), 10129–10139.

(54) Chábera, P.; Liu, Y.; Prakash, O.; Thyrhaug, E.; Nahhas, A. El; Honarfar, A.; Essén, S.; Fredin, L. A.; Harlang, T. C. B.; Kjær, K. S.; Handrup, K.; Ericson, F.; Tatsuno, H.; Morgan, K.; Schnadt, J.; Häggström, L.; Ericsson, T.; Sobkowiak, A.; Lidin, S.; Huang, P.; Styring, S.; Uhlig, J.; Bendix, J.; Lomoth, R.; Sundström, V.; Persson, P.; Wärnmark, K. A low-spin Fe(III) complex with 100-ps ligand-to-metal charge transfer photoluminescence. *Nature* **2017**, *543* (7647), 695–699.

(55) Albini, A. Some remarks on the first law of photochemistry. *Photochem. Photobiol. Sci.* **2016**, *15* (3), 319–324.

(56) Draper, J. W. XXX. On some analogies between the phænomena of the chemical rays, and those of radiant heat. *The London, Edinburgh, and Dublin Philosophical Magazine and Journal of Science* **1841**, *19* (123), 195–210.

(57) Bock, C. R.; Connor, J. A.; Gutierrez, A. R.; Meyer, T. J.; Whitten, D. G.; Sullivan, B. P.; Nagle, J. K. Estimation of excited-state redox potentials by electron-transfer quenching. Application of electron-transfer theory to excited-state redox processes. *J. Am. Chem. Soc.* **1979**, *101* (17), 4815–4824.

(58) Pavlishchuk, V. V; Addison, A. W. Conversion constants for redox potentials measured versus different reference electrodes in acetonitrile solutions at 25°C. *Inorg. Chim. Acta* **2000**, *298* (1), 97–102.

(59) Öfele, K. General Meeting of the Gesellschaft Deutscher Chemiker 1969. *Angew. Chem. Int. Ed.* **1969**, 889–930.

(60) Cetinkaya, B.; Dixneuf, P.; Lappert, M. F. A general synthesis of transition-metal carbene complexes: Cr^{0}, Fe^{0}, Ir^{I}, Ni^{II}, Pd^{II}, Pt^{II}, and Au^{I} mono- and oligo-carbene species from electron-rich olefins. *J. Chem. Soc., Chem. Commun.* **1973**, *105* (6), 206.

(61) Riener, K.; Haslinger, S.; Raba, A.; Högerl, M. P.; Cokoja, M.; Herrmann, W. A.; Kühn, F. E. Chemistry of Iron *N*-Heterocyclic Carbene Complexes: Syntheses, Structures, Reactivities, and Catalytic Applications. *Chem. Rev.* **2014**, *114* (10), 5215–5272.

(62) Kernbach, U.; Ramm, M.; Luger, P.; Fehlhammer, W. P. A Chelating Triscarbene Ligand and Its Hexacarbene Iron Complex. *Angew. Chem. Int. Ed.* **1996**, *35* (3), 310–312.

(63) Nieto, I.; Cervantes-Lee, F.; Smith, J. M. A new synthetic route to bulky "second generation" tris(imidazol-2-ylidene)borate ligands: synthesis of a four coordinate iron(II) complex. *Chem. Commun.* **2005**, 30, 3811.

(64) Muñoz, S. B.; Foster, W. K.; Lin, H.; Margarit, C. G.; Dickie, D. A.; Smith, J. M. Tris(carbene)borate Ligands Featuring Imidazole-2-ylidene, Benzimidazol-2-ylidene, and 1,3,4-Triazol-2-ylidene Donors. Evaluation of Donor Properties in Four-Coordinate $\{NiNO\}^{10}$ Complexes. *Inorg. Chem.* **2012**, *51* (23), 12660–12668.

(65) Danopoulos, A. A.; Tsoureas, N.; Wright, J. A.; Light, M. E. N-Heterocyclic Pincer Dicarbene Complexes of Iron(II): C-2 and C-5 Metalated Carbenes on the Same Metal Center. *Organometallics* **2004**, *23* (2), 166–168.

(66) Fränkel, R.; Kernbach, U.; Bakola-Christianopoulou, M.; Plaia, U.; Suter, M.; Ponikwar, W.; Nöth, H.; Moinet, C.; Fehlhammer, W. P. Homoleptic carbene complexes: Part VIII. Hexacarbene complexes. *J. Organomet. Chem.* **2001**, *617–618*, 530–545.

(67) Dexter, D. L. A theory of sensitized luminescence in solids. *J. Chem. Phys.* **1953**, *21* (5), 836–850.

(68) Fŏrster, Th. 10th Spiers Memorial Lecture. Transfer mechanisms of electronic excitation. *Discuss. Faraday Soc.* **1959**, *27* (10), 7–17.

(69) Brimioulle, R.; Lenhart, D.; Maturi, M. M.; Bach, T. Enantioselective Catalysis of Photochemical Reactions. *Angew. Chem. Int. Ed.* **2015**, *54* (13), 3872–3890.

(70) Großkopf, J.; Bach, T. Catalytic Photochemical Deracemization via Short-Lived Intermediates. *Angew. Chem. Int. Ed.* **2023**, *62* (50).

(71) Mikhnenko, O. V.; Blom, P. W. M.; Nguyen, T.-Q. Exciton diffusion in organic semiconductors. *Energy Environ. Sci.* **2015**, *8* (7), 1867–1888.

(72) Chen, R.; Intermaggio, N. E.; Xie, J.; Rossi-Ashton, J. A.; Gould, C. A.; Martin, R. T.; Alcázar, J.; MacMillan, D. W. C. Alcohol-alcohol cross-coupling enabled by S_H2 radical sorting. *Science* **2024**, *383* (6689), 1350–1357.

(73) Lowry, M. S.; Goldsmith, J. I.; Slinker, J. D.; Rohl, R.; Pascal, R. A.; Malliaras, G. G.; Bernhard, S. Single-Layer Electroluminescent Devices and Photoinduced Hydrogen Production from an Ionic Iridium(III) Complex. *Chem. Mater.* **2005**, *17* (23), 5712–5719.

(74) Larsen, C. B.; Wenger, O. S. Photoredox Catalysis with Metal Complexes Made from Earth-Abundant Elements. *Chem. Eur. J.* **2018**, *24* (9), 2039–2058.

(75) Marzo, L.; Pagire, S. K.; Reiser, O.; König, B. Visible-Light Photocatalysis: Does It Make a Difference in Organic Synthesis? *Angew. Chem. Int. Ed.* **2018**, *57* (32), 10034–10072.

(76) Nicewicz, D. A.; MacMillan, D. W. C. Merging Photoredox Catalysis with Organocatalysis: The Direct Asymmetric Alkylation of Aldehydes. *Science* **2008**, *322* (5898), 77–80.

(77) Ischay, M. A.; Anzovino, M. E.; Du, J.; Yoon, T. P. Efficient visible light photocatalysis of [2+2] enone cycloadditions. *J. Am. Chem. Soc.* **2008**, *130* (39), 12886–12887.

(78) Narayanam, J. M. R.; Tucker, J. W.; Stephenson, C. R. J. Electron-Transfer Photoredox Catalysis: Development of a Tin-Free Reductive Dehalogenation Reaction. *J. Am. Chem. Soc.* **2009**, *131* (25), 8756–8757.

(79) Lehn, J.-M.; Sauvage, J.-P. Chemical Storage of Light Energy. Catalytic Generation of Hydrogen by Visible Light or Sunlight. Irradiation of Neutral Aqueous Solutions. *Nouv. J. Chim.* **1977**, *1* (6), 449–451.

(80) Hedstrand, D. M.; Kruizinga, W. H.; Kellogg, R. M. Light induced and dye accelerated reductions of phenacyl onium salts by 1,4-dihydropyridines. *Tetrahedron Lett.* **1978**, *19* (14), 1255–1258.

(81) Pellegrin, Y.; Odobel, F. Sacrificial electron donor reagents for solar fuel production. *C. R. Chim.* **2017**, *20* (3), 283–295.

(82) Olmsted, John.; Meyer, T. J. Factors affecting cage escape yields following electron-transfer quenching. *J. Phys. Chem.* **1987**, *91* (6), 1649–1655.

(83) Goodwin, M. J.; Dickenson, J. C.; Ripak, A.; Deetz, A. M.; McCarthy, J. S.; Meyer, G. J.; Troian-Gautier, L. Factors that Impact Photochemical Cage Escape Yields. *Chem. Rev.* **2024**.

(84) Juris, A.; Balzani, V.; Barigelletti, F.; Campagna, S.; Belser, P.; von Zelewsky, A. Ru(II) polypyridine complexes: photophysics, photochemistry, eletrochemistry, and chemiluminescence. *Coord. Chem. Rev.* **1988**, *84* (C), 85–277.

(85) Wang, C.; Li, H.; Bürgin, T. H.; Wenger, O. S. Cage escape governs photoredox reaction rates and quantum yields. *Nat. Chem.* **2024**, *16* (7), 1151–1159.

(86) Marcus, R. A. On the Theory of Oxidation-Reduction Reactions Involving Electron Transfer. I. *J. Chem. Phys.* **1956**, *24* (5), 966–978.

(87) Marcus A., R. Electron Transfer Reactions in Chemistry: Theory and Experiment (Nobel Lecture). *Angew. Chem. Int. Ed.* **1993**, *32* (8), 1111–1121.

(88) Marcus, R. A. Electrostatic Free Energy and Other Properties of States Having Nonequilibrium Polarization. I. *J. Chem. Phys.* **1956**, *24* (5), 979–989.

(89) Marcus, R. A. Chemical and Electrochemical Electron-Transfer Theory. *Annu. Rev. Phys. Chem.* **1964**, *15* (1), 155–196.

(90) Delaire, J. A.; Sanquer-Barríe, M.; Webber, S. E. Role of electrostatic interaction in light-induced charge separation in polyelectrolyte bound vinyldiphenylanthracene. *J. Phys. Chem.* **1988**, *92* (5), 1252–1257.

(91) Wolff, H.-J.; Burssher, D.; Steiner, U. E. Spin-orbit coupling controlled spin chemistry of $Ru(bpy)_3^{2+}$ photooxidation: Detection of strong viscosity dependence of in-cage backward electron transfer rate. *Pure Appl. Chem.* **1995**, *67* (1), 167–174.

(92) Jayanthi, S. S.; Ramamurthy, P. Photoinduced electron transfer reactions of 2,4,6-triphenylpyrylium: solvent effect and charge-shift type of systems. *Phys. Chem. Chem. Phys.* **1999**, *1* (20), 4751–4757.

(93) Ohno, T.; Lichtin, N. N. Electron transfer in the quenching of triplet methylene blue by complexes of iron(II). *J. Am. Chem. Soc.* **1980**, *102* (14), 4636–4643.

(94) Miedlar, K.; Das, P. K. Tris(2,2'-bipyridine)ruthenium(II)-sensitized photooxidation of phenols. Environmental effects on electron transfer yields and kinetics. *J. Am. Chem. Soc.* **1982**, *104* (26), 7462–7469.

(95) Hoffman, M. Z. Cage escape yields from the quenching of excited $*Ru(bpy)_3^{2+}$ by methylviologen in aqueous solution. *J. Phys. Chem.* **1988**, *92* (12), 3458–3464.

(96) Kalyanasundaram, K.; Neumann-Spallart, M. Influence of added salts on the cage escape yields in the photoredox quenching of $Ru(bpy)_3^{2+}$ excited states. *Chem. Phys. Lett.* **1982**, *88* (1), 7–12.

(97) Das, P. K.; Encinas, M. V.; Scaiano, J. C. Laser flash photolysis study of the reactions of carbonyl triplets with phenols and photochemistry of p-hydroxypropiophenone. *J. Am. Chem. Soc.* **1981**, *103* (14), 4154–4162.

(98) de Groot, L. H. M.; Ilic, A.; Schwarz, J.; Wärnmark, K. Iron Photoredox Catalysis–Past, Present, and Future. *J. Am. Chem. Soc.* **2023**, *145* (17), 9369–9388.

(99) Gualandi, A.; Marchini, M.; Mengozzi, L.; Natali, M.; Lucarini, M.; Ceroni, P.; Cozzi, P. G. Organocatalytic Enantioselective Alkylation of Aldehydes with [Fe(bpy)$_3$]Br$_2$ Catalyst and Visible Light. *ACS Catal.* **2015**, *5* (10), 5927–5931.

(100) McCusker, J. K.; Walda, K. N.; Dunn, R. C.; Simon, J. D.; Magde, D.; Hendrickson, D. N. Subpicosecond ^{1}MLCT → ^{5}T$_2$ intersystem crossing of low-spin polypyridyl ferrous complexes. *J. Am. Chem. Soc.* **1993**, *115* (1), 298–307.

(101) Aydogan, A.; Bangle, R. E.; De Kreijger, S.; Dickenson, J. C.; Singleton, M. L.; Cauët, E.; Cadranel, A.; Meyer, G. J.; Elias, B.; Sampaio, R. N.; Troian-Gautier, L. Mechanistic investigation of a visible light mediated dehalogenation/cyclisation reaction using iron(iii), iridium(iii) and ruthenium(ii) photosensitizers. *Catal. Sci. Technol.* **2021**, *11* (24), 8037–8051.

(102) Jang, Y. J.; An, H.; Choi, S.; Hong, J.; Lee, S. H.; Ahn, K.-H.; You, Y.; Kang, E. J. Green-Light-Driven Fe(III)(btz)$_3$ Photocatalysis in the Radical Cationic [4+2] Cycloaddition Reaction. *Org. Lett.* **2022**, *24* (24), 4479–4484.

(103) Arias-Rotondo, D. M.; McCusker, J. K. The photophysics of photoredox catalysis: a roadmap for catalyst design. *Chem. Soc. Rev.* **2016**, *45* (21), 5803–5820.

(104) De Kreijger, S.; Gillard, M.; Elias, B.; Troian-Gautier, L. Spectroscopic Techniques to Unravel Mechanistic Details in Light-Induced Transformations and Photoredox Catalysis. *ChemCatChem* **2024**, *16* (1).

(105) Ilic, A. Investigation of Iron-*N*-Heterocyclic Carbene Complexes for Photocatalytic Applications, Lund University, Lund, 2024.

(106) Weller, A. Photoinduced Electron Transfer in Solution: Exciplex and Radical Ion Pair Formation Free Enthalpies and their Solvent Dependence. *Z. Phys. Chem.* **1982**, *133* (1), 93–98.

(107) Rehm, D.; Weller, A. Kinetics of Fluorescence Quenching by Electron and H-Atom Transfer. *Isr. J. Chem.* **1970**, *8* (2), 259–271.

(108) Vauthey, E. Elucidating the Mechanism of Bimolecular Photoinduced Electron Transfer Reactions. *J. Phys. Chem. B* **2022**, *126* (4), 778–788.

(109) Kuhn, H. J.; Braslavsky, S. E.; Schmidt, R. Chemical actinometry (IUPAC Technical Report). *Pure Appl. Chem.* **2004**, *76* (12), 2105–2146.

(110) Prakash, O.; Lindh, L.; Kaul, N.; Rosemann, N. W.; Losada, I. B.; Johnson, C.; Chábera, P.; Ilic, A.; Schwarz, J.; Gupta, A. K.; Uhlig, J.; Ericsson, T.; Häggström, L.; Huang, P.; Bendix, J.; Strand, D.; Yartsev, A.; Lomoth, R.; Persson, P.; Wärnmark, K. Photophysical Integrity of the Iron(III) Scorpionate Framework in Iron(III)–NHC Complexes with Long-Lived ^{2}LMCT Excited States. *Inorg. Chem.* **2022**, *61* (44), 17515–17526.

(111) Ilic, A.; Schwarz, J.; Johnson, C.; de Groot, L. H. M.; Kaufhold, S.; Lomoth, R.; Wärnmark, K. Photoredox catalysis via consecutive ^{2}LMCT- and ^{3}MLCT-excitation of an Fe(III/II)–N-heterocyclic carbene complex. *Chem. Sci.* **2022**, *13* (32), 9165–9175.

(112) Wellauer, J.; Ziereisen, F.; Sinha, N.; Prescimone, A.; Velić, A.; Meyer, F.; Wenger, O. S. Iron(III) Carbene Complexes with Tunable Excited State Energies for Photoredox and Upconversion. *J. Am. Chem. Soc.* **2024**, *16* (146), 11299–11318.

(113) Kaul, N. Carbenes: The Gathering – Photophysics of Transition Metal Carbene Complexes, Uppsala University, Uppsala, 2023.

(114) Mathur, M. A.; Moore, D. A.; Popham, R. E.; Sisler, H. H.; Dolan, S.; Shore, S. G. Trimethylamine-Tribromoborane. In *Inorg. Synth.*; 1992; Vol. 29, pp 51–54.

(115) Liu, B.; Xia, Q.; Chen, W. Direct Synthesis of Iron, Cobalt, Nickel, and Copper Complexes of N-Heterocyclic Carbenes by Using Commercially Available Metal Powders. *Angew. Chem. Int. Ed.* **2009**, *48* (30), 5513–5516.

(116) Alcarazo, M.; Roseblade, S. J.; Cowley, A. R.; Fernández, R.; Brown, J. M.; Lassaletta, J. M. Imidazo[1,5-a]pyridine: A Versatile Architecture for Stable N-Heterocyclic Carbenes. *J. Am. Chem. Soc.* **2005**, *127* (10), 3290–3291.

(117) Kaufhold, S.; Rosemann, N. W.; Chábera, P.; Lindh, L.; Bolaño Losada, I.; Uhlig, J.; Pascher, T.; Strand, D.; Wärnmark, K.; Yartsev, A.; Persson, P. Microsecond Photoluminescence and Photoreactivity of a Metal-Centered Excited State in a Hexacarbene–Co(III) Complex. *J. Am. Chem. Soc.* **2021**.

(118) Otto, S.; Dorn, M.; Förster, C.; Bauer, M.; Seitz, M.; Heinze, K. Understanding and exploiting long-lived near-infrared emission of a molecular ruby. *Coord. Chem. Rev.* **2018**, *359*, 102–111.

(119) Hollis, T. K.; Webster, C. E. Unsymmetrical salts, CCC-NHC pincer metal complexes, and methods of making the same. WO2018175659, 2018.

(120) Dorn, M.; Kalmbach, J.; Boden, P.; Päpcke, A.; Gómez, S.; Förster, C.; Kuczelinis, F.; Carrella, L. M.; Büldt, L. A.; Bings, N. H.; Rentschler, E.; Lochbrunner, S.; González, L.; Gerhards, M.; Seitz, M.; Heinze, K. A Vanadium(III) Complex with Blue and NIR-II Spin-Flip Luminescence in Solution. *J. Am. Chem. Soc.* **2020**, *142* (17), 7947–7955.

(121) Herr, P.; Kerzig, C.; Larsen, C. B.; Häussinger, D.; Wenger, O. S. Manganese(i) complexes with metal-to-ligand charge transfer luminescence and photoreactivity. *Nat. Chem.* **2021**, *13* (10), 956–962.

(122) *Man on the moon tech*. https://manonthemoontech.com/ (accessed 2024-08-20).

(123) Roselló-Merino, M.; Rama, R. J.; Díez, J.; Conejero, S. Catalytic dehydrocoupling of amine-boranes and amines into diaminoboranes: isolation of a Pt(II), Shimoi-type, η1-BH complex. *Chem. Commun.* **2016**, *52* (54), 8389–8392.

(124) Huber, F. L.; Amthor, S.; Schwarz, B.; Mizaikoff, B.; Streb, C.; Rau, S. Multi-phase real-time monitoring of oxygen evolution enables in operando water oxidation catalysis studies. *Sustain. Energy Fuels* **2018**, *2* (9), 1974–1978.

(125) Ahokas, J.; Pettersson, M. Method and Device for Determining Gas Concentration. WO 2013/079806 A1, 2013.

(126) Ahokas, J. Towards Hydrogen Production by Microalgae Biophotolysis: Gas phase Raman-based Analysis for Process Monitoring and Control, Lappeenranta–Lahti University of Technology LUT, 2023.

(127) Larkin, P. J. *Infrared and Raman Spectroscopy: Principles and Spectral Interpretation*, 2nd ed.; Elsevier, 2017.

(128) Hoskins, L. C. Pure rotational Raman spectroscopy of diatomic molecules. *J. Chem. Educ.* **1975**, *52* (9), 568.

(129) Schrader, B. Raman Spectrometers. In *Encyclopedia of Spectroscopy and Spectrometry*; Elsevier, 2017; pp 900–905.

(130) Tachikawa, T.; Majima, T. Single-Molecule Fluorescence Imaging of TiO_2 Photocatalytic Reactions. *Langmuir* **2009**, *25* (14), 7791–7802.

(131) Tian, B.; Gao, W.; Ning, X.; Wu, Y.; Lu, G. Enhancing water splitting activity by protecting hydrogen evolution activity site from poisoning of oxygen species. *Appl. Catal., B* **2019**, *249*, 138–146.

(132) Pfeffer, M. G.; Müller, C.; Kastl, E. T. E.; Mengele, A. K.; Bagemihl, B.; Fauth, S. S.; Habermehl, J.; Petermann, L.; Wächtler, M.; Schulz, M.; Chartrand, D.; Laverdière, F.; Seeber, P.; Kupfer, S.; Gräfe, S.; Hanan, G. S.; Vos, J. G.; Dietzek-Ivanšić, B.; Rau, S. Active repair of a dinuclear photocatalyst for visible-light-driven hydrogen production. *Nat. Chem.* **2022**, *14* (5), 500–506.

(133) Leung, C.-F.; Ng, S.-M.; Ko, C.-C.; Man, W.-L.; Wu, J.; Chen, L.; Lau, T.-C. A cobalt(ii) quaterpyridine complex as a visible light-driven catalyst for both water oxidation and reduction. *Energy Environ. Sci.* **2012**, *5* (7), 7903.

(134) Guo, X.; Li, X.; Liu, X. C.; Li, P.; Yao, Z.; Li, J.; Zhang, W.; Zhang, J. P.; Xue, D.; Cao, R. Selective visible-light-driven oxygen reduction to hydrogen peroxide using BODIPY photosensitizers. *Chem. Commun.* **2018**, *54* (7), 845–848.

(135) Costentin, C.; Dridi, H.; Savéant, J.-M. Molecular Catalysis of O_2 Reduction by Iron Porphyrins in Water: Heterogeneous versus Homogeneous Pathways. *J. Am. Chem. Soc.* **2015**, *137* (42), 13535–13544.

(136) Yin, P.; Yao, T.; Wu, Y.; Zheng, L.; Lin, Y.; Liu, W.; Ju, H.; Zhu, J.; Hong, X.; Deng, Z.; Zhou, G.; Wei, S.; Li, Y. Single Cobalt Atoms with Precise N-Coordination as Superior Oxygen Reduction Reaction Catalysts. *Angew. Chem. Int. Ed.* **2016**, *55* (36), 10800–10805.

(137) Klingler, S.; Bagemihl, B.; Mengele, A. K.; Kaufhold, S.; Myllyperkiö, P.; Ahokas, J.; Pettersson, M.; Rau, S.; Mizaikoff, B. Rationalizing In Situ Active Repair in Hydrogen Evolution Photocatalysis via Non-Invasive Raman Spectroscopy. *Angew. Chem. Int. Ed.* **2023**, *62* (44), e202306287.

(138) Schiermeier, Q.; Tollefson, J.; Scully, T.; Witze, A.; Morton, O. Energy alternatives: Electricity without carbon. *Nature* **2008**, *454* (7206), 816–823.

(139) Wang, R. R.; Zhao, Y. Q.; Babich, A.; Senk, D.; Fan, X. Y. Hydrogen direct reduction (H-DR) in steel industry—An overview of challenges and opportunities. *J. Clean Prod.* **2021**, *329*, 129797.

(140) Öhman, A.; Karakaya, E.; Urban, F. Enabling the transition to a fossil-free steel sector: The conditions for technology transfer for hydrogen-based steelmaking in Europe. *Energy Res. Soc. Sci.* **2022**, *84*, 102384.

(141) Howarth, R. W.; Jacobson, M. Z. How green is blue hydrogen? *Energy. Sci. Eng.* **2021**, *9* (10), 1676–1687.

(142) de Kleijne, K.; de Coninck, H.; van Zelm, R.; Huijbregts, M. A. J.; Hanssen, S. V. The many greenhouse gas footprints of green hydrogen. *Sustain. Energy Fuels* **2022**, *6* (19), 4383–4387.

(143) IEA. *The Future of Hydrogen*; Paris, 2019. https://www.iea.org/reports/the-future-of-hydrogen (accessed 2024-06-11).

(144) DeLaive, P. J.; Sullivan, B. P.; Meyer, T. J.; Whitten, D. G. Applications of light-induced electron-transfer reactions. Coupling of hydrogen generation with photoreduction of ruthenium(II) complexes by triethylamine. *J. Am. Chem. Soc.* **1979**, *101* (14), 4007–4008.

(145) Kalyanasundaram, K.; Kiwi, J.; Grätzel, M. Hydrogen Evolution from Water by Visible Light, a Homogeneous Three Component Test System for Redox Catalysis. *Helv. Chim. Acta* **1978**, *61* (7), 2720–2730.

(146) Kalyanasundaram, K.; Grätzel, M. Cyclic Cleavage of Water into H_2 and O_2 by Visible Light with Coupled Redox Catalysts. *Angew. Chem. Int. Ed.* **1979**, *18* (9), 701–702.

(147) Kiwi, J.; Grätzel, M. Hydrogen evolution from water induced by visible light mediated by redox catalysis. *Nature* **1979**, *281* (5733), 657–658.

(148) Dau, H.; Fujita, E.; Sun, L. Artificial Photosynthesis: Beyond Mimicking Nature. *ChemSusChem* **2017**, *10* (22), 4228–4235.

(149) Berardi, S.; Drouet, S.; Francàs, L.; Gimbert-Suriñach, C.; Guttentag, M.; Richmond, C.; Stoll, T.; Llobet, A. Molecular artificial photosynthesis. *Chem. Soc. Rev.* **2014**, *43* (22), 7501–7519.

(150) Du, P.; Schneider, J.; Jarosz, P.; Eisenberg, R. Photocatalytic generation of hydrogen from water using a platinum(II) terpyridyl acetylide chromophore. *J. Am. Chem. Soc.* **2006**, *128* (24), 7726–7727.

(151) Du, P.; Knowles, K.; Eisenberg, R. A homogeneous system for the photogeneration of hydrogen from water based on a platinum(II) terpyridyl acetylide chromophore and a molecular cobalt catalyst. *J. Am. Chem. Soc.* **2008**, *130* (38), 12576–12577.

(152) Fihri, A.; Artero, V.; Pereira, A.; Fontecave, M. Efficient H_2-producing photocatalytic systems based on cyclometalated iridium- and tricarbonylrhenium-diimine photosensitizers and cobaloxime catalysts. *Dalton Trans.* **2008**, 41, 5567.

(153) Okura, I.; Kim-Thuan, N. Hydrogen generation by visible light with zinc(II) tetraphenylporphyrin in aqueous micellar solutions. *J. Mol. Catal.* **1979**, *6* (3), 227–230.

(154) Luo, S. P.; Esteban Mejía; Friedrich, A.; Pazidis, A.; Junge, H.; Surkus, A. E.; Jackstell, R.; Denurra, S.; Gladiali, S.; Lochbrunner, S.; Beller, M. Photocatalytic water reduction with copper-based photosensitizers: A noble-metal-free system. *Angew. Chem. Int. Ed.* **2013**, *52* (1), 419–423.

(155) Sun, Y.-Y.; Wang, H.; Chen, N.-Y.; Lennox, A. J. J.; Friedrich, A.; Xia, L.-M.; Lochbrunner, S.; Junge, H.; Beller, M.; Zhou, S.; Luo, S.-P. Efficient Photocatalytic Water Reduction Using In Situ Generated Knölker's Iron Complexes. *ChemCatChem* **2016**, *8* (14), 2340–2344.

(156) Wang, X.; Maeda, K.; Thomas, A.; Takanabe, K.; Xin, G.; Carlsson, J. M.; Domen, K.; Antonietti, M. A metal-free polymeric photocatalyst for hydrogen production from water under visible light. *Nat. Mater.* **2009**, *8* (1), 76–80.

(157) Lazarides, T.; McCormick, T.; Du, P.; Luo, G.; Lindley, B.; Eisenberg, R. Making hydrogen from water using a homogeneous system without noble metals. *J. Am. Chem. Soc.* **2009**, *131* (26), 9192–9194.

(158) Zimmer, P.; Müller, P.; Burkhardt, L.; Schepper, R.; Neuba, A.; Steube, J.; Dietrich, F.; Flörke, U.; Mangold, S.; Gerhards, M.; Bauer, M. N-Heterocyclic Carbene Complexes of Iron as Photosensitizers for Light-Induced Water Reduction. *Eur. J. Inorg. Chem.* **2017**, *2017* (11), 1504–1509.

(159) Huber-Gedert, M.; Nowakowski, M.; Kertmen, A.; Burkhardt, L.; Lindner, N.; Schoch, R.; Herbst-Irmer, R.; Neuba, A.; Schmitz, L.; Choi, T.; Kubicki, J.; Gawelda, W.; Bauer, M. Fundamental Characterization, Photophysics and Photocatalysis of a Base Metal Iron(II)-Cobalt(III) Dyad. *Chem. Eur. J.* **2021**, *27* (38), 9905–9918.

(160) Kanoufi, F.; Zu, Y.; Bard, A. J. Homogeneous Oxidation of Trialkylamines by Metal Complexes and Its Impact on Electrogenerated Chemiluminescence in the Trialkylamine/Ru(bpy)$_3^{2+}$ System. *J. Phys. Chem. B* **2001**, *1* (105), 210–216.

(161) Hu, X.; Cossairt, B. M.; Brunschwig, B. S.; Lewis, N. S.; Peters, J. C. Electrocatalytic hydrogen evolution by cobalt difluoroboryl-diglyoximate complexes. *Chem. Commun.* **2005**, *1* (37), 4723.

(162) Du, P.; Schneider, J.; Luo, G.; Brennessel, W. W.; Eisenberg, R. Visible Light-Driven Hydrogen Production from Aqueous Protons Catalyzed by Molecular Cobaloxime Catalysts. *Inorg. Chem.* **2009**, *48* (11), 4952–4962.

(163) Bakac, A.; Espenson, J. H. Unimolecular and bimolecular homolytic reactions of organochromium and organocobalt complexes. Kinetics and equilibria. *J. Am. Chem. Soc.* **1984**, *106* (18), 5197–5202.

(164) Fihri, A.; Artero, V.; Razavet, M.; Baffert, C.; Leibl, W.; Fontecave, M. Cobaloxime-based photocatalytic devices for hydrogen production. *Angew. Chem. Int. Ed.* **2008**, *47* (3), 564–567.

(165) Schrauzer, G. N.; Parshall, G. W.; Wonchoba, E. R. Bis(Dimethylglyoximato)Cobalt Complexes: ("Cobaloximes"). In *Inorg. Synth.*; Jolly, W. L., Ed.; 1968; Vol. 11, pp 61–70.

(166) Wayner, D. D. M.; McPhee, D. J.; Griller, D. Oxidation and Reduction Potentials of Transient Free Radicals. *J. Am. Chem. Soc.* **1988**, *110* (1), 132–137.

(167) Bhattacharyya, K.; Das, P. K. Nanosecond transient processes in the triethylamine quenching of benzophenone triplets in aqueous alkaline media. Substituent effect, ketyl radical deprotonation, and secondary photoreduction kinetics. *J. Phys. Chem.* **1986**, *90* (17), 3987–3993.

(168) Protti, S.; Albini, A.; Serpone, N. Photocatalytic generation of solar fuels from the reduction of H_2O and CO_2: a look at the patent literature. *Phys. Chem. Chem. Phys.* **2014**, *16* (37), 19790.

(169) IEA. *Net Zero by 2050*; Paris, 2021. https://www.iea.org/reports/net-zero-by-2050 (accessed 2024-09-16).

(170) Fujita, E. Photochemical carbon dioxide reduction with metal complexes. *Coord. Chem. Rev.* **1999**, *185–186*, 373–384.

(171) Lehn, J.-M.; Ziessel, R. Photochemical generation of carbon monoxide and hydrogen by reduction of carbon dioxide and water under visible light irradiation. *Proc. Natl. Acad. Sci. U.S.A.* **1982**, *79* (2), 701–704.

(172) Matsuoka, S.; Yamamoto, K.; Ogata, T.; Kusaba, M.; Nakashima, N.; Fujita, E.; Yanagida, S. Efficient and selective electron mediation of cobalt complexes with cyclam and related macrocycles in the p-terphenyl-catalyzed photoreduction of carbon dioxide. *J. Am. Chem. Soc.* **1993**, *115* (2), 601–609.

(173) Hawecker, J.; Lehn, J.-M.; Ziessel, R. Efficient photochemical reduction of CO_2 to CO by visible light irradiation of systems containing $Re(bipy)(CO)_3X$ or $Ru(bipy)_3^{2+}$–Co^{2+} combinations as homogeneous catalysts. *J. Chem. Soc., Chem. Commun.* **1983**, 9, 536–538.

(174) Yamazaki, Y.; Takeda, H.; Ishitani, O. Photocatalytic reduction of CO2 using metal complexes. *J. Photochem. Photobiol., C* **2015**, *25* (4), 106–137.

(175) Won, D. Il; Lee, J. S.; Ba, Q.; Cho, Y. J.; Cheong, H. Y.; Choi, S.; Kim, C. H.; Son, H. J.; Pac, C.; Kang, S. O. Development of a Lower Energy Photosensitizer for Photocatalytic CO2 Reduction: Modification of Porphyrin Dye in Hybrid Catalyst System. *ACS Catal.* **2018**, *8* (2), 1018–1030.

(176) Muñoz-Molina, J. M.; Belderrain, T. R.; Pérez, P. J. Atom Transfer Radical Reactions as a Tool for Olefin Functionalization – On the Way to Practical Applications. *Eur. J. Inorg. Chem.* **2011**, *2011* (21), 3155–3164.

(177) Kharasch, M. S.; Jensen, E. V.; Urry, W. H. Addition of Carbon Tetrachloride and Chloroform to Olefins. *Science* **1945**, *102* (2640), 128–128.

(178) Kharasch, M. S.; Skell, P. S.; Fisher, P. Reactions of Atoms and Free Radicals in Solution. XII. The Addition of Bromo Esters to Olefins. *J. Am. Chem. Soc.* **1948**, *70* (3), 1055–1059.

(179) Curran, D. P.; Bosch, E.; Kaplan, J.; Newcomb, M. Rate constants for halogen atom transfer from representative α-halo carbonyl compounds to primary alkyl radicals. *J. Org. Chem.* **1989**, *54* (8), 1826–1831.

(180) Curran, D. P.; Chen, M. H.; Spletzer, E.; Seong, C. M.; Chang, C. T. Atom-transfer addition and annulation reactions of iodomalonates. *J. Am. Chem. Soc.* **1989**, *111* (24), 8872–8878.

(181) Nguyen, J. D.; Tucker, J. W.; Konieczynska, M. D.; Stephenson, C. R. J. J. Intermolecular Atom Transfer Radical Addition to Olefins Mediated by Oxidative Quenching of Photoredox Catalysts. *J. Am. Chem. Soc.* **2011**, *133* (12), 4160–4163.

(182) Courant, T.; Masson, G. Recent Progress in Visible-Light Photoredox-Catalyzed Intermolecular 1,2-Difunctionalization of Double Bonds via an ATRA-Type Mechanism. *J. Org. Chem.* **2016**, *81* (16), 6945–6952.

(183) Brandl, F.; Bergwinkl, S.; Allacher, C.; Dick, B. Consecutive Photoinduced Electron Transfer (conPET): The Mechanism of the Photocatalyst Rhodamine 6G. *Chem. Eur. J.* **2020**, *26* (35), 7946–7954.

(184) Graml, A.; Neveselý, T.; Jan Kutta, R.; Cibulka, R.; König, B. Deazaflavin reductive photocatalysis involves excited semiquinone radicals. *Nat. Commun.* **2020**, *11* (1), 3174.

(185) Haimerl, J.; Ghosh, I.; König, B.; Vogelsang, J.; Lupton, J. M. Single-molecule photoredox catalysis. *Chem. Sci.* **2019**, *10* (3), 681–687.

(186) Ghosh, I.; Ghosh, T.; Bardagi, J. I.; König, B. Reduction of aryl halides by consecutive visible light-induced electron transfer processes. *Science* **2014**, *346* (6210), 725–728.

(187) Purser, S.; Moore, P. R.; Swallow, S.; Gouverneur, V. Fluorine in medicinal chemistry. *Chem. Soc. Rev.* **2008**, *37* (2), 320–330.

(188) Miller, M. A.; Sletten, E. M. Perfluorocarbons in Chemical Biology. *ChemBioChem* **2020**, *21* (24), 3451–3462.

(189) Buzzetti, L.; Crisenza, G. E. M.; Melchiorre, P. Mechanistic Studies in Photocatalysis. *Angew. Chem. Int. Ed.* **2019**, *58* (12), 3730–3747.

(190) Rosemann, N. W.; Lindh, L.; Bolaño Losada, I.; Kaufhold, S.; Prakash, O.; Ilic, A.; Schwarz, J.; Wärnmark, K.; Chábera, P.; Yartsev, A.; Persson, P. Competing dynamics of intramolecular deactivation and bimolecular charge transfer processes in luminescent Fe(III) N-heterocyclic carbene complexes. *Chem. Sci.* **2023**, *14* (13), 3569–3579.

(191) Prakash, O.; Chábera, P.; Kaul, N.; Hlynsson, V. F.; Rosemann, N. W.; Losada, I. B.; Hoang Hai, Y. T.; Huang, P.; Bendix, J.; Ericsson, T.; Häggström, L.; Gupta, A. K.; Strand, D.; Yartsev, A.; Lomoth, R.; Persson, P.; Wärnmark, K. How Rigidity and Conjugation of Bidentate Ligands Affect the Geometry and Photophysics of Iron *N*-Heterocyclic Complexes: A Comparative Study. *Inorg. Chem.* **2024**, *63* (10), 4461–4473.

(192) Paulus, B. C.; Adelman, S. L.; Jamula, L. L.; McCusker, J. K. Leveraging excited-state coherence for synthetic control of ultrafast dynamics. *Nature* **2020**, *582* (7811), 214–218.

(193) Darari, M.; Francés-Monerris, A.; Marekha, B.; Doudouh, A.; Wenger, E.; Monari, A.; Haacke, S.; Gros, P. C. Towards Iron(II) Complexes with Octahedral Geometry: Synthesis, Structure and Photophysical Properties. *Molecules* **2020**, *25* (24), 5991.

(194) May, A. M.; Dempsey, J. L. A new era of LMCT: leveraging ligand-to-metal charge transfer excited states for photochemical reactions. *Chem. Sci.* **2024**, *15* (18), 6661–6678.

Printed by Media-Tryck, Lund 2024 NORDIC SWAN ECOLABEL 3041 0903

ISBN 978-91-8096-068-7

Centre for Analysis and Synthesis
Department of Chemistry
Faculty of Science
Lund University

LUND UNIVERSITY